Hahn-Meitner-Institut Berlin
in der Helmholtz-Gemeinschaft

Annual Report 2006
Selected Results

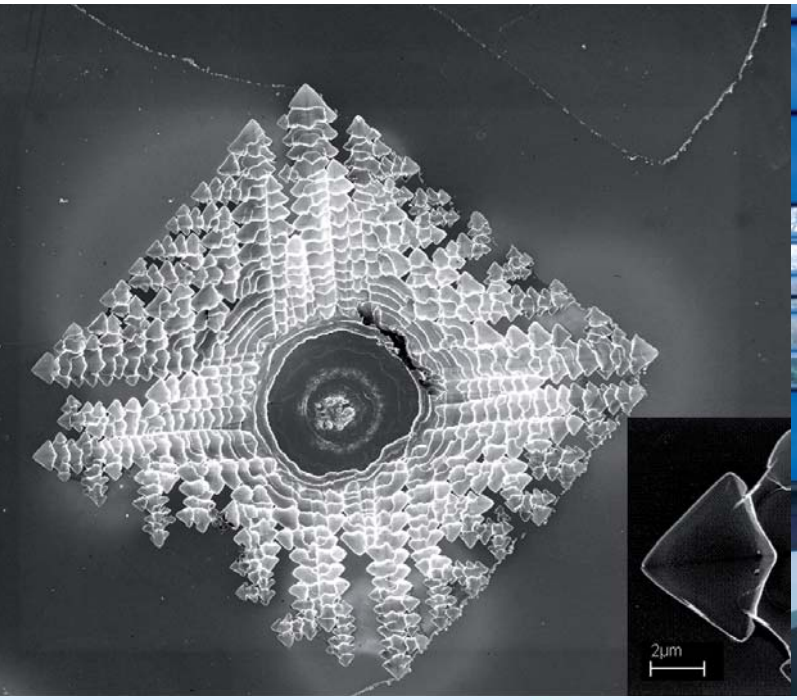

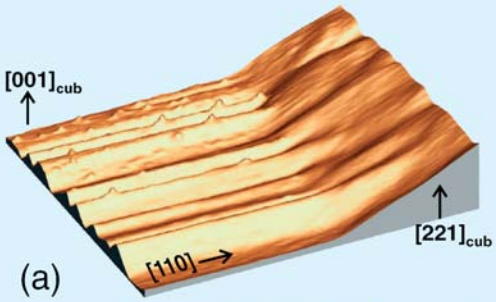

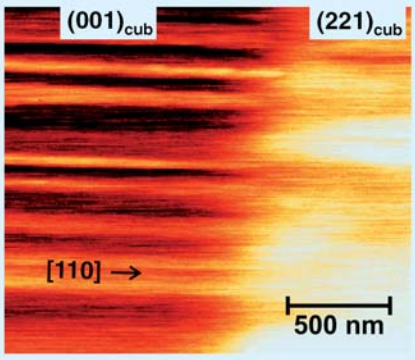

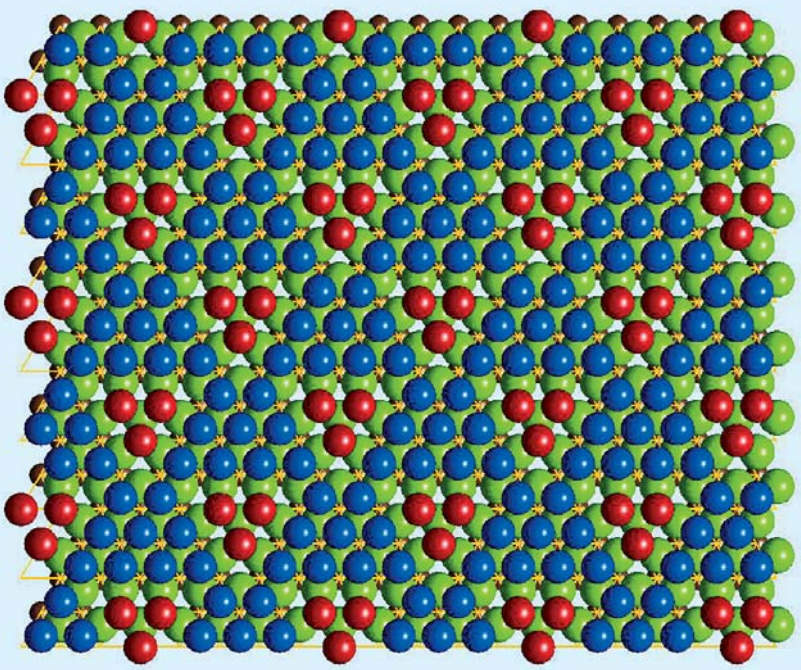

HMI-B 614

Legend to Cover Figures:

top left: HR-SEM image of a Si(100) surface after 10 min in 40% NH_4F at 6V
top right: Model of HMI's new high field magnet
bottom left: 3D representation of the topography close to the epitaxially grown $\sum 3$ grain boundary of a $CuGaSe_2$ bicrystal as measured by KPFM
bottom right: Arrangement of Sodium atoms (red and blue) in Na_xCoO_2 with a 80% filled sodium layer

Annual Report 2006
Selected Results

Hahn-Meitner-Institut
Berlin, 2007

Table of contents

Foreword

This Annual Report presents the most important events and selected scientific Highlights of the Hahn-Meitner-Institut from the year 2006.

2006 was the last year of research with ions at HMI. Closing of the institute's Ion Beam Laboratory ISL completes 40 years of successful research using ion accelerators.

The proton induced eye tumour therapy at HMI will survive this turning point: The Charité University Hospital Berlin is ready to continue the therapy in Wannsee with HMI delivering the proper proton beam on the basis of full cost refunding outside our research programme.

Part of the ISL experimental stations designed for heavy ion induced materials modification and analysis will be transferred to GSI, the Gesellschaft für Schwerionenforschung in Darmstadt, to allow the user community to continue the corresponding part of their scientific programme.

We will take all efforts to justify the closure of ISL by integrating the personnel and the resources for the visible benefit of the research with neutrons and synchrotron light.

This will concern two major tasks in particular:
The most spectacular project for the research with neutrons is certainly the new High Field Magnet. With its realisation, scheduled for 2010, we will further sharpen our profile and remain at the forefront in providing extreme sample environments. We are grateful that the Helmholtz Association has approved the funding of the project.

The installation of the instruments in the new Neutron Guide Hall II is in progress. This includes the new time-of-flight diffractometer EXED at the new multispectral neutron guide, specifically designed for experiments utilising the new High Field Magnet.

The other major task will be the upgrade of the "old" instruments over the next years. An external review panel convened in October 2006 to discuss a priority list.

The Solar Energy Research Division very successfully passed the mid-term evaluation of its first programme-period under the programme-oriented funding (POF). In this context, an extensive discussion on the future strategy for this program took place. An important result is the foundation of a Competence Center for Photovoltaic Thin-Film Technology. The task of this centre, co-ordinating the activities of HMI, the Technische Universität (TU) Berlin and industry, will be to combine the more fundamental research at HMI with the technology and device oriented activities at the TU and the actual production by industrial companies.

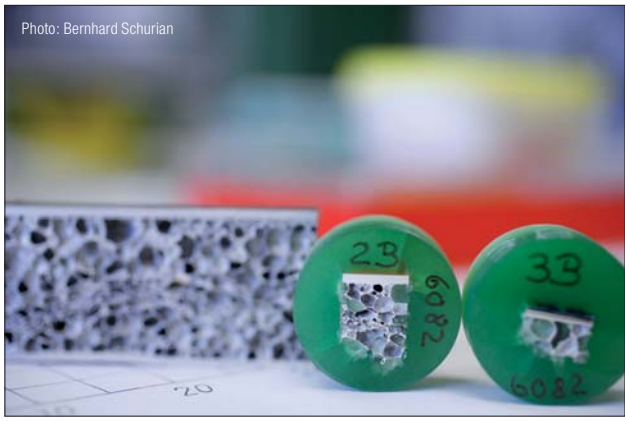

One of the key figures in this project is the new head of the department Silicon Photovoltaics (SE1), Bernd Rech, whom we gladly welcomed joining HMI in June 06.

Other new faculty appointments were on halt because of the pending formulation of the Structure and Development Plan for the next one to two decades. As the S&E plan is now formulated, we hope to advance with the search for the new department heads SF1, SF4 and SE4 without further delay.

All these developments, together with the continuing devoted engagement of our staff as well as of our associates makes us grateful and looking forward very trustfully.

Scientific Director (CEO) Prof. Dr. Michael Steiner, Administrative Director Dr. Ulrich Breuer

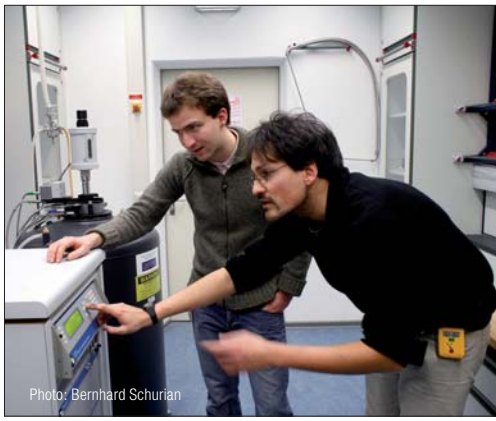

Photo: Bernhard Schurian

HMI in brief

The **Hahn-Meitner-Institut** (HMI) in Berlin is one of Germany's leading centres for research on solar energy conversion, condensed matter and materials science. It has approximately 750 employees, including almost 300 scientists – most of them physicists and chemists. Most of the institute's annual budget of roughly 70 Million € is provided by the German Federal Government and the City of Berlin in a ratio of 9 to 1.

The Hahn-Meitner-Institut is member of the Helmholtz Association of National Research Centres, an organisation representing fifteen of Germany's largest scientific institutions. The common mission of the Helmholtz centres is to develop, set-up and operate large-scale facilities, to solve complex – often multidisciplinary – scientific and technological problems in long-term proactive research programmes and to develop high technologies for the future. The Helmholtz Association concentrates its work in six research fields: *Energy, Earth and Environment, Health, Structure of Matter, Transport and Space* and *Key Technologies*. For each of these fields, scientists develop several research programmes for 5-year periods. These programmes are then evaluated by a group of international experts. This evaluation forms the basis for the programme-oriented funding, which distributes the financial resources to the scientific programmes of the Helmholtz research fields rather than to the institutes.

Scientific work at the Hahn-Meitner-Institut is organised in two divisions reflecting the two main fields of activity: *Solar Energy Research* and *Structure and Dynamics in Condensed Matter*. The Solar Energy Research is part of the Helmholtz-programme *Renewable Energies* within the research field *Energy*. Most of the activities of the Division *Structure and Dynamics in Condensed Matter* are part of the programme *Large-Scale Facilities for Research with Photons, Neutrons and Ions* in the research field *Structure of Matter*. The research on trace elements is conducted in the Helmholtz programme *Environmental Health* within the research field *Health*.

Solar energy research at the Hahn-Meitner-Institut is the largest effort in the field of sustainable energy within the Helmholtz Association and comprises approximately 25 % of HMI's research and development efforts. As an interdisciplinary activity between solid state physics, material chemistry, optics and interfacial chemistry, it aims at creating scientific and technological preconditions for significantly increasing the contribution of sustainable energy to our energy supply over the next decades. This activity is taking advantage of an already well balanced research infrastructure and increasingly uses the unique measurement opportunities provided by the large scale facilities of the Hahn-Meitner-Institut.

Photo: Bernhard Schurian

Materials and concepts for thin-film solar cells are at the centre of the solar energy research at HMI. These activities cover the entire spectrum from basic research to the design of actual devices. The focus is on the currently most promising technologies, namely thin-film poly-crystalline silicon and compound semiconductors of the I-III-VI_2 and III-V type. Research projects aim at the development of efficient photo-voltaic solar cells which allow substantial reductions in the costs of solar power generation. The strategy is to develop existing thin-film technologies to a state of maturity and, in parallel, to explore new materials and concepts for solar cells of the future, e.g. nanocomposite crystalline materials.

After closing the ion beam lab by end of 2006, research on Structure and Dynamics in Condensed Matter at the Hahn-Meitner-Institut is focused on experimental investigations of structures and materials using neutrons and synchrotron x-rays as probes. These two probes are provided by two large-scale facilities: The 10 MW research reactor BER II operated by HMI on its grounds in Berlin-Wannsee with the Berlin Neutron Scattering Center BENSC and the 3rd generation electron storage ring BESSY, an independent research institution in Berlin-Adlershof.

All facilities are primarily operated for a national and international user community. About 70 % of the beam time at the instruments is used by scientists from other research institutes, universities and industry from Germany and from abroad. It is HMI's policy to provide these users with full scale technical and scientific support, this way enabling them to make best possible use of the facilities. An outstanding highlight among the HMI activities are neutron scattering studies of samples in extreme sample environments such as very high magnetic fields and extremely low temperatures made possible by the institute's unique expertise on sample environment equipment. Fields in the focus of in-house structural research are magnetic phenomena, properties and design of engineering components and materials, soft matter and biological systems as well as theoretical physics.

Furthermore, HMI's accelerator facility provides the beam for the eye tumour therapy with protons operated by the University Hospital Charité.

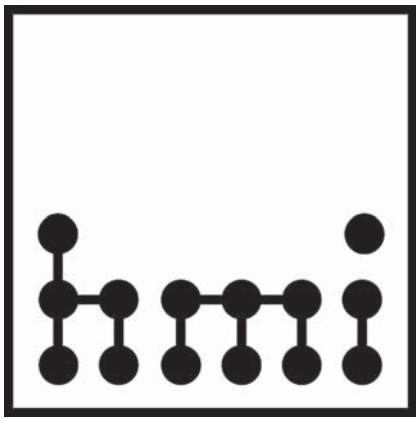


Photo: Sebastian Frenkel


Photo: Bernhard Schurian

A model of the planned new high field magnet of the Hahn-Meitner-Institut. It will be the world's strongest magnet for neutrons scattering experiments.

News and Events 2006

(Photo: Bernhard Schurian)

Prof. Dr. Bernd Rech

Since 1 July the department SE1 Silicon Photovoltaics has been headed by Prof. Dr. Bernd Rech, who was also appointed Professor at the Technische Universität Berlin (TUB) on the 1 January 2007. Professor Rech was formerly employed at the Forschungszentrum Jülich (FZJ), where he was head of a working group for solar cell technology.

Bernd Rech, new head of the department Crystalline Silicon Photovoltaics

Prof. Dr. H.-W. Schock

Prof. Schock (SE3 Technology) took the post as head of the division in October 2006 from Prof. Tributsch (SE5 Solar Energetics), who went for a sabbatical to Australia.

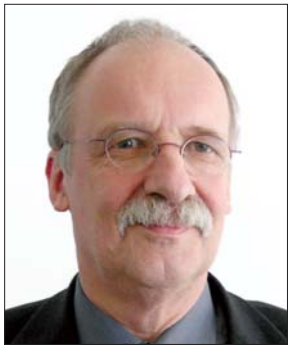

Hans Werner Schock, Head of Division Solar Energy

Prof. Dr. Judith Peters

Prof. Dr. Judith Peters, instrument scientist at the department SF1 responsible for the set up of the high resolution diffractometer EXED, has been appointed professor of Biophysics at the Université Joseph Fourier in Grenoble France. She assumed office on 1 September 2006. In addition to her position at the university, she is responsible for the neutron scattering instrument IN13 at the ILL research reactor.

Judith Peters – formerly scientist at HMI, now professor of biophysics in Grenoble. (Photo: David Ausserhofer)

Dr. Eveline Rudigier

Dr. Eveline Rudigier has won the Shell She-Study-Award 2006. In her thesis the 32-year old showed how the production of pollution free solar cells can be improved. By correlating the material properties of the active layer made from copper indium sulfide (CIS) with the efficiency of the solar cells, she made an important contribution for the process optimization of CIS thin-film solar cells. A patent application affirms the practical relevance of her work.

Eveline Rudigier was awarded the Shell She-Study-Award for her work on pollution free solar cells

Tumour Therapy at HMI continues

The eye tumour therapy at the Hahn-Meitner-Institut will be continued – this is the main result of the new contract between the HMI and the Charité, Berlin's university hospital. The original plan was to close down the therapy with the decision to close HMI's ion beam laboratory ISL. This would have meant the shut down of Germany's only facility, where eye tumours can be treated with protons. German patients would have been forced to travel abroad to be treated.

The decision to continue the operations at this unique facility was announced at a press conference on 16 February 2007 attended by Thomas Rachel, the Parliamentary State Secretary to the Federal Minister of Education and Research, and Prof. Dr. Jürgen Zöllner, Senator of Education, Science and Research of the City State of Berlin.

The new contract allows the continuation of the therapy with HMI operating the accelerators and providing the necessary proton beam and Charité taking care of all medical aspects. Thus the medical physicists responsible for the planning of the treatment, e.g. adjusting the range and shape of the beam to the needs of every single patient and the medical research, changed from HMI to Charité.

Michael Foerster, Head of the Ophthalmologic clinic of the Charité University hospital (left) and Thomas Dünow, the first person to be treated with protons at HMI in the therapy room.

Compared to other forms of cancer therapy, proton therapy has the advantage that one can confine the impact of the proton beam to the tumour, thus sparing the surrounding healthy tissue. This is particularly important in the case of tumours located in the vicinity of sensitive organs such as – in the case of the eye – the macula or the optic disc.

At the press conference announcing the continuation of the proton therapy at HMI:
From left to right: Detlev Ganten, head of the Charité university hospital, Jürgen Zöllner, Senator of Education, Science and Research of the City State of Berlin, Thomas Rachel, Parliamentary State Secretary to the Federal Minister of Education and Research, Michael Steiner, Scientific director of the Hahn-Meitner-Institut.

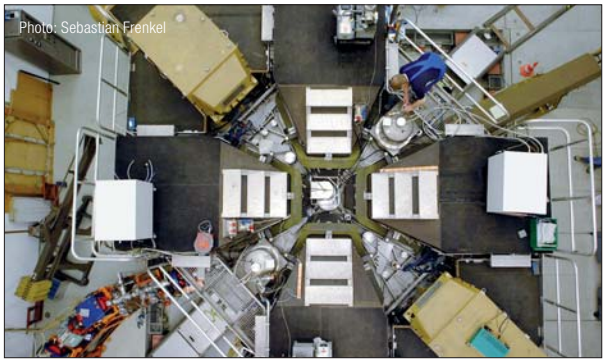

HMI's cyclotron accelerates protons to the velocity necessary for proton therapy.

Until the shut down of ISL the accelerators producing the proton beam were providing mainly ion beams for experiments in ion-solid interaction and material analysis. As the proton energy available at the HMI corresponds to a range of about 4 centimetres in living tissue, in 1993 the then Klinikum Steglitz (now Charité – Campus Benjamin Franklin) and HMI signed a co-operation contract to install a facility for the treatment of eye tumours. The proton therapy at HMI started in 1998. Since then the treatment more than 800 patients have been treated. Most of them suffered from choroidal melanomas, malignant tumours, located at the posterior pole of the eye.

Competence center for thin-film- and nanotechnologies for photovoltaics to be built in Berlin

The Hahn-Meitner-Institut (HMI), the Technische Universität Berlin (TUB) and eight leading industrial companies signed a memorandum of understanding (MoU) in April. Together with the WISTA Management GmbH and the TSB Technologiestiftung Innovationsagentur Berlin GmbH, the HMI and the TUB are planning to working hand-in-hand with the industry to develop innovative products for photovoltaics and thus bridge the gap between fundamental research and industrial production.

One of the first tasks at hand for the competence centre is to address central questions emerging from the coating of thin-film solar modules. In doing so, prototypes are to be designed in close cooperation with the industry. In addition, innovative solar cell concepts and manufacturing procedures will be developed.

Integrated EU-Project ATHLET aims for advancement of photovoltaic thin film technology

Cost reduction is the central mission of photovoltaics today, and thin-film-technology one major approach to meet this challenge. To promote the transition from thin-film solar cell research to into the market, Europe's largest thin-film-technology research-project started in January 2006. On 19 February the kick-off meeting and press-conference took place in Berlin. 24 partners from 11 countries are working together on the development, assessment and consolidation of photovoltaic thin film technology. The Integrated Project with partners from industry, universities and research facilities is being coordinated by the HMI.

The Participants of the ATHLET project at their first meeting, 19 February 2006 in Berlin

Late night science

Reactor of the Hahn-Meitner-Institut opens to the public was the title of a newspaper article announcing the HMI's offer for the Lange Nacht der Wissenschaften 2006 – the open "day" of all the scientific institutes in Berlin and Potsdam on 13 May. And it probably was the prospect of accessing areas that are usually completely inaccessible to the public – the experimental halls around the research reactor and the accelerators of the Ion Beam Laboratory – that drew about 1600 visitors to HMI's campus at Berlin-Wannsee.

But HMI offered its visitors much more than guided tours to its large scale facilities. One could watch metals turn into foam, experience the force exerted by a very strong magnet on metal tools or learn how neutrons help art historians find out the story of painting.

A special focus of the Lange Nacht 2006 at HMI was the programme for children. The school lab opened its doors and gave older children the opportunity to operate a magnetic accelerator or to learn how to put the largest possible number of footballs into a huge box; special lab tours for children allowed them to experience various labs at their own pace. The highlight of the programme for smaller children was Klaus Kiefer's presentation "A day in the life of a physicist". Kiefer, a scientist in the sample environment group, not only showed what a scientist is doing all day, but also made the children experience what it feels to be an atom in a melting crystal.

But HMI is not only Wannsee. The parts of the institute located in Adlershof, also participated in the Lange Nacht. The scientists at the department Silicon photovoltaics answered countless questions about solar energy and let their visitors find out on an energy bike how much it takes to produce the energy necessary to operate a television set.

The marketplace of science

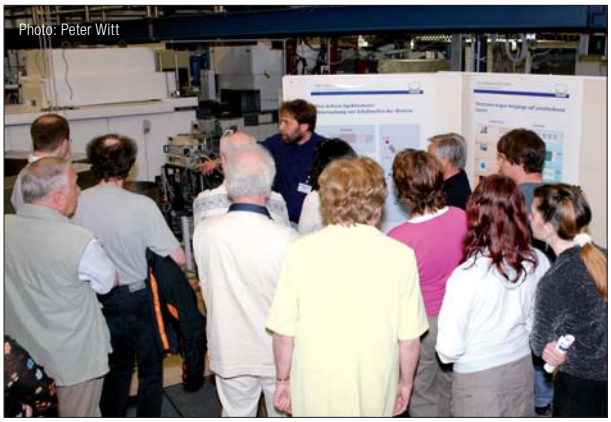

Explaining neutron scattering to visitors at the Lange Nacht der Wissenschaften

Experiencing a really strong magnet

Solar Energy evaluated

(Not only) members of the review panel took interest in the poster session during the SE-evaluation

The division Solar Energy presented itself in the mid term evaluation of its first programme-period under the program-oriented funding (POF). This was the first evaluation for HMI since the start of the program-oriented funding in 2004. On 3 April, the intensive preparations proved to be worth their while: a full programme with presentations, poster sessions on tours through the laboratories offered the review a thorough picture of the research activities. The results of the evaluation were highly successful; the review panel gave a very optimistic and positive assessment of the R&D activities regarding solar energy.

HMI's Solar Energy presents itself

On the weekend 26 – 27 August, the German government invited to the *Tage der offenen Tür der Bundesregierung* (open days of the government). The HMI presented its solar energy research at the Federal Environment Ministry together with the Forschungsverbund Sonnenenergie (FVS). Visitors could learn all about the advantages and challenges of thin-film-technology. The HMI-Stand was visited by the secretary of state Astrid Klug who showed explicit interest in the research done at the HMI.

Europe's most important photovoltaics conference has always been a mandatory destination for the researchers of the division solar energy. But in September 2006, the HMI participated for the first time with a stand at the fair, together with the HMI spin-off Sulfurcell. The HMI booth, located in a crowded and hot tent, was visited by many experts as well as the interested public. After four days, the stand personnel was hardly able to talk any more, but all participants agreed to continue the participation at the next PVSEC as well as to carry on with the combined presentation of the HMI together with Sulfurcell.

The HMI is a steady participant at one of Berlin's largest fair for renewable energies. Besides information to various aspects of photovoltaics, visitors could learn about the everyday energy-consumption with the "Energy-Bike".

Visitors at the HMI-stand at the PVSEC fair in Dresden

HMI-stand at the exhibit with a Sulfurcell prototype (PVSEC Dresden)

Perspective for a growing business – innovations in photovoltaics

The “Day for the industry” (Industrietag) of the division Solar Energy reflected the current success in the photovoltaics business: around 120 guests were expected to come on 27 November to Berlin-Wannsee, more than 160 showed up to learn more about this successful technology. Speakers from industry and science gave an overview as well as important inputs for future developments. Besides these presentations, the participants could visit different laboratories and speak with the involved scientist. The day concluded with an informal reception in the evening, where guests and HMI employees could talk in a relaxed atmosphere.

Full house: the main auditorium of the HMI was at its carrying capacity, many visitors felt taken back to university as they had to scramble for a seat

The end of a success story

In 2004, HMI’s board of directors had decided to shut down Ion Beam Lab ISL at the end of 2006 and to concentrate the institute’s efforts in structural research on work with neutrons. The final colloquium on 19th December 2006, attended by colleagues from HMI and scientists from other institutes, marked the end of 12 years of successful scientific work on ion-solid interactions and ion analytics at HMI. The four invited speakers gave a taste of the variety of topics addressed in ISL’s activities: The physicists Sytze Brandenburg (KFI Groningen) and Arjen Vredenberg (University of Utrecht) talked about accelerator technology and ions as a shaping tool for the nanoworld, respectively. Michael Foerster, head of the Ophthalmologic clinic of the Charité University Hospital (Campus Benjamin Franklin) presented the story of the proton therapy at HMI and Dietrich Wildung, head of the Egyptian Museum in Berlin discussed the new paradigm for the research at European archaeological museums – instead of bringing more and more artefacts from abroad one concentrates on detailed investigations of the objects already in the museum. This requires modern scientific techniques such as the analytical tools that were available at ISL.

Finally, it was Arjen Vredenberg’s task to show that not only ISL had many talents, but also its users. In addition to his talk, he played two solo pieces on his cello.

ISL final colloquium: Arjen Vredenberg, ISL user provided the music for the colloquium.

High Field Magnet - HMI to get world's strongest magnet for neutron scattering

For many years, the prospect of performing neutron scattering experiments on matter exposed to extremely high magnetic fields has been attracting users from all over the world to come to HMI. Now, the Helmholtz Association has decided to support the set up of a new high field magnet that will secure HMI's leading role in this field in the years to come. The magnet will create fields above 30 Tesla in its final stage – fields exceeding by far anything available at any neutron centre worldwide. The overall investments of the project will amount to 17.8 million euros with 90% being covered by the Federal Government and 10% by Berlin.

Scientists expect that neutron scattering experiments in the new magnet will contribute to important insights in many fields of condensed matter research, such as quantum magnetism, new materials or high temperature superconductivity. In the latter case researchers hope that experiments at magnetic fields around 25 Tesla will lead to a breakthrough in understanding the mechanism that causes some materials to lose their electrical resistance at temperatures below around minus 200 degrees Celsius.

The new magnet will not only allow for novel experiments, it will be at the forefront of development in magnet design itself. The design of the magnet will follow the Series Connected Hybrid System Technology developed at the National High Magnetic Field Laboratory (NHMFL) in Tallahassee, Florida. The magnetic field will be produced by two coaxial horizontal coils connected in series: The external coil will be made of a low temperature superconductor, while the inner coil will be produced of a copper alloy. The advantage of this construction lies in the fact that the use of superconducting coils helps to reduce the energy costs compared to an all-copper magnet, while the copper part allows reaching fields that cannot be cre-

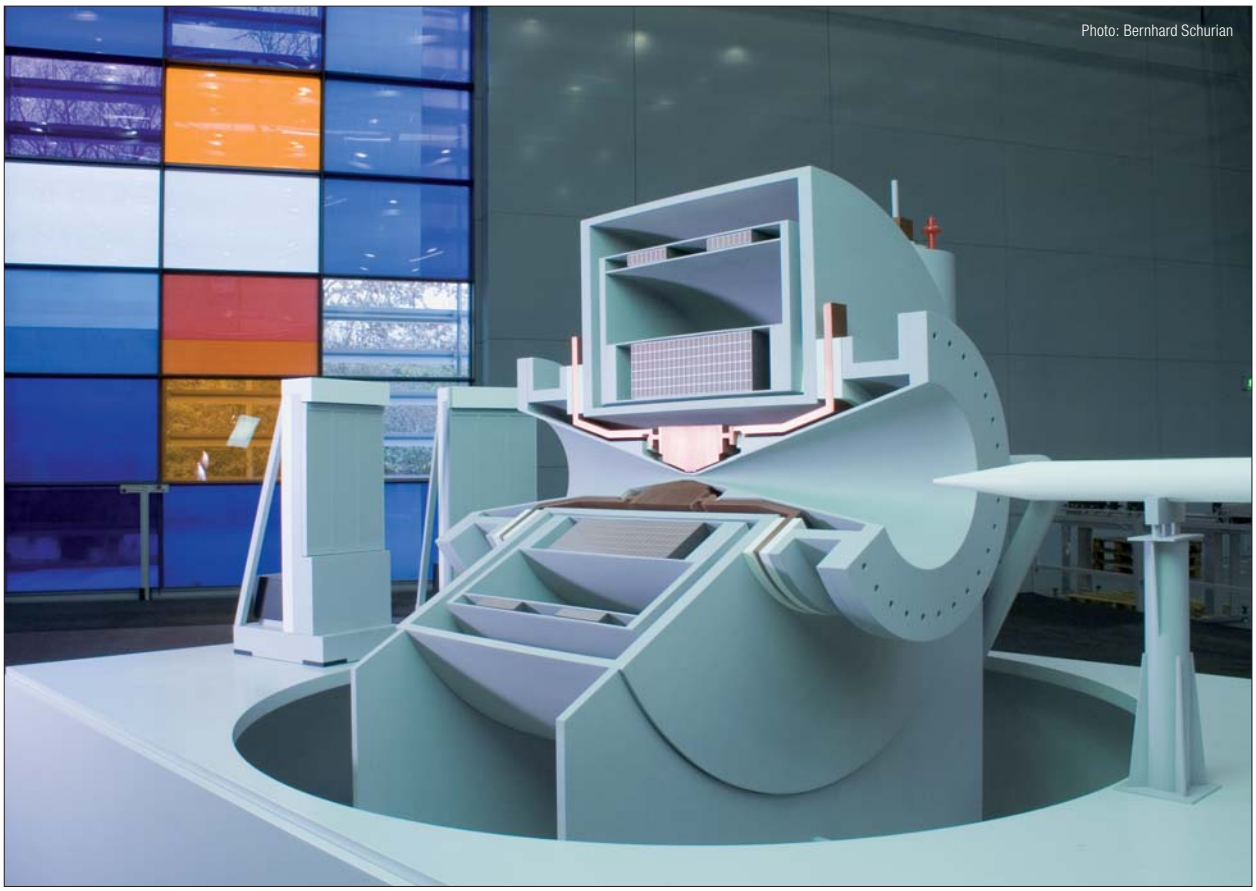

Model of HMI's new high field magnet. The model is cut open showing the inner design of the magnet.

Neutron Guide Hall II in December 2006. The magnet will be placed in front of the big window at the end of the hall. The blue tubes on the right hand side are the neutron guides of the instrument EXED that will be operated with the magnet.

High-field magnet: Signing of the contract between HMI and the National High Magnetic Field Laboratory (NHMFL), Tallahasse, Florida.
At the table (from left to right) Michael Steiner, Scientific Director of HMI, Kirby Kemper, Vice President for Research at Florida State University, Ulrich Breuer, Administrative Director of HMI. Standing: Jürgen Mlynek, President of the Helmholtz-Association, and Thomas Rachel, Parliamentary State Secretary to the Federal Minister of Education and Research.

ated by superconducting coils only because of the critical field of the available superconducting materials.
The magnet will be located at the end of HMI's Neutron Guide Hall II just in front of the stained glass window. Seen from outside, it will have the shape of a horizontal cylinder with conical openings on both sides. These openings will allow the neutrons from the reactor to access the sample located at the centre of the magnet and to continue towards the detectors after scattering. The magnet will be incorporated in the extreme environment diffractometer EXED – a neutron scattering instrument specially developed for that purpose.

It will take another four to five years until the magnet will begin its operations in Berlin. In that time, HMI will build the necessary infrastructure that will supply the magnet with electricity, cooling water and liquid helium and take into operation the diffractometer EXED. The magnet will be designed and constructed by NHMFL in Florida and later shipped to Berlin and assembled at the Hahn-Meitner-Institut. By that time, many condensed matter scientists will have developed ideas for experiments at the new magnet and will be looking forward to new insights into the fascinating worlds of magnetism or superconductivity.

Berlin at the centre of the polarized neutron world

Scattering of polarized neutrons, neutrons with all their spins oriented in one direction, opens for great opportunities in investigating the magnetic properties of materials or – via the spin echo technique – the dynamics in soft matter and other complex systems. In various forms, polarized neutrons are used in experiments at the Hahn-Meitner-Institut and the institute is an important centre for the development of novel techniques in this field.

For a few weeks in September 2006, Berlin and HMI became the centre of the polarized neutron world – the Polarized Neutron School and the PNCMI conference (Polarized Neutrons in Condensed Matter Investigations) were organized by HMI in the German capital. The school, taking place from 19 to 22 September at HMI gave 30 diploma and Ph.D. students the opportunity to get acquainted with polarized neutron research – its experimental and theoretical aspects. The following week, almost 150 experienced researchers convened at the Berlin-Brandenburgische Akademie der Wissenschaften for the PNCMI conference to discuss the latest scientific trends

Speakers and students at the Polarized Neutron School held in Berlin in September 2006

and instrumental developments in this field. A field, which – as Ferenc Mezei remarked in his talk to the school participants – has an old connection with the Hahn-Meitner-Institut: Otto Frisch, the first to create a beam of polarized neutrons, was a nephew of Lise Meitner.

27th Tutorial Session on Neutron Scattering

International Conference on Atomic Collisions in Solids (ICACS)

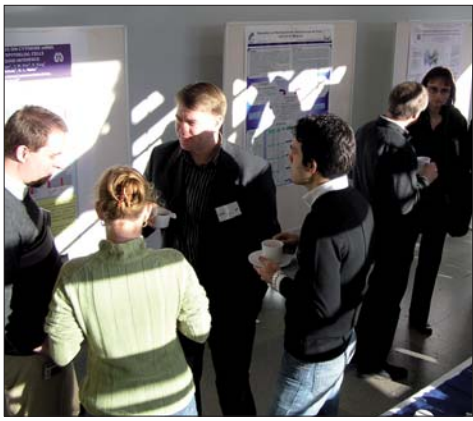

5th Workshop on Metallo- and Metalloid proteins (Herbsttagung)

Meetings, Conferences organized by HMI

Several meetings, schools and conferences have been organised at or by the Hahn-Meitner-Institut in 2006. A table presents an overview.

Event	Organized together with	Location	Dates
27th Tutorial Session on Neutron Scattering		Hahn-Meitner-Institut	27 February – 2 March
Meeting of the European Neutron Radiography Association 2006		Hahn-Meitner-Institut	17 March
International Conference on Atomic Collisions in Solids (ICACS)	Technische Universität Berlin	Technische Universität Berlin	21 – 26 July
Summer student programme		Hahn-Meitner-Institut	August/September
PNCMI School		Hahn-Meitner-Institut	19 – 22 September
PNCMI Conference (Polarised Neutrons for Condensed Matter Investigations)		Berlin	25 – 28 September
WINS2006 (Workshop on Inelastic Neutron Spectrometers)		Hahn-Meitner-Institut	29 – 30 September
5th Workshop on Orbital Physics and Novel Phenomena in Transition Metal Oxides	University of Hamburg	Hahn-Meitner-Institut	5 – 6 October
5th Workshop on Metallo- and Metalloid proteins (Herbsttagung)	GSF – National Research Center for Environment and Health	Hahn-Meitner-Institut	6 – 7 December

HMI's new Neutron Guide Hall II. Currently, two new neutron scattering instrument are being built up in this hall

User Service

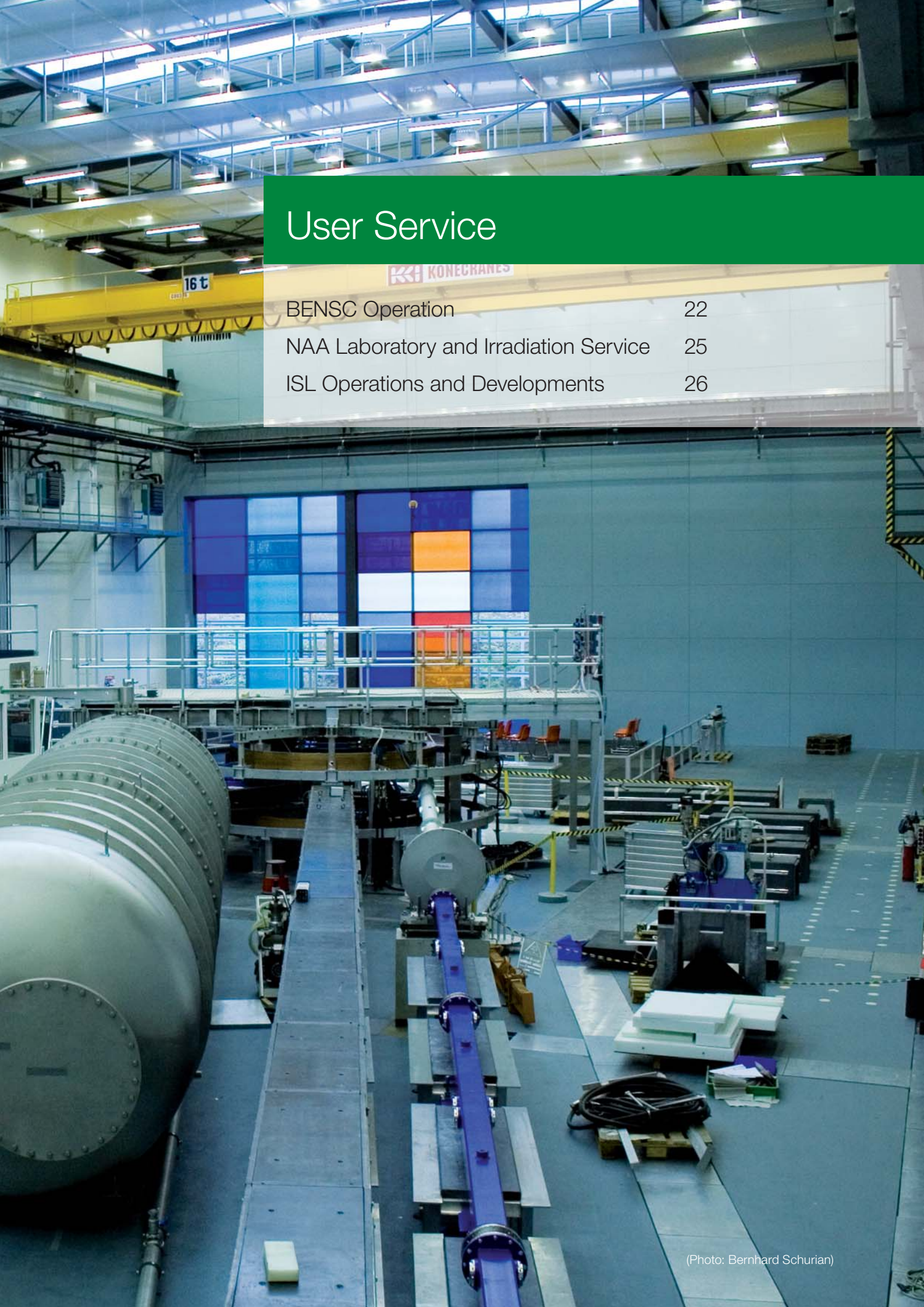

(Photo: Bernhard Schurian)

BENSC Operation

Director: Ferenc Mezei

It is the mission of the Hahn-Meitner-Institut as a research centre of the Helmholtz Association to operate large-scale facilities for providing best state-of-the-art research opportunities for the national and international user community. The Berlin Neutron Scattering Center (BENSC) was established at the HMI to accomplish this task for the neutron research community and more recently also for users of synchrotron radiation with a particular focus on promoting the complementary use of both probes: neutrons and photons. BENSC is characterised by two important strengths: extreme sample environment providing the world's highest magnetic fields and lowest temperatures in neutron scattering and development of new instrumentation concepts and techniques both for continuous and pulsed neutron sources. As a result, experimental capabilities at several BENSC instruments are unique or competitive with the best at high-flux sources. Other BENSC instruments provide solid performance for a nearly complete spectrum of neutron scattering studies, for purposes of both high quality research and education of students and new neutron users. The BENSC user programme has always been highly rated and is strongly supported by the EU since 1993.

BENSC Instrumentation

BENSC is characterized by an extraordinarily wide-ranging instrumentation, which is remarkable for a medium flux neutron facility. With the exception of a backscattering machine, a complete spectrum of instrument types allows experiments to be performed in practically all areas of neutron science, from basic to applied research. At present, 14 instruments are offered to users on a regular basis. These are five thermal diffractometers (E2 – flat-cone, E3 – residual stress, E4 – single crystal, E6 – single crystal and powder, E9 – powder), one cold diffractometer (V1), a thermal three-axes spectrometer (E1), a cold three-axes spectrometer (V2 – FLEX), a time-of-flight spectrometer (V3 – NEAT), a small-angle scattering instrument (V4), a spin-echo spectrometer (V5 – SPAN), a reflectometer (V6), a tomography station (V7 – CONRAD) and a USANS/tomography instrument (V12). Two more user instruments are presently being installed in the new Neutron Guide Hall II – the extreme environment diffractometer EXED and the high-resolution small-angle diffractometer VSANS. The next commissioning of these two novel instruments is forseen for end of 2007 / beginning of 2008.

BENSC User Programme

BENSC operates a comprehensive user programme at these 14 instruments. About 70% of the beam time at each instrument is offered to external users, 30% to in-house researchers. A minor part of the beam time for external users (up to 20% of the total beam time of an instrument) can be given to long-term collaborating groups from German universities and other research institutions, the rest (at least 50% of the total beam time) is allocated to short-term projects. The long-term collaborations serve mainly two purposes: (i) they allow university groups a reliable planning of thesis works and (ii) they enlarge the pool of scientific expertise available at BENSC. Scientifically extremely fruitful collaborations of this kind exist with the universities of Tübingen, Darmstadt, Kassel, Berlin, with the Max-Planck institutes at Golm (Potsdam) and at Stuttgart and with the reactor centre of Gatchina (St. Petersburg, Russia).

The beam time allocation is based on a proposal system with two proposal rounds per year. Proposals for short-term projects submitted by external users are peer-reviewed by an international Scientific Selection Panel which is meeting at the HMI to discuss and evaluate the proposals. Following the decisions of the Scientific Panel, proposers of accepted short-term projects are invited to perform the proposed experiment at BENSC free of charge. Proprietary research by commercial companies is also possible at request, mainly at special instruments, but this will be charged.

BENSC provides extensive technical and scientific support for all external users at the scheduled instruments. The instrument scientists assist in preparing and performing the experiments and in the data evaluation process. Advanced sample environment such as high-field cryomagnets or high-temperature furnaces is operated by experts from the sample environment group. BENSC also provides extensive logistic support. It runs a 30 bedroom hostel on site and assists external users by contributing to travel and subsistence expenses, whereby users from German universities get preferential treatment. Users from EU member states and associated states are eligible for grants provided by the European Commission. EU users can get full travel refund for up to two participants per experiment.

User statistics for 2006

In 2006, 254 short-term proposals were submitted to BENSC, 160 have been accepted by the Scientific Selection Panel of BENSC. Out of these, 155 were executed in 2006 by 299 visitors (233 individual researchers) using 1059 out of 2574 instrument days. In addition, 11 long-term projects and 81 internal projects were performed. The distribution of the different kinds of projects over the totally available beam time of 2574 instrument days is displayed in Fig. 1.

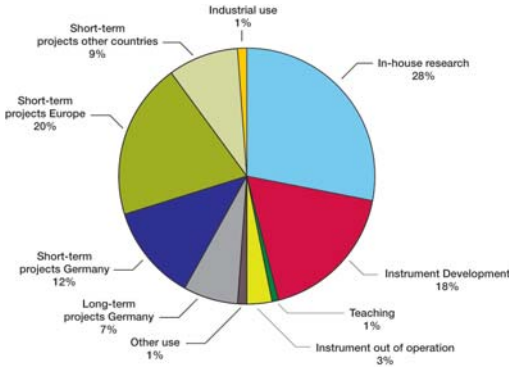

Fig. 1: The share of beam-time for the different kinds of projects in 2006. The percentage figures relate to the totally available beam time of 2574 effective instrument days.

Research fields covered external projects

Fig. 2 displays the research fields covered by the external projects (including long-term projects) in 2006. The figure demonstrates the particular attractiveness of BENSC for researchers working in the field of magnetism. This is certainly due to the special sample environment BENSC offers to its users: highest magnetic fields in combination with lowest temperatures, unmatched world-wide. Throughout all the last years the beam-time share of magnetism projects was around 40%. With regard to 2006 one has to keep in mind that the statistics is slightly biased, because two instruments, which traditionally have a high proportion of magnetism projects, were only part-time operational in 2006. This underlines that magnetism is the most important field for the external BENSC users. It is, however, also interesting to see that Soft Matter & Biology is continuously increasing, from 24% in 2002 to 29% in 2006. This can be traced back to the fact that four instruments in the old neutron guide hall, the membrane diffractometer V1, the time-of-flight spectrometer V3 (NEAT), the small-angle scattering machine V4 and the reflectometer V6, have succeeded in attracting a growing user community from this very dynamically developing field.

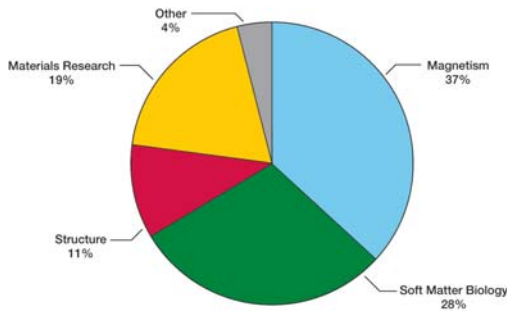

Fig. 2: The research fields covered by external projects (including long-term projects) performed at BENSC in 2006.

	Projects	Visitors
Germany	43	93
Europe	83	153
Russia	8	12
Others*	21	41
Sum	155	299

*Australia, India, Japan, Mongolia, Ukraine, U.S.A

Table 1: Short term projects performed at BENSC in 2006 listed according to the origin of the proposer groups.

Table 1 shows the origin of the groups performing the short-term projects with respect to the institution the main proposer is affiliated to. In contrast to individual researchers the number of visitors is based on multiple counting of the same person if present at more than one experiment per year (corresponds to number of visits). Table 1 clearly demonstrates that BENSC has established itself as a truly international, world-wide recognised centre for neutron science. This is due to the unique opportunities offered by the neutron instrumentation and sample environments of BENSC, but also to the particular service provided at the instruments. Even scientists from overseas countries with own strong neutron sources such as the USA and Japan come to BENSC to perform experiments. It is especially the high field sample environment, which attracts these users. Many of their experiments resulted in publications in high-ranked journals. A large part of the European users could be supported by the NMI3 access programme to large-scale facilities of the European Commission under contract number RII3-CT-2003-505925 which is gratefully acknowledged by BENSC. From 2004 to 2006, 365 individual users performing 228 projects benefited from this European programme.

Output of BENSC – publication record
Each short-term project carried out at BENSC must be followed by an Experimental Report within due time. The call goes out at the end of the year. For continued projects, the report on the predecessor project is prerequisite for the allocation of further beam time. The contributions to the Experimental Report are short descriptions of the experiments performed and the data obtained. It is clear that the results given in the reports can often only be preliminary. The reports are collected and published annually as BENSC Experimental Reports. They are distributed to all users of BENSC and give a complete overview on the scientific activities at BENSC. Starting with the year 2000 the BENSC Experimental Reports are also available on the BENSC web pages (http://www.hmi.de/bensc/user-info/reports.htm).

BENSC's share in the production of neutron scattering results published in recognised quality journals is outstanding compared to its size and neutron source power. A scientific focus of BENSC user publications in highly ranked journals is the field of magnetism. This particular strength of BENSC also becomes apparent at national and international conferences, where BENSC contributions to the field of magnetism often play a dominant role. At the European Conference on Neutron Scattering 2003 in Montpellier the BENSC share in the field of magnetism was more than 20%, at the last national conference, the SNI 2006 in Hamburg which was a joint meeting of users of synchrotron, neutron and ion beam radiation, the BENSC share in the field of magnetism was 30%.
Two examples of highlight results from external user groups are included in the Scientific Highlights Section of this Report.

Contribution of BENSC for educating young scientists
A minimum of 4 diploma theses and 23 PhD theses were based on experiments performed at the neutron facilities of BENSC in the years 2005 and 2006 (the true figures are higher, since not all achievements of diploma and PhD theses are communicated to BENSC). Once a year, a neutron tutorial is held with lectures and practical exercises, allowing students and postdocs from all over Europe hands-on training at the neutron scattering instruments of BENSC.

Additional services of BENSC
BENSC has built up additional laboratory services for its users which are becoming increasingly important. The laboratory for soft-matter and biological samples is frequented by more than 30% of all users of the instruments in the neutron guide hall for preparing their samples and making additional measurements. More recently, a laboratory for physical properties measurements (LaMMB, Laboratory for Magnetic Measurements at BENSC) with a state-of-the-art PPMS system and highly-specialised instrumentation for specific heat measurements has been opened for users. A throughput of 59 samples from 13 internal and 6 external users in 2006 demonstrates the attractiveness of this additional BENSC service. Presently, these services are expanded by installing a state-of-the-art laboratory system for adsorption measurements allowing users to perform additional experiments in parallel to investigations by e.g. neutron small-angle scattering.

Fig. 3: Tutorial on neutron scattering in 2006

Fig. 4: Laboratory for Magnetic Measurements at BENSC – LaMMB

Neutrons and photons from BENSC
In particular to promote the complementary use of neutrons and synchrotron radiation, BENSC is engaged at the Berlin Synchrotron Radiation Source BESSY with three beamlines in the framework of a CRG programme: at the undulator UE46 it operates a world-leading soft x-ray beamline with two end stations, a spectroscopy chamber and a high magnetic field reflectometer. At the 7T Wiggler, BENSC operates two beamlines, one specialised on residual stress measurements and one with two experimental options: (i) a resonant magnetic scattering instrument and (ii) an instrument for anomalous small-angle and grazing incidence scattering. An x-ray tomography instrument installed at a non-HMI beamline allows investigations complementary to the neutron tomography station of BENSC. User access to these BENSC operated facilities at BESSY is organised via the BESSY proposal system.

NAA-Laboratory and Irradiation Service

D. Alber, G. Bukalis, H. Kizilkay, B. Stanik (SF6)

Fig. 1: Granules of pure Silicon enclosed in ampoules made of highly pure silica.

The laboratory for neutron activation analysis (NAA) at HMI's research reactor BER II provides irradiation services for universities, scientific institutions and industry. Typical fields of applications are:

- Trace element analysis by means of neutron activation analysis (NAA) for example in biology, medicine, geology and archeology. Certification of reference materials.
- Irradiation experiments, such as isotope production for medical applications, sources for Mößbauer spectroscopy and production of tracers for scientific and industrial applications. The operation and further development of the irradiation devices at BER II and of the NAA measuring systems are a central task of the department SF6.

Irradiation devices

Three irradiation devices are available for different applications.

DBVK: irradiation device in the reactor core
DBVR: rotatable irradiation device in the Be-reflector of the reactor core
TBR: dry irradiation device outside the Be-reflector

Device	$\Phi_{thermal}$ [1/cm^{2}s]	Φ_{fast} [1/cm^{2}s]	Container
DBVK	1,5E+14	4,3E+13	6
DBVR	7,5E+12	1,9E+10	9
TBR	3,4E+12	2,2E+10	1

Table 1: Fast and thermal neutron flux at different irradiation positions

DBVK and DBVR are used for long term irradiation experiments. Up to 9 aluminum containers can be irradiated simultaneously. Short time irradiation experiments are carried out by means of TBR. A fast rabbit system (SRT) is closed for the time being.

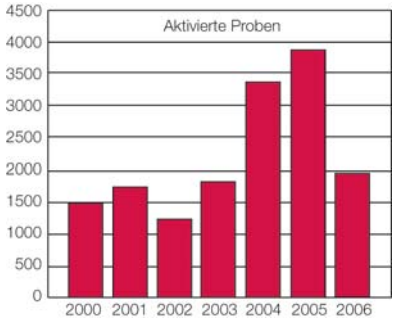

Fig. 2: Statistics of irradiated samples.

Irradiation Experiments 2006

A total of about 1900 samples were irradiated in 2006. Most of the 221 irradiation experiments were performed with the DBVK or DBVR. With these devices it is possible to irradiate up to 24 samples simultaneously in one aluminum container.

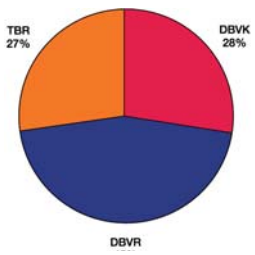

Fig. 3: Utilization of the different Irradiation devices.

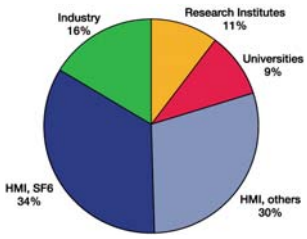

Fig. 4: Origin of Samples irradiated in 2006

About 48% of the irradiation experiments and the analysis of samples were done for external users. Most of the internal users are from the Dept. SF6, but irradiation and analyses were also performed for users from other departments (SF2, SF4, SE5, Reactor department).

External users

Irradiation experiments and NAA were performed for users from the German universities (Berlin, Mainz, Münster, Leipzig, Nuremberg) and from research institutes like BAM (Berlin), GSF (Neuherberg), and Fraunhofer Institute (Dresden).

ISL Operations and Developments

Scientists: A. Denker, H. Homeyer, W. Pelzer, C. Rethfeldt, J. Röhrich,
Operators: J. Bundesmann, R. Grünke, G. Heidenreich, H. Lucht, E. Seidel, H. Stapel

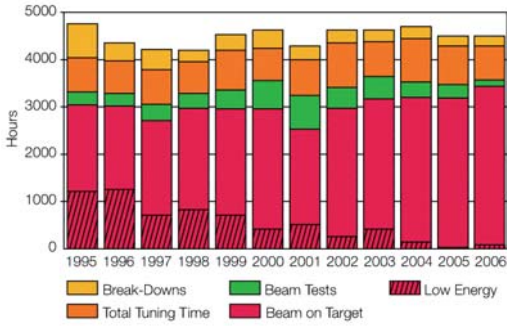

Fig. 1: ISL operations since 1995: it is very stable over the past ten years. In 2006, the maximum beam time on target ever produced was achieved, although the scheduled beam time was less than in previous years.

Following the decision of the board of directors, 2006 was the last year of operation at HMI's ion beam laboratory ISL. In spite of that, ISL operations went extremely well in 2006 (see Fig. 1). This was due to the efforts of the accelerator crew and the result of improvements concerning the reliability.
ISL offered ion-beams from various accelerators and accelerator combinations with energies ranging from some tens of eV to several hundred MeV dedicated to the application of ion-beam techniques. Internal and external users studied the basics of the interaction of ions with solids. They modified and analysed materials with ion beams and they performed radiotherapy of eye tumours with fast protons in a joint venture with university clinics. Users had at their disposal 15 different irradiation areas equipped with specific instrumentation.

The second ion source for the RFQ, installed in 2005, allowed shorter tuning times, as one source could already be started whilst the other one still delivered beam to the target. Within the scheduled operation time of 4400 hours, nearly 3500 hours of beam time on target were produced. The loss of scheduled beam time due to break-downs reached an all-time low of 4%. The high reliability of 96% was essential for a successful user program, in particular for the therapy of ocular melanomas with high energy protons. Like in last year, Au-ions and protons were the most attractive beams in 2006. Au-beams were used as projectiles for ma-

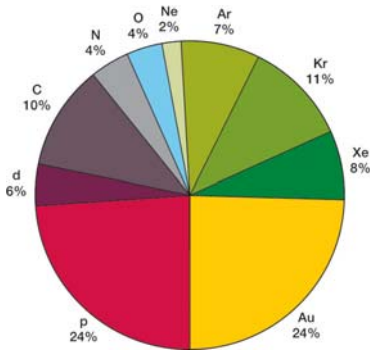

Fig. 2: Ions produced at ISL in 2006: Au-beams with a share of 37% are the most frequently used beams. Main applications are ion-beam analysis (ERDA) and ion-beam induced materials modifications.

terials analyses and ion-beam induced materials modifications. Apart from therapy, there was a large demand for high energy proton beams, either for high-energy PIXE, radiation hardness testing or device testing for hadron therapy machines.

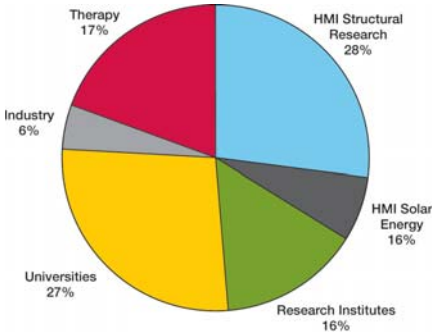

Fig. 3: Home institutions of ISL-users: HMI-activities (SF4 and solar energy) use about one third of the beam time. University based researchers used nearly one third of the beam time.

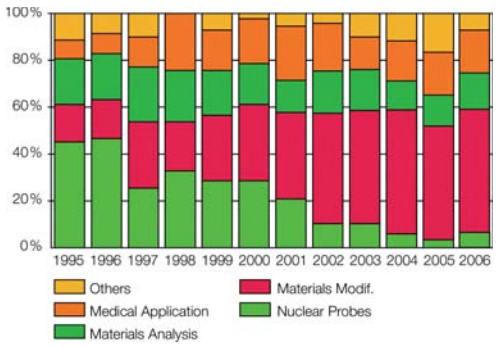

Fig. 4: Use of ISL ion beams: Materials modifications became the largest part of research and development at ISL. Most of the corresponding user groups came essentially from universities documenting ISL's importance for the FSI (*Forschung mit nuklearen Sonden und Ionenstrahlen*) community.

In total, 37 different projects involving more than 100 scientists received beam time in 2006. About 30% of the users came from universities, their main topic of research being materials modifications. Research groups of the HMI use one third of the beam time.

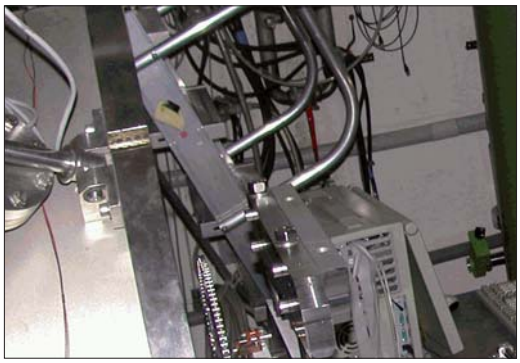

Fig. 5: Boards for satellite on-orbit servicing during the installation in the BIBER chamber. On these boards, radiation hardness tests were performed using a 5.6 MeV/u cocktail beam of Xe, Kr, Ar, and O ions.

It turned out that, since 2002, the relative share of beam time for the different ion-beam applications at ISL has been relatively stable (see fig. 4). Materials analyses with an average of 15% of the beam time were performed exclusively with fast ions. The ERDA method used the heaviest ions to determine, among others, the stoichiometry of thin layers for HMI's solar cells development programme. High-energy PIXE utilized fast protons preferentially for the analysis of objects d'art or archaeological samples. In addition, radiation hardness tests were performed using protons as well as heavy ion cocktails (see fig. 5). Eye tumour therapy was performed at 10 therapy blocks (5 days/block) for more than 150 patients. The total medical share of 15% includes beam time for the Helmholtz health programme Precision Proton Therapy. Since the start in 1998, a total of more than 800 patients have been treated at ISL.

The quota of "others" reflects guest activities in nuclear physics with high-energy heavy ion beams and the Q3D magnetic spectrometer. As shown in fig. 6, the amount of beam time used by external users varies slightly around 70%.

Most of the efforts undertaken in 2006 were dedicated to keep the reliability of the facility in general and to deliver as much beam as possible in order to allow our users to finish their experiments.

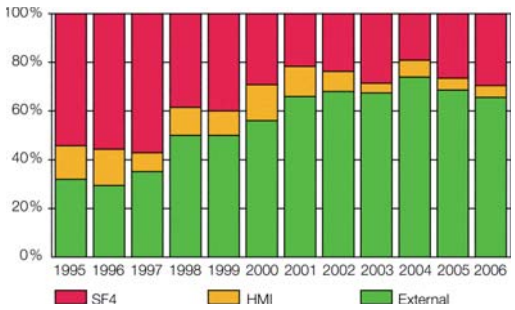

Fig. 6: User Facility ISL: Development into a user facility. External users including proton therapy had a stable share of about 70% in the past years.

In December 2006, a „final colloquium", reviewing the impact of ISL on accelerator technology, the role of ion beams as shaping tools for the nano world, their analytical power for understanding and preserving our cultural heritage, and their use in tumour therapy, once again demonstrated the broadness and the success of the ISL activities.

Thus, a very fruitful phase of research using fast ions comes to an end. We thank our users for exciting experiments and the ISL accelerator crew for their endeavours.

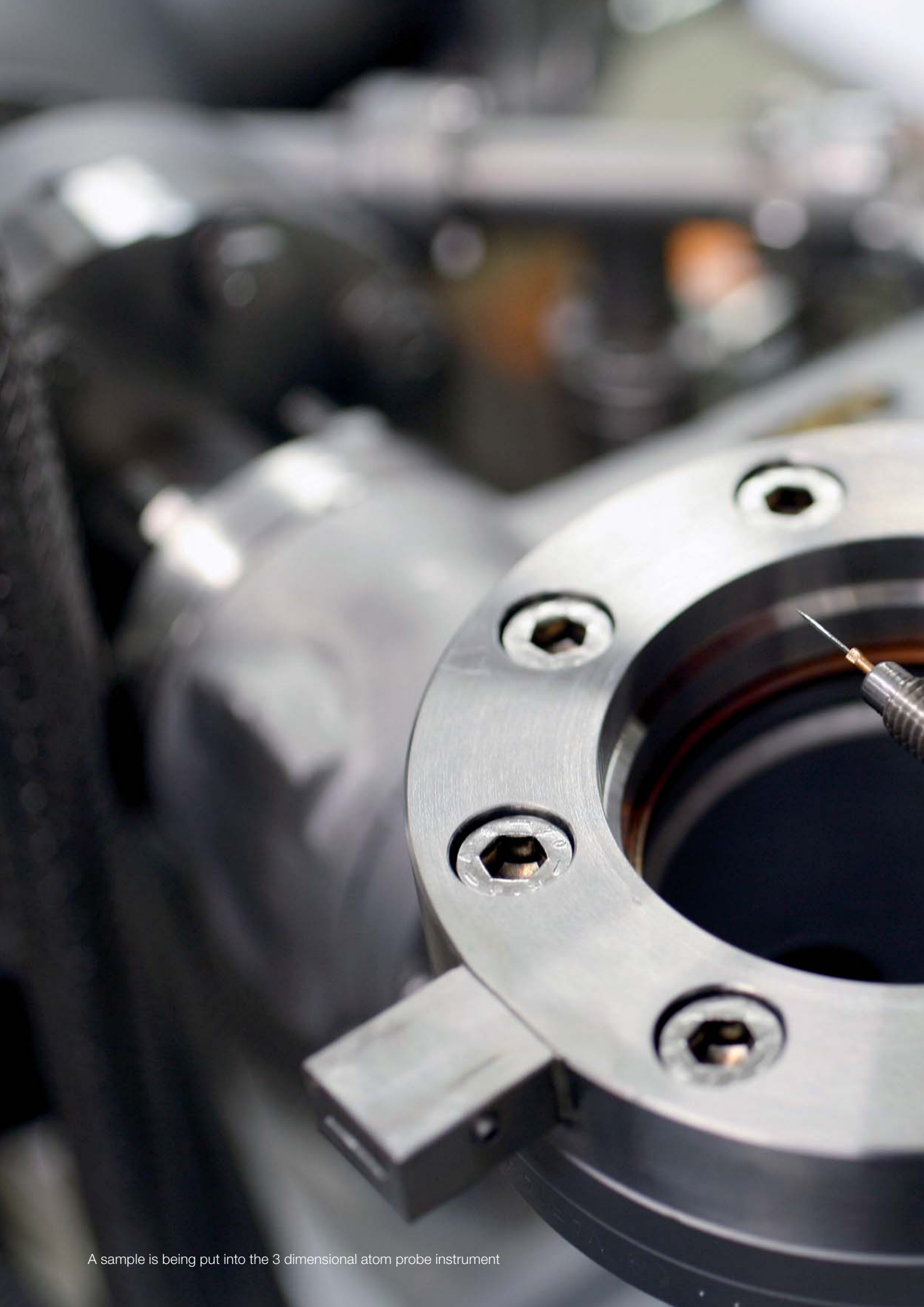

A sample is being put into the 3 dimensional atom probe instrument

Scientific Highlights
Structure Research 2006

(Photo: Bernhard Schurian)

Are cold neutrons cool enough to help us get home faster?

L.P. Aldridge[1] H.N. Bordallo[2], A. Desmedt[3]

■ 1 Materials & Engineering Science ANSTO School of Civil and Environmental Engineering, UNSW, Australia ■ 2 HMI, SF6 ■ 2 Groupe de Spectroscopie Moléculaire, ISM, Université Bordeaux 1, France

Fig. 1: Remedial treatment to plastic cracking in a new bridge deck prior to opening.

In 2005, more than 5 billion tons of concrete were made. Well-made concrete has a long service life, and it should be possible to build structures that are almost maintenance free from it. However, due to poor concrete technology many structures deteriorate. For example, some bridge decks need maintenance after seven years of exposure to salt either from de-icing or marine sources. These repairs can be costly – for example, in the USA, it has been estimated that over a billion dollars need to be spent each year to repair concrete bridge decks.

The key to making durable concrete is to limit the ability of concrete to transport fluids (like water)[1]. Poorly made concrete will have cracks and pores allowing water to travel easily through, while in well made concrete it is more difficult for water to penetrate. Concrete is made from cement paste and a number of inert aggregates and in un-cracked concrete it is the cement paste that will transport the water.

As cement hydrates, sets and hardens, it forms pores which are classified either as “capillary pores”, if the pore diameter is larger than 100Å, or “gel pores” for the smaller pores. When the water content in the paste is such that the water to cement ratio (w/c) is less than, and the paste is properly cured, then the capillary pores become discontinuous. Then it is the gel pores that will limit water transport in concrete.

This joint research between the Hahn-Meitner-Institut (HMI) in Berlin, the IMES Australian Nuclear Science and Technology Organization (ANSTO) and the School of Civil and Environmental Engineering, University of New South Wales in Sydney, Australia combines practical work on large

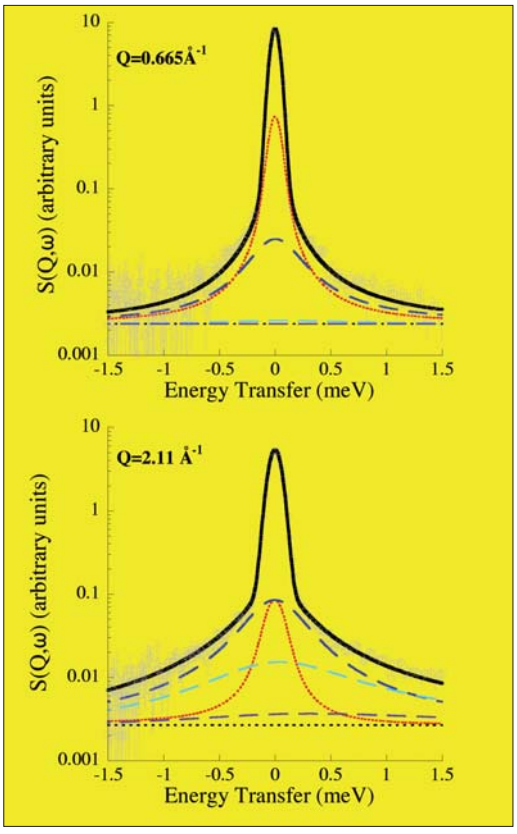

Fig. 2: Examples of experimental spectra (○) at selected Q-values for the cement paste with w/c=0.42, ΔE=98μeV, together with the best fit (solid line) and the quasi-elastic components (dotted lines represents the translational component and the long dashed lines represents the first three terms of the Sears expansion used to describe the rotational motion). The background is also shown (short dashed line).

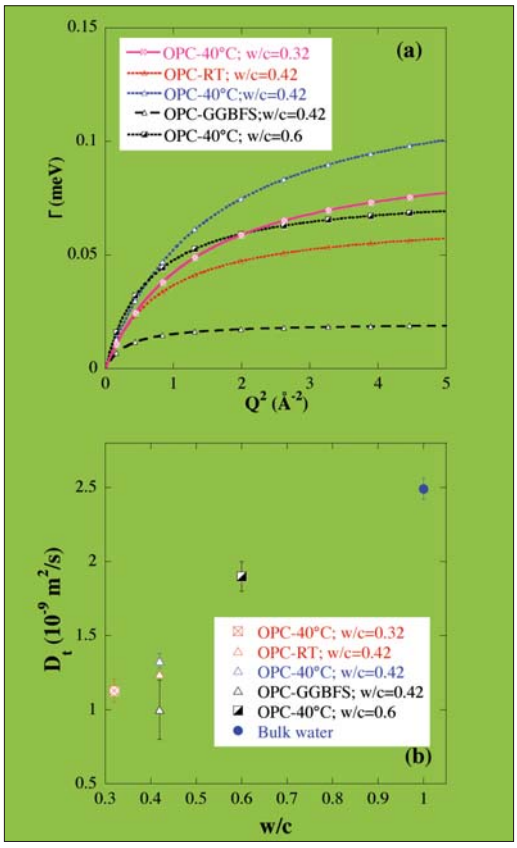

Fig. 3: (a) Line-width (Γ, HWHM) as a function of Q^2 of the quasi-elastic component for water contained in cement pastes, using 5.1 Å neutrons, with $\Delta E = 98$ μeV The solid lines are fit to the data using the model of Singwi and Sjölander.[2,3] (b) Self-diffusion coefficient (D_t) vs w/c content for the different pastes.

concrete blocks with measurements on small samples to determine how water moves in the hardened cement paste.

In complex systems such as hardened cement pastes, it is neither easy nor straightforward to determine the origin of the observed differences in the dynamical behavior of the water molecules. However, quasi-elastic neutron scattering (QENS) has been used to estimate the dynamics of confined and interfacial water. Using HMI's time-of-flight spectrometer NEAT, we have performed a series of QENS experiments to investigate the dynamics of water in the pores within the cement paste. It was possible to measure the diffusion of water in 1 g of paste.

QENS spectra of a number of different cements have been measured and analyzed as outlined in Bordallo et al [4] in terms of rotation and long range translational motion. The quasi elastic widths (Γ) plotted as a function of Q^2 are shown in Figure 3(a). From the slope we calculated the translational diffusion of water while the saturation values at higher Q's gave the rotational values. This approach indicates that at least two diffusion processes occurred. A fast diffusion is most likely attributable to the water confined in the capillary pore structure ($D_t \sim 10^{-9}$ m^2/s) and a slower diffusion is probably due to gel pore water ($D_t \sim 10^{-10}$ m^2/s). In addition from high-resolution backscattering measurements a slower motion was also detected, that could be associated with a long-range translational diffusion [5].

Our work [4] distinguishes between three different types of water confirming the interpretation of previous NMR experiments [6]. Thus QENS is able not only to distinguish between the types of water but it also quantifies the rotation and diffusion of this water. Pastes made under different conditions (i.e. with Ground Granulated Blast Furnace Slag (GGBFS), or different water/cement ratios (w/c) or cured at room temperature (RT) or 40°C) give significantly different diffusivities as shown in Figure 3(b).

The long term aim of the work is to develop tests that show the "fitness for purpose of concrete" within the first week of concrete setting. Such tests can only take place if the role of water in the gel pores is understood. When this is achieved, then "in-situ" tests may be developed to show if the concrete has been properly cured and compacted. Then estimates of the durability of concrete could be made on site during construction. Thus maintenance-free concrete bridge decks could be built and such frequent bridge repairs will no longer be needed. So if cold neutrons are cool enough to measure the slow diffusivity of water in cement paste, tests will be developed so less reconstruction is needed. Perhaps then neutrons will have helped us get home faster from work.

[1] S. Mindess, J.F. Young, D. Darwin, in Concrete - 2nd ed.; Prentice Hall, 2003
[2] K.S. Singwi and A. Sjölander, Phys. Rev., **119**, 863 (1960)
[3] M. Beé, in Quasi-Elastic Neutron Scattering; Adam Hilger, Bristol, Philadelphia, 1988
[4] H.N. Bordallo, L.P. Aldridge and A. Desmedt, J. Phys. Chem. B, **110**, 17966 (2006)
[5] L.P. Aldridge, H.N. Bordallo and A. Desmedt, Physica B, **350**, e565 (2004)
[6] J. Greener, H. Peemoeller, C. Choi, R. Holly, E.J. Reardon, C.M. Hansson and M.M. Pintar, J. Am. Ceram. Soc., **83**, 623 (2000)

Corresponding authors:
L.P. Aldridge
laurie.aldridge@gmail.com
H.N. Bordallo
bordallo@hmi.de

Magnetic excitations in the magnetically ordered phases of PrB_6

K. A. McEwen[1], M. D. Le[1], K. C. Rule[2], J-G. Park[3], S. Lee[3], F. Iga[4]

■ 1 Department of Physics and Astronomy, University College London, UK ■ 2 HMI, SF1
■ 3 Department of Physics, SungKyunKwan University, Suwon, Korea ■ 4 Department of Quantum Matter, Hiroshima University, Japan

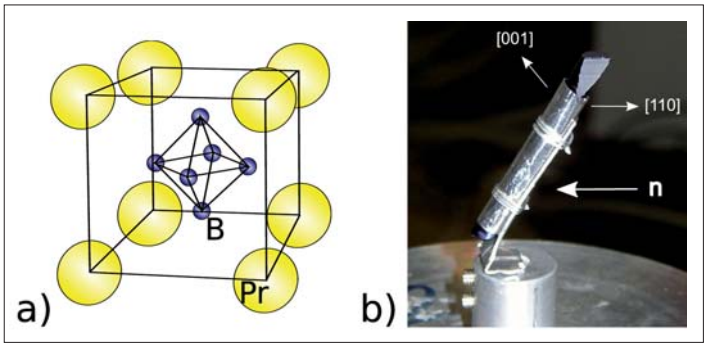

Fig. 1: (a) Crystal structure of PrB_6; (b) The single crystal of PrB_6 as oriented and mounted for the zero field experiments.

The RB_6 family of intermetallic compounds exhibit a particularly interesting range of electrical and magnetic properties, as the number of 4*f* electrons in the rare-earth (R) element increases. At the start of the rare-earth sequence, La has no 4*f* electrons and so is non-magnetic, but displays superconductivity at low temperatures. The single 4*f* electron in CeB_6 is strongly hybridised with the conduction electrons, leading to an enhanced effective mass and showing the characteristic "heavy fermion" behaviour in its electrical resistivity, heat capacity and magnetic susceptibility at low temperatures. CeB_6 does not exhibit ordering of its magnetic dipole moments, but instead the electric quadrupole moments of the 4*f* electrons develop long-range ordering below 3.3K. The various quadrupolar phases of CeB_6 have been extensively studied. However, with two 4*f* electrons, PrB_6 does show long-range ordering of the magnetic dipole moments, as do the remaining members of the RB_6 family (with the exception of divalent EuB_6 and mixed-valent SmB_6).

The crystal structure of PrB_6, like the other RB_6 compounds, is rather straightforward, consisting of a cage of Pr^{3+} ions in a simple cubic structure, with an octahedron of boron atoms within this cage (see Fig. 1a). The aim of our neutron scattering experiments at HMI has been to investigate the magnetic excitations in PrB_6 and hence to determine the magnetic interactions between the Pr ions in this system.

The crystal used for our experiments (shown in Fig. 1b) was grown at Hiroshima University in Japan by means of a floating-zone method. Natural boron comprises an approximately equal mixture of the isotopes ^{10}B and ^{11}B. Since ^{10}B strongly absorbs thermal and cold neutrons, our PrB_6 crystal was prepared using boron enriched to 99% of the non-absorbing ^{11}B isotope.

Earlier neutron diffraction experiments have revealed the magnetic structures of PrB_6. At the lowest temperatures, below 4.2K, the Pr moments orders in the magnetic structure shown in Fig. 2a. This comprises two coexisting chains of antiferromagnetic moments directed at right angles to each other along [110] and $[1\bar{1}0]$ in a so-called *commensurate double-q structure*, with associated wave vectors [¼ ¼ ½] and $[¼\ \bar{¼}\ ½]$. Between 4.2K and 7.0K the system adopts the *incommensurate double-q structure* shown in Fig. 2b, where the periodicity of the magnetic moments is no longer an integer multiple of the lattice periodicity. The application of a magnetic field simplifies the structures considerably. Above a field of 2 tesla, we find the *commensurate single-q* magnetic structure shown in Fig. 2c, with all the magnetic moments perpendicular to the magnetic field direction.

Our inelastic neutron scattering experiments have been carried out using the V2/FLEX triple-axis spectrometer. The Pr^{3+} ions have a total angular momentum J=4: the 9-fold degeneracy of the ground $^3H_4$ multiplet is removed by the cubic crystalline electric field into a singlet, a doublet and two triplet states. The ground state is the Γ_5 triplet with a first excited Γ_3 doublet at 27meV. In the magnetically ordered phases, the Γ_5 triplet is itself split by the molecular (internal) field. Hence the low energy excitations in the ordered phases are expected to be due entirely due to spin waves from this splitting, which is ~1-2meV.

In our experiments we have mapped out the dispersion of these low energy excitations along the principal symmetry directions ([*h h* 1½] and [¼ ¼ l]) around the magnetic Brillouin zone centre at (¼ ¼ 1½). Fig. 3 shows the dispersion along [h h 1½], with a typical scan shown in Fig. 4a.

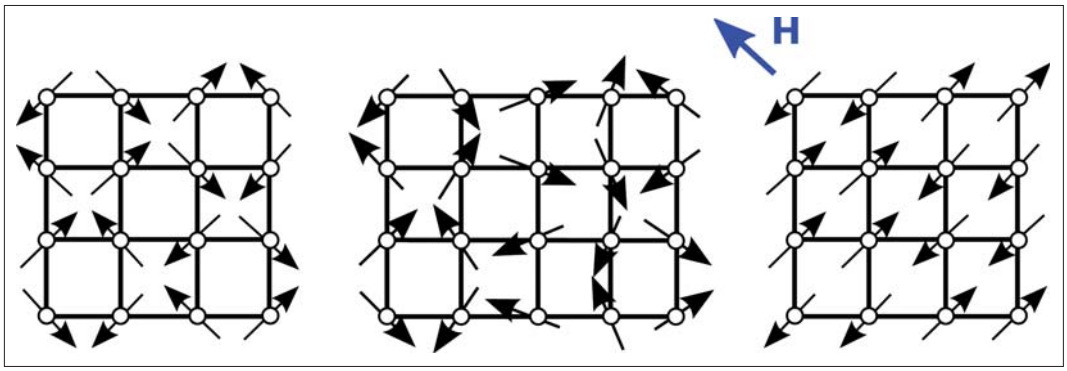

Fig. 2: Magnetic structures of PrB_6; (a) Commensurate double-q structure for T<4.2K; (b) Incommensurate double-q structure for 4.2K<T<7K; (c) Commensurate single-q structure for fields above 2 tesla along the direction shown.

Three modes are clearly observed at the magnetic zone boundary: the two lower energy modes merge near the middle of the zone. Analysis of these results shows that the dominant magnetic interactions are between nearest neighbour Pr ions, but that interactions up to fourth nearest neighbours are required to explain the dispersion relation in zero applied magnetic field.

As discussed above, the application of a magnetic field leads to a dramatic simplification of the magnetic structure. The dispersion of the excitations along [*h h* 1½] becomes significantly greater as can be seen in Fig. 3. Moreover, only a single mode is now observed: Fig. 4b shows that two of the modes seen in Fig. 4a are suppressed by the magnetic field. The nearest neighbour interaction now almost completely dominates which is reflected in the change in structure.

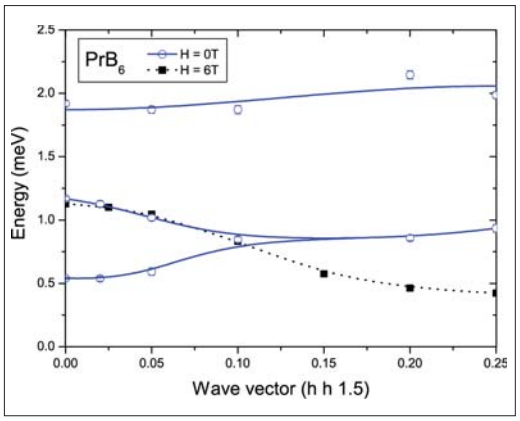

Fig.3: Dispersion of the magnetic excitations in PrB_6 at 2K. The open blue symbols show the zero field results. The filled black symbols show the results in a field of 6 tesla. The lines are guides to the eye.

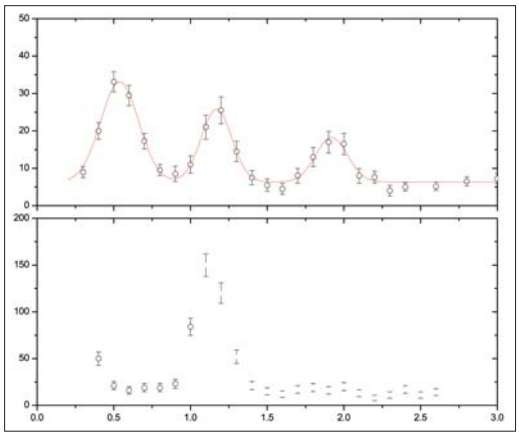

Fig.4: Typical inelastic neutron scattering spectra for PrB_6 at 2K. The data at the wave vector Q=(0 0 1.5) show that two of the three excitations in zero field are suppressed by a field of 2 tesla.

The combination of the high resolution triple-axis spectrometer and the availability of high magnetic fields at HMI have been essential in our investigations. Although the Pr ions are on a very simple structure, nevertheless the competing interactions (crystalline electric field, exchange, Zeeman and quadrupolar) lead to surprisingly complex magnetic structures. For further details, see [1]

[1] M.D. Le, K.A. McEwen, J-G. Park, S. Lee, F. Iga, K.C. Rule, submitted to *J. Phys: Condens. Matter.*, July 2007.

Corresponding author:
K. A. McEwen
k.mcewen@ucl.ac.uk

Analysis of restricted elements in plastics using XRF

C. Mans, S. Hanning, C. Simons, A. Wegner, A. Janssen, M. Kreyenschmidt
■ **Fachhochschule (University of Applied Sciences) Münster, Fachbereich Chemieingenieurwesen, Steinfurt, Germany**

Fig. 1: In a few years, even this computer will become old and contribute to the problem of electronic waste containing hazardous materials.

X-ray fluorescence analysis (XRF) has proved to be a powerful tool for a huge variety of analytical tasks in industry. One new area of application is related to the implementation of the EU directives *Restriction on use of certain hazardous substances (RoHS) [2002/96/EG]* and *Waste Electrical and Electronic Equipment (WEEE) [2002/95/EG]* which have been implemented in Germany in form of the Elektrogesetz. According to these directives, the concentrations of polybrominated biphenyls and polybrominated diphenyl ethers, lead, chromium(VI), mercury and cadmium in electronic and electrical equipment are restricted since 01.06.2006. Furthermore, all used electronic and electrical products have to be taken back and disposed by their producers. These new laws and restrictions cause technical problems as well as new challenges for the product developer as they create a need to evolve fast and economically suitable analytical tools to control a product's quality and to facilitate compliance with these regulations.

The challenge for the development of such an analytical tool is related to the large variety of materials used in this field of electronic applications. The chemical analysis of the restricted compounds might therefore be accompanied by enormous problems. Commonly used analytical methods for the determination of the regulated elements are Inductively Coupled Plasma Atomic Emission Spectroscopy (ICP-AES), Inductive Coupled Plasma Mass Spectroscopy (ICP-MS) or Atomic Absorption Spectrometry (AAS). Unfortunately these techniques require generally liquid samples. Therefore, the samples have to be digested – nowadays mostly using microwave digestion. The demand on the digestion procedure is that the material has to be brought completely into solution, which is time-consuming and costly. Furthermore the unavoidable dilution of the sample leads to a drastic rise in detection limits. For these reasons, the aim of a research project at the Laboratory for Instrumental Analysis of the University of Applied Sciences Münster was to develop an analytical method which allows the direct characterization of certain plastic materials according to EU-directives RoHS/WEEE without foregoing sample digestion.

An available analytical method which matches these demands is the X-Ray Fluorescence Analysis (XRF). Unfortunately, this method is strongly limited by the need for suitable standard materials for the calibration. In technical literature, various attempts to produce such standard materials are described. There are some standard materials available for purchase, but these are often restricted in their applicability to the RoHS/WEEE. Frequently the available materials do not contain all restricted elements and do not cover the whole concentration range necessary for the calibration. Furthermore they are available only with polyvinyl chloride (PVC) or polyethylene (PE) as matrix material, which is not sufficient for this wide range of polymer materials used in electronic industry. For these reasons, a special process was designed by the University of Applied Sciences Münster, which allows the production of plastic standards based on acrylonitrile-butadiene-styrene terpolymer (ABS), containing the regulated elements Br, Cd, Cr, Hg and Pb. ABS is a polymer commonly used as base material for e.g. housings in electrical and electronic industry. The standard materials were produced as granulates and solid bodies to potentiate the measurement of granulates as well as the measurement of bulk samples, which could be for example parts of housings etc.

Fig. 3: Produced ABS standard Materials (solid bodies) containing the regulated Elements Pb, Br, Hg, Cr, Cd

During the development of the production process it became apparent that it was impossible to add the restricted elements to the ABS without partial loss. Therefore the real concentrations of the added elements in the ABS had to be determined by alternative methods. For this special problem the Neutron Activation Analysis NAA provided by the Hahn-Meitner-Institut in Berlin was the method of choice, as especially

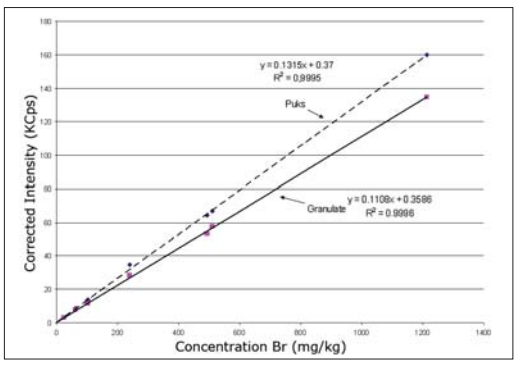

Fig. 2: Correlation of the Br-concentration in the produced standard materials determined by NAA and the measured intensities on S4 Pioneer

the determination of bromine in the ABS was not sufficient by other methods like ICP-AES or ICP-MS. NAA was chosen as this technique works without foregoing digestion of the sample and is regarded to be an absolute method.

The concentrations determined with ICP-AES (Pb) and NAA were used to calibrate the wavelength dispersive XRF S4 Pioneer (Bruker AXS) at the University of Applied Sciences Münster. The correlation of the XRF measurements with the values determined using ICP-AES and NAA showed a very good linearity as well for the produces granulates as for the solid bodies. As an example the calibration curve for Bromine is shown in Fig. 2.

The produced standard materials can be directly used to determine the concentration of the regulated elements in ABS. As determination of element concentrations in plastics is interesting for a lot of different fields in industry today, the production of further standard materials based on different plastic materials is focus of present and future research at University of Applied Sciences Münster. As these developments also need determination of the added elements by NAA, there will be a future cooperation of the Hahn-Meitner-Institut and the University of Applied Sciences Münster.

[1] C. Mans, S. Hanning, C. Simons, A. Wegner, A. Janssen, M. Kreyenschmidt, *Development of suitable plastic standards for XRF*, Spectrochimica Acta, Part B: Atomic Spectroscopy **62**B (2007) 116-122.
[2] C. Mans, S. Hanning, C. Simons, A. Janßen, M. Kreyenschmidt; *Kunststoffanalytik mit der RFA – Alles Plastik?*, Labor Praxis **10** (2006) 50-52, Journal in German

Corresponding author:
C. Mans
c.mans@fh-muenster.de

Composition profile of a wetting film in a binary liquid mixture

James Bowers[1], Ali Zarbakhsh[2], Hugo K. Christenson[3], Ian A. McLure[4], John R. P. Webster[5] and Roland Steitz[6]

■ 1 Department of Chemistry, University of Exeter, Exeter ■ 2 Department of Chemistry, Queen Mary, University of London, London ■ 3 School of Physics and Astronomy, University of Leeds, Leeds ■ 4 Department of Chemistry, University of Sheffield, Sheffield ■ 5 ISIS Facility, CLRC Rutherford Appleton Laboratory, Chilton, Didcot, UK ■ 6 HMI, SF1 and BENSC

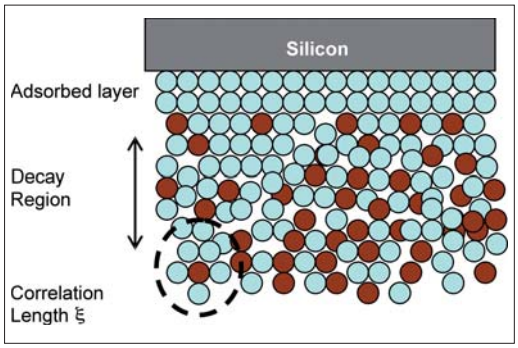

Fig. 1: Cartoon of the density in the boundary layer of a binary liquid mixture (represented by blue and brown spheres) against a solid wall (silicon substrate)

The wetting of surfaces in binary liquid mixtures has provided a rich area for fundamental studies of surface critical phenomena [1,2]. Hydrocarbon-fluorocarbon interactions are both of academic interest and practical importance with applications such as non-stick coatings, anti-graffiti paints and specialized lubricants and surfactants. Despite the absence of dipolar effects and hydrogen-bonding, alkane-perfluoroalkane systems are characterized by significant non-ideality and this gives rise to a miscibility gap with an upper critical solution temperature T_c (see Fig. 2). Close to the critical point long-range correlations in the bulk fluid dominate the adsorption behavior at a surface. Here, the density profile is expected to show universal behavior [3], decaying as an inverse power law close to the surface and showing exponential decay for distances exceeding the bulk correlation length ξ (see also Fig. 1).

Unlike the case with most liquid-vapor systems, the critical point in binary liquid systems is often at a convenient temperature and ambient pressure, thus providing ideal testing ground for theoretical predictions [1–5]. However, there are few experimental studies of wetting and adsorption in liquid-liquid mixtures away from the critical regime [2], in particular in the complete wetting regime, where adsorption is expected to be governed by long-range van der Waals forces. In our experiment at the neutron reflectometer V6 of BENSC, we studied the n-hexane and perfluoro-n-hexane system at a volume fraction of n-hexane $\phi_H = 0.25$ (in the complete wetting regime, far from the critical $\phi_H = 0.50$). See also crosses in Figure 2.

The reflectivity data obtained allowed for the determination of the composition profile of the wetting film [7]. Near the coexistence limit T_0, the composition of the liquid boundary layer was found to be different from the bulk fluid for distances up to $z \approx 100\text{-}120$ nm. The neutron reflectivity curves recorded from the system are displayed in Fig. 3. They show significant changes close to the critical edge (inset). The volume fraction profiles derived from the multilayer fits in Fig. 3 are shown in Fig. 4a. Far from coexistence, i.e. $T/T_c > 1$, there is a thin adsorbed film with the hexane content decaying exponentially towards the bulk. As T approaches T_c the decay length of the exponential increases as does the hexane content. For $T < T_c$ the decay length remains constant but the thickness and n-hexane content of the film increase with decreasing T. Furthermore, the advancement of the critical edge indicates the presence of a long-range effect on the density profile. There must be an extensive region with n-hexane content greater than that of the bulk, but

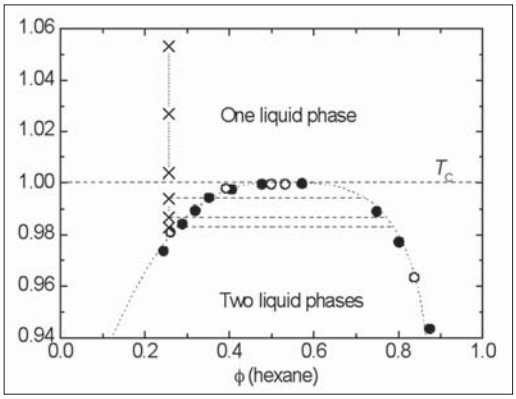

Fig. 2: Phase diagram displayed as T/T_c against the hexane volume fraction for the mixtures n-hexane-h_{14} (•) or n-hexane-d_{14} (o) + perfluoro-n-hexane. The dotted curve is the common curve for this and related mixtures [6]. The (x) are experimental points and the horizontal lines determine the composition of the hexane-rich phase at coexistence.

different from that of the wetting film that emerges at the coexistence limit. Only in the inner region, next to the substrate surface, does the composition of the film approach that of the n-hexane-rich phase, which phase separates at T_0 (or $T/T_c = 0.98$ for $\phi_H = 0.25$, see Fig. 2). The horizontal regions of the profiles for small z result from minimising the number of parameters in the fitting procedure.

The reflectivity curves were fitted using three modeling strategies, resulting in profiles displaying very much the same characteristic features (Figure 4). The profiles in Fig. 4b and 4c give the same high-quality fits to the reflectivity data as the fit shown on Fig. 3, which corresponds to the profile in Fig. 4a. All profiles show the growth

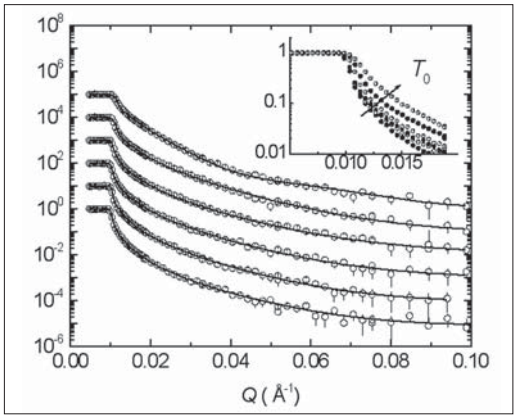

Fig. 3: Reflectivity measured along the path indicated by crosses in Fig. 2; from bottom to top, $t_0 = |T\text{-}T_0|/T_0 = 7.38 \times 10^{-2}$, 4.70×10^{-2}, 2.32×10^{-2}, 1.32×10^{-2}, 5.81×10^{-3}, and 1.91×10^{-3}. The solid lines are fits corresponding to the volume fraction composition profiles of Fig. 4a. The inset shows how the critical edge advances as the coexistence limit $T_0 = 0.98\ T/T_c$ for ϕ (hexane) = 0.25 is approached. For that composition, $T_c = 14.39 \pm 0.05$ °C, and T_0 is 8.93 ± 0.05 °C.

of a wetting layer close to the interface followed by a long decay to the bulk composition. These features occur on length scales greater than the nominal minimum resolution ($2\pi/Q_{max}$) of 60 Å.

The surface excess, i.e. the enrichment of hexane at the interface, was computed from the profiles shown in Fig. 4 as $\Gamma = \int_{z=0}^{\infty}(\phi - \phi_B)c_H dz$, where ϕ_B is the bulk volume fraction and c_H is the concentration of pure hexane. Γ obeys the predicted power law $\Gamma = \Gamma_0 t_0^m$ as a function of distance from coexistence with $t_0 = |T\text{-}T_0|/T_0$.

At small t_0 for $T < T_c$, the exponent m is close to –1/3, a value consistent with van der Waals complete wetting. For larger t_0, $m >> -1/3$, indicating a

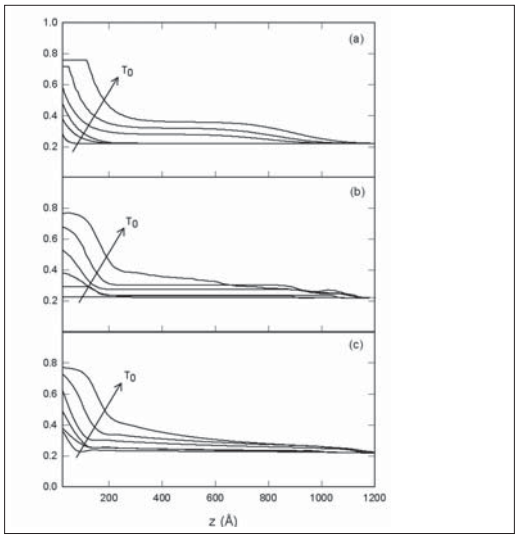

Fig. 4: Volume fraction composition profiles corresponding to the multilayer fit in Fig. 3 (a), from the unbiased fit (b), and from the analytical fit (c). The arrows show the evolution as the coexistence point is approached.

crossover in wetting behavior. We note, however, that these conclusions should be considered with caution as the Lifshitz theory of van der Waals forces cannot be strictly applied to a system in which the density profile decays so gradually into the bulk. In such a case it is not possible to define a sharp interface between the bulk solution and the adsorbed region. Moreover, it is not clear up to what extent the wall and the bulk fluid at large z compete in determining the strength of the z^{-3} potential.

[1] Bonn, D.; Ross, D. Rep. Prog. Phys. **64**, (2001).
[2] Law, B. D. Prog. Surf. Sci. **66**, (2001).
[3] Fisher, M. E.; De Gennes, P. G. C. R. Acad. Sci. (Paris) Ser. B **287**, 207,(1978); Rowlinson, J. S.; Widom, B. Molecular Theory of Capillarity; Dover: Mineola, NY, 2002.
[4] Zhao, H; Penninckx-Sans, A.; Lee, L.-T.; Beysens, D.; Jannink, G. Phys. Rev. Lett. **75**, (1995).
[5] Fenistein, D.; Bonn, D.; Rafaï, S.; Wegdam, G. H.; Meunier, J.; Parry, A. O.; Telo da Gama, M.; Phys. Rev. Lett. **89**, 096101, (2002)
[6] Bowers, J.; Zarbakhsh, A.; Christenson, H. K.; McLure, I. A.; Webster, J. R. P.; Steitz, R. Phys. Rev. E **72**, 041606 (2005).
[7] Bowers, J.; Zarbakhsh, A.; McLure, I. A.; Webster, J. R. P.; Steitz, R.; Christenson, H. K. J. Phys. Chem. C **111**, 5568 (2007).

Corresponding author:
R. Steitz
steitz@hmi.de

Higher and Higher: Momentum-Resolved High-Resolution Spectroscopy of Elementary Excitations using the Neutron Resonance Spin-Echo Method

K. Habicht[1], T. Keller[2, 3], S.P. Bayrakci[2], P. Aynajian[2], L. Boeri[2], S.K. Bose[2], B. Keimer[2] und F. Mezei[1]

■ 1 HMI, SF1 ■ 2 Max-Planck-Institut für Festkörperforschung, Stuttgart ■ 3 ZWE FRM II, TU München

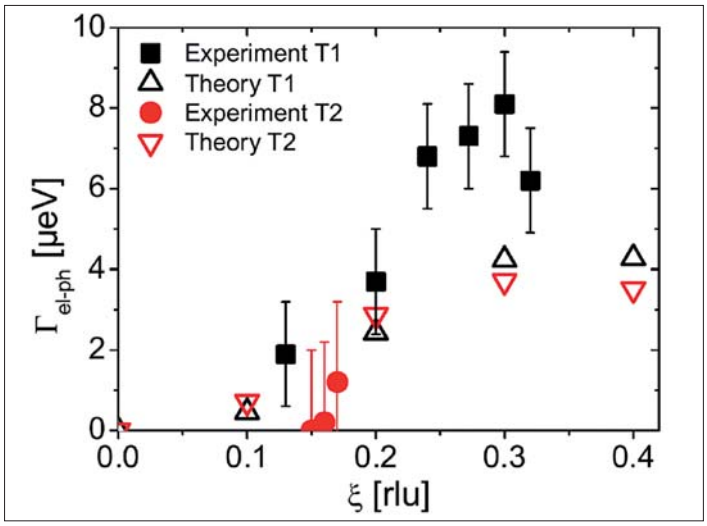

Fig. 1: Contribution of the electron-phonon interaction to the linewidth of transverse acoustic [ξξ0] phonons in Pb with different polarization vectors T1 and T2: experimental data compared to ab-initio theoretical predictions.

From a microscopic point of view, transport phenomena in solid state physics, such as thermal or electrical conductivity, are governed by the interaction between quasiparticles or their interaction with other real particles. Heat in a material can be transported by the propagation of quantized lattice vibrations, i.e. phonons. This phonon propagation, and thus the lifetime of the quasiparticles, is limited by the interaction with other thermally excited phonons as is the case in anharmonic crystals. Electrical conductivity is limited by scattering processes of electrons with phonons playing a crucial role in superconductivity of elemental metals. Likewise in a magnetic material collective spin excitations (magnons) may interact with each other. All these diverse types of interactions (phonon-phonon, electron-phonon, and magnon-magnon) can be studied by measuring the quasiparticle lifetime which is inversely proportional to their linewidth in energy. While the energy of the elementary excitations as a function of wavevector (dispersion relation) is easily accessible with well established neutron scattering techniques such as triple-axis spectroscopy (TAS), higher energy resolution is mandatory for the study of their energy widths or lifetimes.

Increasing the resolution is usually at the cost of intensity of the probing neutron beam. The Neutron Spin Echo method allows overcoming this restriction in that it decouples the energy resolution from the intensity by using polarized neutrons. High energy resolution is here achieved by measuring the spread in Larmor precession angles of neutrons travelling in well defined magnetic field regions before and after the sample. The Neutron Resonance Spin-Echo technique (NRSE) is a sophisticated technical variant ideally suited to investigate dispersive excitations since *spin-echo focussing* onto the phonon branches is easily realized by tilting of compact resonance frequency spin-flippers. Combining NRSE and TAS instrumentation offers the highest resolution available for lifetime studies of dispersive excitations.

The first realization of the NRSE-TAS technique has been implemented at the cold neutron triple axis instrument V2/FLEX at HMI. Initial experiments focused on the temperature dependence of phonons along the main crystallographic directions in single crystal Pb [1]. Broadening of the one-phonon peaks due to lattice anharmonicity (phonon-phonon interaction) resulting in Lorentzian linewidths could be measured with high accuracy. A thorough understanding of resolution effects in NRSE-TAS type experiments is a necessary prerequisite to separate intrinsic lifetimes from resolution effects. This is provided by a general analytical approach developed at HMI, which identified systematic instrumental effects, sample mosaicity and curvature of the

dispersion surface to enter into the resolution function and allows one to correct experimental raw data. Since NSE is sensitive to the intermediate scattering function directly such correction requires no deconvolution as has been proven for the case of dispersive excitations [2].

The difference in linewidths for a phonon mode above and below the superconducting transition temperature T_C is a direct measure of the electron-phonon contribution to the linewidth. Due to Cooper-pair formation the phonon decay channel via e-p interaction is forbidden below T_C. The experiments performed at V2/FLEX could already establish a 6 μeV upper limit for the change in linewidth due to electron-phonon interaction for a particular mode, the transverse acoustic [0.1 0.1 0] phonon. In collaboration with the MPI Stuttgart pioneering experiments could be performed with the new NRSE based instrument TRISP at FRM II. This instrument benefits from a substantial increase in neutron flux and offers access to thermal neutron wavelengths. The electron-phonon interaction in the BCS superconductor Pb could be studied in a wide momentum range [3]. For the first time a detailed comparison between theoretical *ab-initio* model calculations and momentum-resolved experimental data became possible (Fig. 1). This comparison shows that the q-dependence of the electron-phonon contribution to the linewidth is in general satisfactorily described by theory. Quantitatively however, the theory yields smaller values than experimentally observed.

The NRSE method is also very well suited to investigate spin waves in antiferromagnets. Recently it has been applied in measurements of the prototype antiferromagnet MnF_2 [4]. Due to access to thermal neutron wavelengths earlier experiments performed at V2/FLEX (restricted to a wavevector range less than 0.2 reciprocal lattice units) could be extended to investigate magnon lifetimes over the whole Brillouin zone. Both wavevector and temperature dependence were extensively investigated. As a surprising result, the experimental data (Fig. 2) is best described by a theoretical model which is based on scattering processes of magnons with longitudinal spin fluctuations and not by magnon-magnon interaction.

These experiments demonstrate that the spin echo method allows a completely new experimental access to the understanding of important microscopic phenomena such as superconductivity or dynamics in magnetism and mark the beginning of a new chapter in neutron scattering research.

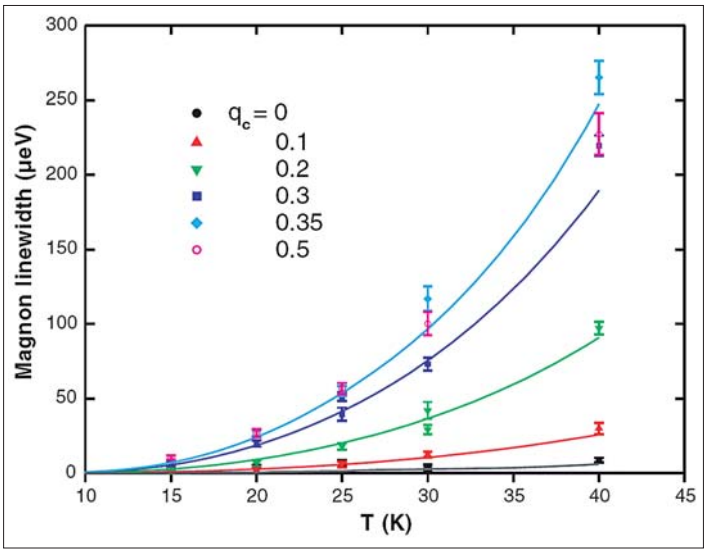

Fig. 2: Temperature dependence of magnon linewidths in MnF_2 for various wavevectors q_c along the crystallographic c-direction. The curves represent theoretical model calculations.

[1] K. Habicht, R. Golub, F. Mezei, B. Keimer, and T. Keller, Phys. Rev. B **69**, 104301 (2004).
[2] K. Habicht, T. Keller, and R. Golub, J. Appl. Crystallogr. **36**, 1307 (2003).
[3] T. Keller, P. Aynajian, K. Habicht, L. Boeri, S.K. Bose, B. Keimer, PRL **96**, 225501 (2006)
[4] S.P. Bayrakci, T. Keller, K. Habicht, B. Keimer, Science **312**, 1926 (2006)

Corresponding author:
K. Habicht
habicht@hmi.de

Sodium ordering and the control of properties in sodium cobaltate

D. J. P. Morris[1], M. Roger[2], D. A. Tennant[1,4], M. J. Gutmann[5], J. P. Goff[3], J.-U. Hoffmann[1], R. Feyerherm[1], E. Dudzik[1], D. Prabhakaran[6], A. T. Boothroyd[6], N. Shannon[7], B. Lake[4,8] & P. P. Deen[9]

■ 1 HMI, SF2 ■ 2 CEA Saclay, France ■ 3 Royal Holloway, University of London, UK ■ 4 Institut für Festkörperphysik, Technische Universität Berlin, Germany ■ 5 ISIS, Didcot, UK ■ 6 Clarendon Laboratory, Oxford, UK ■ 7 University of Bristol, UK ■ 8 HMI, SFN1 ■ 9 ILL, Grenoble, France

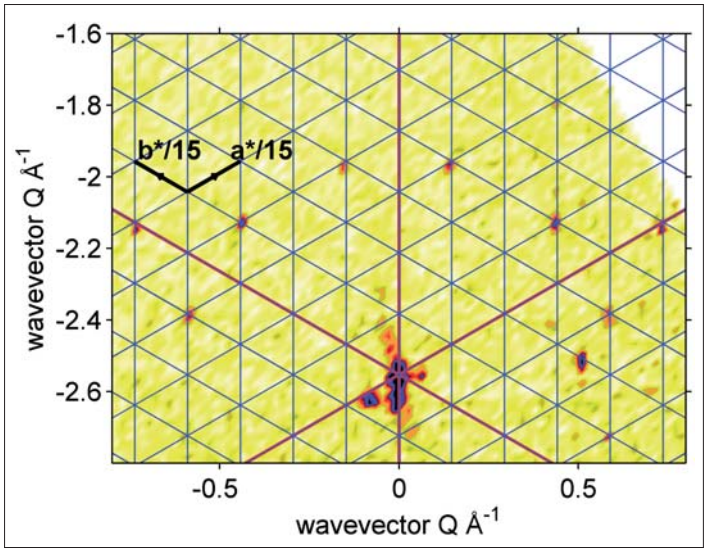

Fig. 1: Superstructure peaks observed for $Na_{0.75}CoO_2$ on E2 at HMI at 1.5K in the (hk0) plane. The high **Q**-resolution allowed the commensurability of this structure to be observed by placing a commensurate grid (**a***/15 × **b***/15) over the data.

Sodium cobaltate, Na_xCoO_2, has attracted much interest in the past decade due to the possibilities of thermoelectric applications [1] and interplay between magnetism and superconductivity leading to comparisons with the superconducting cuprates [2].

The structure is made up of triangular layers of CoO_2 separated by a sodium layer of variable concentration. Due to this structure it was expected to show two-dimensional magnetism. Whereas magnetic inelastic neutron scattering measurements showed that the in-plane magnetic coupling is comparable to that out-of-plane [3], implying different underlying physics to that seen in the cuprates.

In 2003 superconductivity was discovered in the hydrated material, $Na_{0.35}CoO_2{\cdot}1.3H_2O$ [2]. Early understanding was that the water molecules created a spacer layer screening the cobalt from the pair breaking potential due to the Na^+ ordering. This was backed up by the discovery that the monohydrate system (H_2O intercalated into the Na layer rather than between Na and CoO_2 layers) fails to superconduct. Recent work, however, has shown that the water also plays a chemical role in the superconducting samples with the intercalation of oxonium ions, H_3O^+, into the Na layer.

Recent studies have shown one way of obtaining the properties of a good thermoelectric material is via phonon-glass-electron-crystals (PGEC). Such materials form electrically conductive cages around a free atom which can 'rattle' scattering thermal phonons. One explanation for Na_xCoO_2 being a good thermoelectric is that it is a PGEC but lacks the usual 'rattler' cages [4]. Other possible explanations for the thermopower have also developed and gained popularity for example involving spin entropy.

The role of sodium ordering on the physical properties and the principles behind the ordering was also not well understood, although was widely recognised as playing an important role in the broader physics. This had previously been studied using electron diffraction, powder neutron diffraction and single crystal hard x-ray diffraction but the ordering principles had not been deduced. Our approach was to take high quality single crystals and observe the spatial sodium ordering using complementary diffraction techniques; neutron Laue diffraction on the SXD instrument at ISIS and E2 at HMI and hard x-ray diffraction on MAGS at BESSY [5].

With SXD, a large three-dimensional volume of reciprocal space is measured giving more information about the superstructure than the previous techniques used since a large number diffracted peaks (main Bragg peaks and superstructure peaks) are obtained. In a sample of concentration x=0.92 a 12-spot ring surrounding the main Bragg peak positions at base temperature and superstructure peaks at 0.2 r.l.u. (reciprocal lat-

tice units) at room temperature were measured. The 12-spot ring was also measured in a sample of concentration $x=0.75$ at base temperature and also at 150 K. Then using E2 it was possible to zoom into a plane of reciprocal space giving higher resolution in wave-vector transfer (**Q**). With this information we were able to determine that this ordering is commensurate (see Fig.1). Also following the peak heights with varying temperature told us that we were dealing with a first order transition at approximately 285 K. Using single crystal hard x-ray measurements on MAGS allowed precise temperature dependence measurements to be made. This showed a substantial hysteresis in the superstructure peak intensities across the transition.

By application of electrostatics, involving short-range and long-range potentials on the sodium cobaltate structure, the ordering principles were studied. The sodium ions have two possible sites; Na^1 on top and below a neighbouring cobalt ion, and Na^2 which is a lower energy site away from nearest neighbour cobalt ions. It was found that vacancies in the sodium layer become attractive at very short distances since the promotion of a sodium ion onto Na^1 sites become energetically favourable. The long-range Coulomb interactions then allow these clusters to condense out onto a long range order. One ground state structure that condenses out of this model is a square trivacancy structure with concentration $x=0.80$. By further calculating the potential gradient on the cobalt ions due to the Na ordering it was possible to see that the CoO_2 layer is buckled by the underlying sodium cluster (see Fig.2). Our low temperature data proved extremely sensitive to this buckling, with the Fourier transform of the trivacancy structure requiring the cobalt ions to be buckled by less than $0.01c$ in order to give good agreement with diffraction data (c being the c lattice parameter, ~10.82Å) [5].

Calculating the Coulomb landscape on the cobalt layer it is then possible to see how the partial cobalt valences, reported in NMR measurements, are realised. Also the resulting potential wells are large compared to hopping frequencies, therefore spins can become localised. This occurs with the same periodicity as the sodium ordering and can readily explain the dimensionality of the magnetism since in plane well separation is approximately equal to the c-lattice parameter. The buckling of the CoO_2 layer forms cages around the Na_1 ions (red spheres in fig. 2) giving rise to the rattler sites missing from previous reports of PGEC thermoelectric behaviour in this material as well as conduction pathways within the Coulomb landscape.

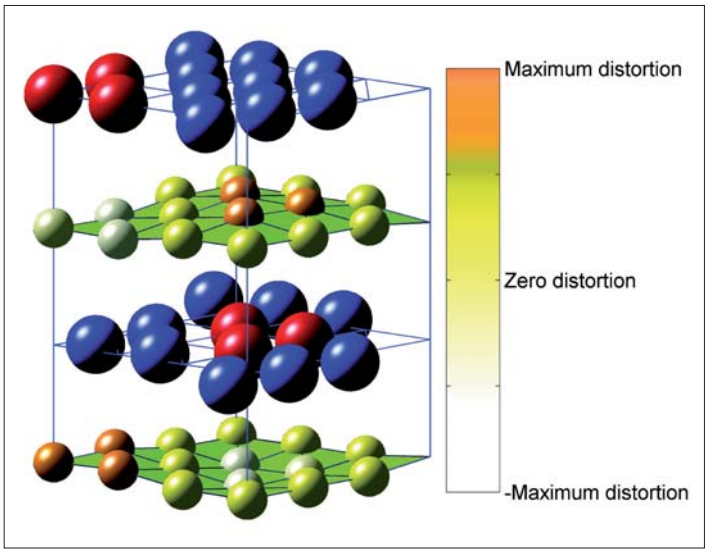

Fig. 2: Unit cell for $x=0.80$ trivacancy superstructure used to model the low temperature phase for $Na_{0.75}CoO_2$ and $Na_{0.92}CoO_2$. The colour scale shows the buckling of the CoO_2 layer (oxygens are ommited for clarity) that form cages allowing Na to rattle.

To summerise, the sodium ordering has been understood with complementary techniques of neutron and x-ray diffraction with application of electrostatics. This then sheds new light on the magnetism, thermopower, and importance of ionic ordering in this type of system.

[1] I. Terasaki, et al. Phys. Rev. B. **56**, R12685–R12687 (1997)
[2] K. Takada, et al. Nature. **422**, 53–55 (2003)
[3] S. P. Bayrakci, et al. Phys. Rev. Lett. **94**, 157205 (2005)
[4] K. Takahata et al. Phys. Rev. B. **61**, 12551–12555 (2000)
[5] M. Roger, et al. Nature. **445**, 631-634 (2007)

Corresponding author:
D. J. P. Morris
jonathan.morris@hmi.de

Spin-state polaron as a precursor to ferromagnetism and metallicity in hole-doped $LaCoO_3$

A.Podlesnyak[1], M.Russina[2], K.Conder[3], E.Pomjakushina[3], P.Allenspach[3] and D.I.Khomskii[4]

■ 1 HMI SF2 ■ 2 HMI SF1 ■ 3 Laboratory for Developments and Methods, Paul Scherrer Institut, Villigen PSI, Switzerland. ■ 4 II Physikalisches Institut, Universität zu Köln, Köln, Germany.

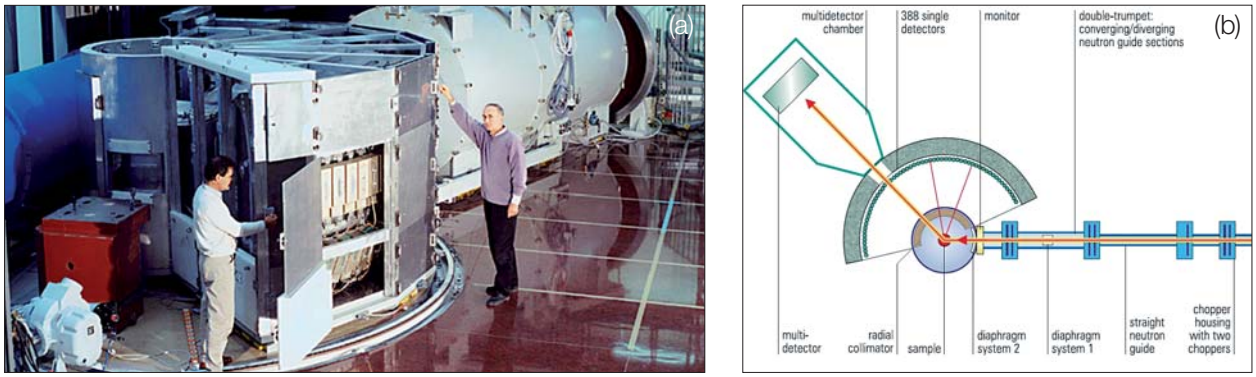

Fig. 1: a) The high-resolution time-of-flight spectrometer V3/NEAT b) Schematics of a direct time-of-flight spectrometer. The choppers define the energy and the pulse width of the incident neutrons. The monochromatic neutron pulses are then scattered from the sample and are detected by arrays of neutron counters covering a large solid angle. The energy transfer $\hbar\omega$ and the modulus of the scattering vector **Q** are then determined by the flight time of the neutrons from the sample to the detector and by the scattering angle Θ at which the detector is positioned, respectively.

Nanostructured magnetic materials form a novel type of systems where fundamental properties can be tuned to desired requirements on the molecular level. It makes these materials of particular interest for applications in such fields as molecular electronics or quantum computing. Doped perovskites $La_{1-x}Sr_xCoO_3$, compounds where magnetic nanoclusters of 20-30Å coexist in a nonmagnetic matrix [1], can serve as a naturally occurring analogue to artificially fabricated heterostructures. Already a slight variation of the doping degree strongly influences the interactions in- and between the clusters leading to dramatical changes of the macroscopic properties, such as value and temperature dependence of magnetization.

Most of the investigations up to now have been focused on the relatively high composition range above x=0.1, where it is believed that embedded spins already form short-range-ordered ferromagnetic clusters. However, one intriguing point was discovered in 1996 and apparently forgotten later. Namely, already lightly doped materials, with an estimated concentration of x~0.002 (i.e. two holes per thousand Co^{3+} ions) exhibit paramagnetic properties at low temperatures, in strong contrast to the diamagnetic $LaCoO_3$ [2]. The few embedded spins in a nonmagnetic background would give order of magnitude smaller magnetic susceptibility than it was observed. With this controversy in mind, we undertook an inelastic neutron scattering (INS) study with the goal to identify the energy spectrum and magnetic state of the excited state of cobalt ions in lightly doped $La_{0.998}Sr_{0.002}CoO_3$. The measurements with and without application of magnetic field have been performed on the cold neutron time-of-flight spectrometer NEAT at HMI (Fig. 1). In the view of the low signal the successful optimization of NEAT for these types of studies including the development of the new data collection approach was of crucial importance. The details of the experiments are described in original publications [3-5]. In this report we briefly discuss the obtained result.

Undoped $LaCoO_3$ with perovskite structure contains Co^{3+} ions with six electrons in $3d$ orbitals, octahedrally surrounded by six O^{2-} ions. Two of the $3d$ orbitals ($3d_{x^2-y^2}$ and $3d_{z^2}$, which are called e_g) point directly toward the O^{2-} ions. The other three orbitals ($3d_{xy}$, $3d_{xz}$, and $3d_{yz}$, which are called t_{2g}) lie between the O^{2-} ions. In the crystal field of the six O^{2-} ions the degeneracy of the five $3d$ orbitals is lifted. The latter three of these orbitals are now lower in energy than the former two. The intra-atomic ex-

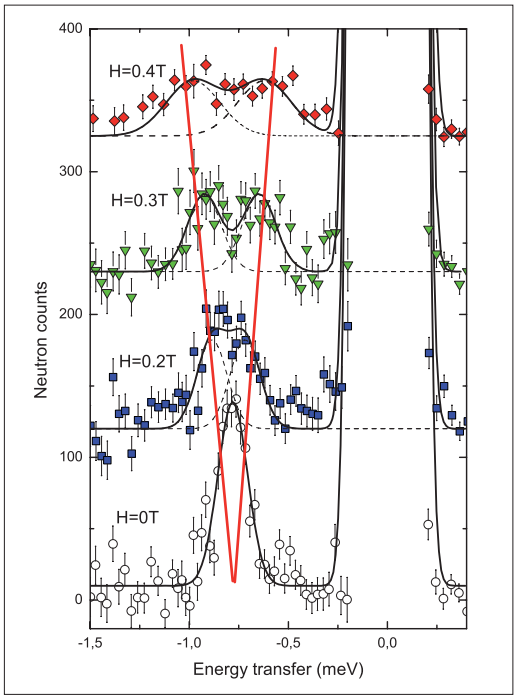

Fig. 2: Evolution of the INS in the external magnetic field at T=2 K.

change interaction and the octahedral crystal-field interaction determine the three possible choices of the orbital occupations by electrons. One of these configurations of Co^{3+} (with 6 d-electrons) has the maximum spin S=2 and is called high-spin (HS). The others configurations are called low-spin (LS) and intermediate-spin (IS) because they contain zero and two unpaired electrons, respectively. When holes are put into these orbitals by replacing the trivalent La^{3+} ions with divalent Sr^{2+} ions, the compound becomes a mixed valence system with both Co^{3+} and Co^{4+}. The description of the magnetic states requires an assignment of the spin state to both Co^{3+} and Co^{4+} ions. The number of possible configurations of the system gives rise to discrete energy levels E_i which can be determined by inelastic neutron scattering. The idea of INS experiment is rather simple. The excited level at energy ΔE results in an inelastic peak in the spectrum of scattered neutrons at an energy transfer $\pm\Delta E$. The position of the peak is determined by the energy gap between two configurations.

In contrast to the parent compound $LaCoO_3$, where no excitations have been found for temperatures T<30K [4], in the doped system with the Sr concentration of only 0.2% an inelastic peak at the energy transfer ΔE~0.75 meV was observed already at T=1.5K. Surprisingly, the intensity of the ΔE excitation is much higher than it was expected from an estimated concentration of doped holes per Co site. With the application of a magnetic field

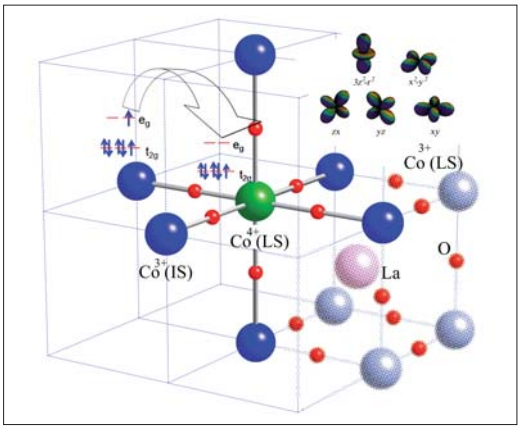

Fig. 3: Schematic view of a possible state of spin-state polaron. The scheme showing the process of electron (hole) hopping on the background of the Co^{3+}(IS) and Co^{4+}(LS) ions. Five 3d orbitals are shown in the right upper corner.

we observed strong Zeeman splitting of the inelastic peak indicating an *unusually high magnetic moment* $gS\sim15_{\Delta B}$ (see Fig. 2). The value of the magnetic moment cannot be described by single Co^{4+} ion in any spin state. In contrast, contribution of several Co-ions, i.e. the formation of the magnetic clusters is required to explain the experimental data. Neighboring LS-Co^{4+} ion and IS-Co^{3+} ion can share an e_g electron by swapping configuration, as shown in Fig. 3. The t_{2g} electrons, in their turn, couple ferromagnetically via double exchange interaction. Therefore, we propose that the *holes introduced in the LS state of* $LaCoO_3$ *are extended over the neighboring* Co *sites forming spin-state polarons and transforming all the involved* Co^{3+} *ions to the IS or HS state (Fig. 3)*. Spin-state polarons behave like a few nanometer size magnetic nanoparticles embedded in an insulating nonmagnetic matrix. The addition of charge carriers leads to grows of such spin-state polarons and finally results in a metallic state with long-range FM order for $x>0.18$ [1]. Our results show remarkable importance of intrinsic inhomogeneities for the governance of macroscopic properties and functionality of doped cobaltites. The tuning of the characteristics of spin-based inhomogeneities in the desired way opens bright perspectives for novel technological applications of these materials.

[1] J. Wu, et al., Phys. Rev. Lett. **94**, 037201 (2005).
[2] S. Yamaguchi, et al., Phys. Rev. B **53**, R2926 (1996).
[3] A. Podlesnyak, et al., JMMM **310**, 1552 (2007).
[4] A. Podlesnyak, et al., Phys. Rev. Lett. **97**, 247208 (2006).
[5] A. Podlesnyak, et al., to be published.

Corresponding author:
A. Podlesnyak
andrei.podlesnyak@hmi.de

Correlation between Icosahedral Short Range Order, Glass Forming Ability and Crystallization of Zr-Ti-Mi-Cu-(Be) Glasses

N.Wanderka, S. Mechler
■ HMI, SF3

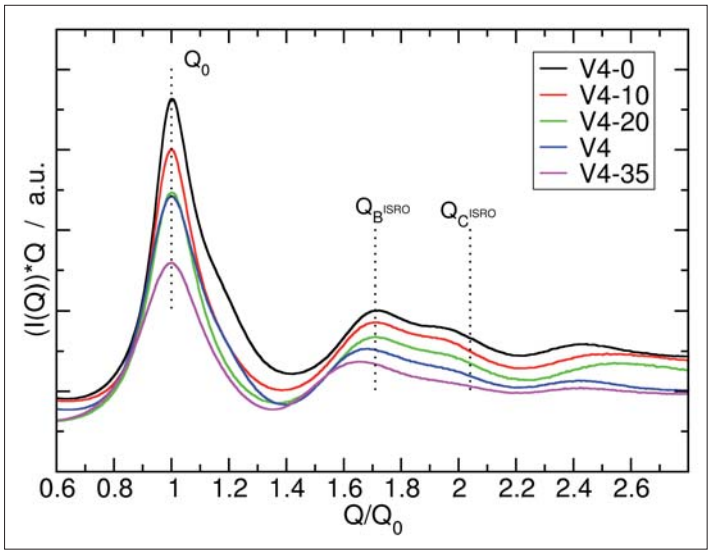

Fig. 1: Interference function $I(Q)*Q$ of various Zr-Ti-Ni-Cu glasses with different Be content (in at.%) amorphous glasses. Be free glass is also shown. The values Q_B and Q_C ^{ISRO} mark the positions of diffuse maxima which according to [3] are indicative for icosahedral short range order of the amorphous phase.

Zr-based metallic glasses can be produced by cooling liquid melts with cooling rates comparable to those of oxide glasses. They are of great technical and physical interest because of their extraordinary properties like high strength, elasticity and low viscosity. However, for their potential application, knowledge about the correlation between structure and thermal stability against crystallisation is necessary. An important parameter for such alloys is the structural icosahedral short-range order (ISRO). ISRO of the glassy phase hinders the formation of intermetallic crystalline phases but leads to formation of quasicrystals. The stable $Zr_{41.5}$–$Ti_{41.5}$-Ni_{17} quasicrystal has ideal ISRO [1]. If the composition of this alloy is altered, e.g. by addition of misfit atoms like Be, the deterioration of the ISRO structure hinders the formation of quasicrystals and therefore the glassy phase is preferred.

To get more insight into the role of ISRO on the thermal stability of glasses we investigated the effect of Be addition to Zr-Ti-Ni-Cu model alloys by X-ray diffraction (XRD) combined with transmission electron microscopy (TEM). The structure of such glasses with different Be content is indicated by the interference functions $I(Q)$ in Fig.1, which were derived from corresponding TEM-selected area electron diffraction images. The existence of the third maximum Q_C^{ISRO} is indicative for ISRO. Be free glass has a significant third maximum Q_C^{ISRO} which indicates high degree of ISRO. Be containing glasses show a decrease of the intensity of the third maximum. With an increase of Be content, the degree of ISRO decreases and for the alloy with Be contents > 25 at%, the third maximum is practically vanished.

We found that the Be free glass easily transforms polymorphously into a quasicrystalline phase during thermal treatment because their ISRO facilitates the nucleation of quasicrystals. The TEM micrograph in Fig. 2 shows the microstructure of the completely crystallised Be free glass The diffraction pattern (inset in Fig. 2) taken from one of the grains shows the tenfold symmetry of an icosahedral quasicrystalline phase. In contrast Be rich glasses are very stable against crystallization and crystallise preferably into intemetallic phases, because the misfit of Be atoms deteriorates the ISRO of the glass and thus impedes the formation of quasicrystals.

Our results fit to the model of geometric frustration, which describes metallic glasses as “highly defective” quasicrystals [2], i.e. as quasicrystals for which the ISRO structure is degraded by misfit atoms. This model can be used as a rule for the design of metallic glasses based on the stable $Zr_{41.5}$–$Ti_{41.5}$-Ni_{17} quasicrystal. Fig. 3 shows a flowchart starting from the composition of this quasicrystal which is altered by the addition of Be, Cu and Al or by change of the element ratios of the composition. Alloys indicated by red colour in Fig. 3 form preferably quasicrystals while alloys indi-

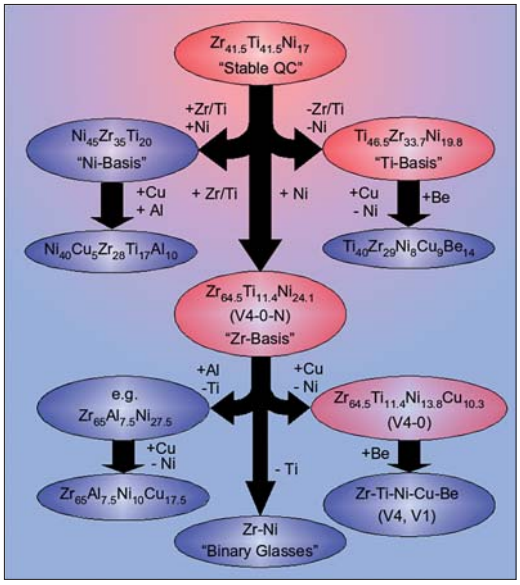

Fig. 3: Flow-chart for the structural alteration of quasicrystals towards metallic glasses as a hint for the design of metallic glasses. Starting from the composition of the stable $Zr_{41.5}$–$Ti_{41.5}$-Ni_{17} quasicrystal the structure is altered by the addition of Be, Cu and Al or by change of the element ratios of the composition, that disturb the ISRO. Alloys indicated by red colour form preferably quasicrystals while alloys indicated by blue colour are good glass formers.

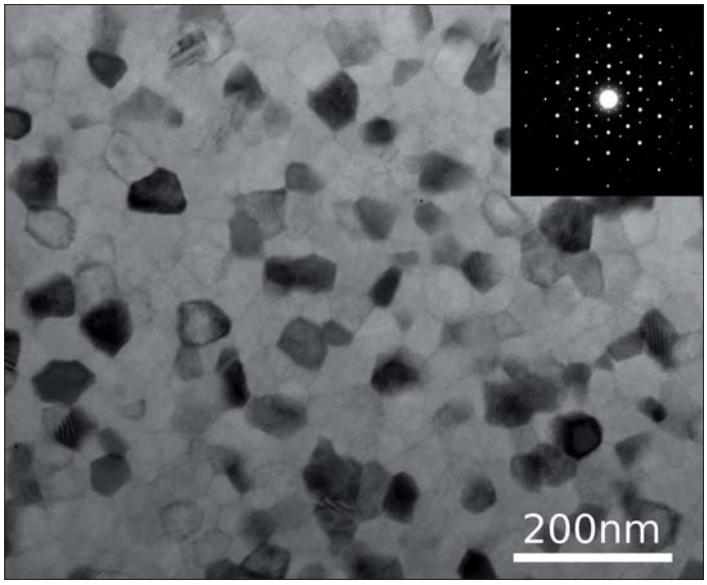

Fig. 2: Bright field TEM image of the microstructure of the Be free Zr-Ti-Ni-Cu-glass after heat treatment with the corresponding SAED image of one icosahedral quasicrystal in the inset.

cated by blue colour are good glass formers. The flow scheme reveals, that the more the structure of the ideal, stable quasicrystal is disturbed, the less stable they are until the glass becomes the preferable structure of the alloy.

More detailed investigations of metallic bulk glasses including the stability against thermal treatments can be found in the thesis of S. Mechler, TU Berlin, January 2007 [4].

[1] K.Kelton, Intermetallics **14** (2006) 996
[2] M.V. Jaric, Introduction to quasicrystals, Vol. 1 (Academic Press Inc., San Diego, 1988)
[3] S.Sachdev and D. Nelson, Phys. Rev. B **32** (1985) 1480
[4] S. Mechler, Ph.-D. Thesis, TU Berlin, January 2007

Corresponding author:
N. Wanderka
wanderka@hmi.de

Energy-selective neutron radiography

N. Kardjilov[1], A.Hilger[1], I. Manke[1,2], M. Strobl[3], W. Treimer[3], J. Banhart[1,2]
■ 1 HMI, SF3 ■ 2 Technische Universität Berlin ■ 2 University of Applied Sciences (TFH) Berlin

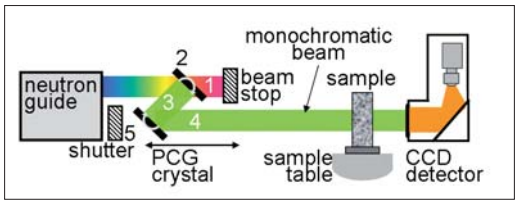

Fig. 1: Schematic sketch of CONRAD including the double monochromator device: (1) upper guide and neutron beam (2) first PG(002) monochromator, (3) diffracted monochromatic neutron beam, (4) second PG(002) monochromator, (5) lower guide and shutter of lower part of the neutron beam

Neutron imaging and especially neutron tomography gained a lot of importance in neutron instrumentation for scientific and industrial applications within the last decade. Monochromatic neutrons, however, have not been in the focus of mainstream developments due to the high intensity losses and correspondingly longer measuring times. In spite of that the neutron radiography and tomography with a monochromatic beam shows promising results in comparison to the standard technique where a white beam is used.

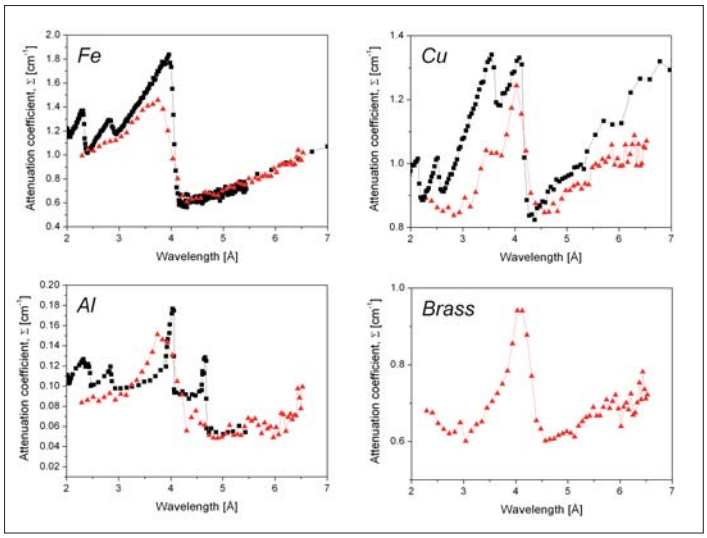

Fig. 2(a) – (d): Tabulated (dark) and radiographically (light) measured attenuation coefficients of Al, Fe, Brass and Copper. The measured values are smeared due to the rather large mosaic spread of the C- crystals.

In the case of polychromatic neutron tomography severe problems for quantification of components of a sample in neutron imaging arise from scattering effects and beam hardening – an effect caused by the fact that the attenuation coefficients are different for different energies present in the beam. The use of monochromatic radiation avoids beam hardening, and the use of wavelengths beyond the Bragg edges of a material avoids Bragg scattering if $\lambda > 2d_{max}$, where d_{max} is the biggest crystal lattice spacing of the sample material (see Table 1). For crystalline solids, these effects and strong incoherent scattering from hydrogenous materials give rise to unwanted background scattering. Monochromatic cold neutrons allow for a much better quantification and are much more sensitive to inhomogeneities in samples. Therefore, a double monochromator option was designed and set up at the neutron radiography instrument CONRAD at HMI [1].

The first measurement position of CONRAD immediately behind the neutron guide was used to install a double monochromator device as shown in Fig.1. Both crystals of the device can be rotated to chosen Bragg angles; the second one can additionally be positioned along the original beam direction in order to reflect the monochromatic beam coming from the first crystal into the initial beam path of the CONRAD instrument. This construction enables one to choose a monochromatic beam with a defined wavelength band ($0.1 < \Delta\lambda/\lambda < 0.01$) between 2.0 Å and 6.5 Å. This wavelength range (depending on the Bragg angle) includes the Bragg edges of many important engineering materials like e.g. Al, Brass (CuZn), Cu and Fe.

Material (hkl)	Al (111)	C (001)	Cu (111)	Fe (110)	β-CuZn (110)
Cut-off, d_{max} [Å]	4.68	6.71	4.17	4.08	4.20

Table 1: Bragg cut-offs of important engineering materials

Quantitative measurements were performed on test samples of Al, Fe, Brass and Copper and the data compared with tabulated values. Figs.2a–2d show the results (for brass tabulated values could not be found). The worse resolution

is due to the broad mosaic spread of the graphite crystals, however, a smaller mosaic spread would decrease the reflected intensity and increase the exposure time for radiography and tomography.

The advantage of such a continuously adjustable wavelength is apparent. Different parts of an object under investigation having very similar attenuation coefficients can be made transparent at a certain wavelength (cp. the attenuation of copper at $\lambda = 3.4$ Å and $\lambda = 4.2$ Å, and for steel at $\lambda = 4.2$ Å and $\lambda = 4.6$ Å) or enhanced using another wavelength, where the particular attenuation differs much more, see Fig. 3. Moreover, the method gives the possibility to distinguish between alloys like Cu and ZnCu (Brass). Additionally, the attenuation of PE is nearly constant within narrow wavelength band. So it is possible to eliminate scattering from H-containing parts in a radiography (and tomography) using proper wavelength for other materials that show high contrast in the pictures, see Fig. 3 (right).

Material stress and strain regions in samples usually require point-like scans of neutron diffraction to determine the proper region of interest (ROI). Using the tuneable option of CONRAD these ROI can now investigated in a much more efficient manner. Based on the Bragg edges (of different crystals) the attenuation spectra of these regions show enhanced contrast behaviour in the neighbourhood of proper wavelengths but not only in one point but all over the sample simultaneously. Recording radiographs at different (equidistant) wavelengths, one gets of each point of the sample the full information of attenuation. As a Bragg edge originates in the diffraction from a specific crystal lattice spacing of a material, lattice changes due to material stress can be imaged with this

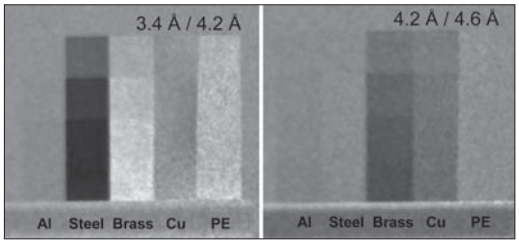

Fig. 3: Quotient images at wavelengths where the attenuation coefficients for Cu (left) and Fe (right) stay without change.

new method by mapping the shape, position and amplitude of a Bragg edge. In order to test this method a deformed steel plate of 5 mm thickness has been measured radiographically from 2.2 Å until 6.4 Å. in steps of 0.1 Å. The attenuation

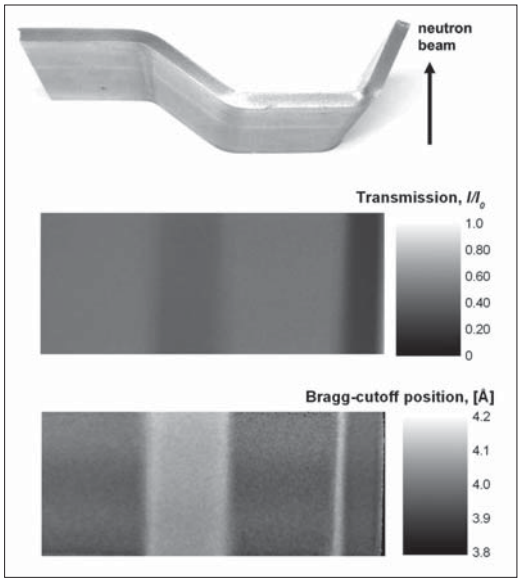

Fig. 4: Steel plate (50×10 mm^2) of 5 mm thickness was deformed – photo on the top. The radiography image is shown in the middle. 2D mapped position of the Bragg edge for each pixel in the deformed plate is shown in the bottom image. The obtained map can be related to the residual stress distribution in the plate.

spectrum (see Fig. 1b) for each point of the sample was derived and the resulted curve was fitted by a Gauss function. From the fit parameters the position of the Bragg edge was determined and a grey value was related to the obtained value. The results of the data evaluation are shown in Fig. 4. These promising results can be improved by decreasing the mosaic spread of the C–crystals and increase of energy resolution and hence the resolution of the Bragg edge scans. This would enable a fast spatial resolved stress mapping of big sample areas eventually to determine specific areas for more accurate diffraction investigations in dedicated stress and strain diffractometer.

[1] W. Treimer et al., Appl. Phys. Lett. **89**, 203504 (2006).

Corresponding author:
N. Kardjilov
kardjilov@hmi.de

Ion induced intermixing in thin metal tri-layers – a study with sub-nanometre depth resolution

N. Darowski[1], I. Zizak[1,2], A. Gupta[3], C. Meneghini[4], A. Erko[2]

■ 1 HMI, SF4 / SF2 ■ 2 BESSY, Berlin, Germany ■ 3 UGC-DAE Consortium for Scientific Research, Indore, India ■ 4 University of Rome, Rome, Italy

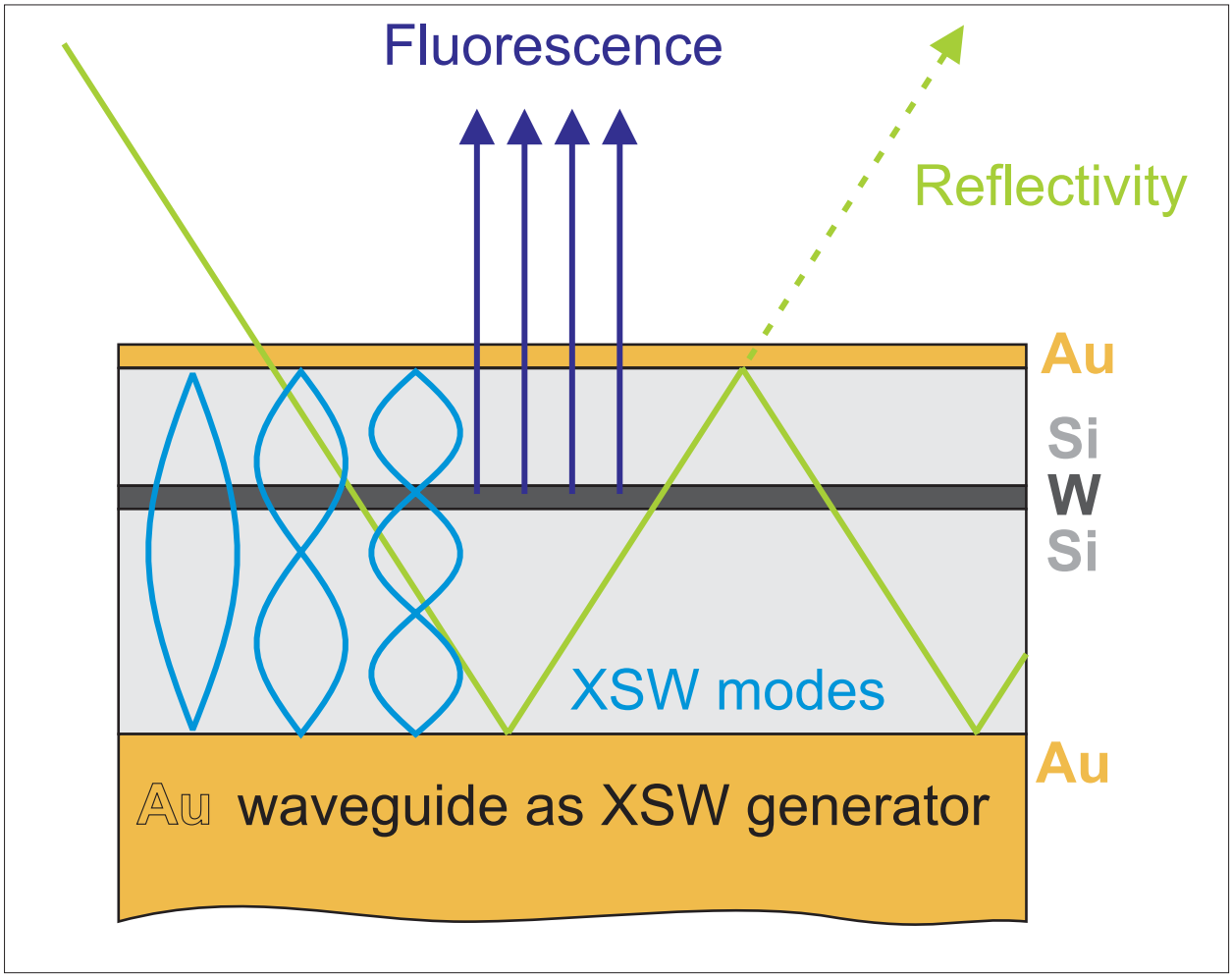

Fig. 1: Experiment geometry (See text for details)

Thin films and multilayers have emerged as important classes of nanostructured materials with immense possibilities of tailoring their properties in order to achieve the desired functionality. In multilay er structures, a particular property can get modified drastically as the thickness of the individual layers becomes comparable to the characteristic length scale of that given property, providing control over functionality through control of structure. Depending upon the application, layer thicknesses may vary from a fraction of a nanometre to few tens of nanometres. Since – in such multilayers – a large fraction of atoms resides at the surface/interfaces, the interfacial region plays a dominant role in determining their properties. Therefore, it is important to elucidate the interface

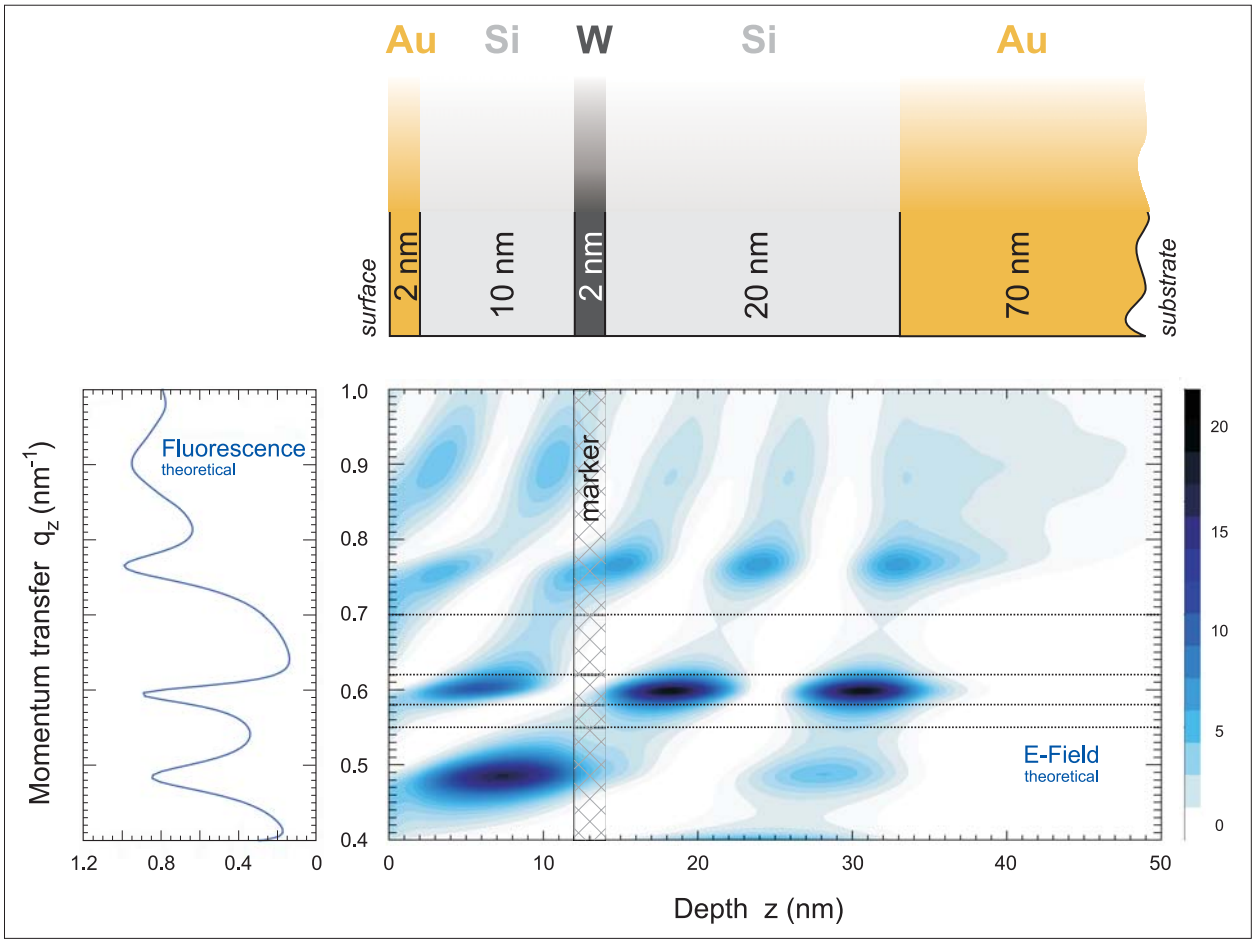

Fig. 2: Intensity distribution of the electrical wave field inside the sample versus the momentum transfer calculated at 10.3 keV (tungsten L-edge) together with the corresponding W fluorescence signal. Details of the multilayer structure are given in the upper part.

structure in order to understand their novel properties as well as to tailor the same via customized interface structures.

X-ray based characterization techniques are powerful tools for the study of atomic scale structure of materials. However, information obtained through x-ray diffraction techniques is usually averaged over the penetration depth of the probing x-rays, i.e., several microns for standard geometries. Depth selectivity can be obtained by generating x-ray standing waves (XSW) inside a layered structure by exploiting the effect of total reflection from an underlying layer composed of high Z material like Au [1]. Depth selectivity can be further enhanced when waveguide structures are used [2]. The geometry of the performed experiment is sketched in Fig. 1 together with the excitation modes of the x-ray standing wave.

Since the intensity of the x-rays is strongly localized in the region of antinodes, the standing wave field can be used as a localized probe with a sub-nanometer spatial resolution along the z-direction.

In case of a marker layer embedded into appropriate spacer layers, the fluorescence from the marker will depend upon the x-ray intensity at that point. As the angle of incidence of the probing x-rays with respect to the sample surface, θ, increases, the antinode position will move to larger depths. Whenever an antinode passes across the marker layer the corresponding fluorescence will exhibit a maximum as illustrated in Fig. 2. Thus, the q_z dependence of the fluorescence provides weighted information for a given element from different depth below the surface. The momentum transfer along z-direction is defined as $q_z = 4\pi \sin\theta / \lambda$, with λ denoting the wavelength of the probing x-rays.

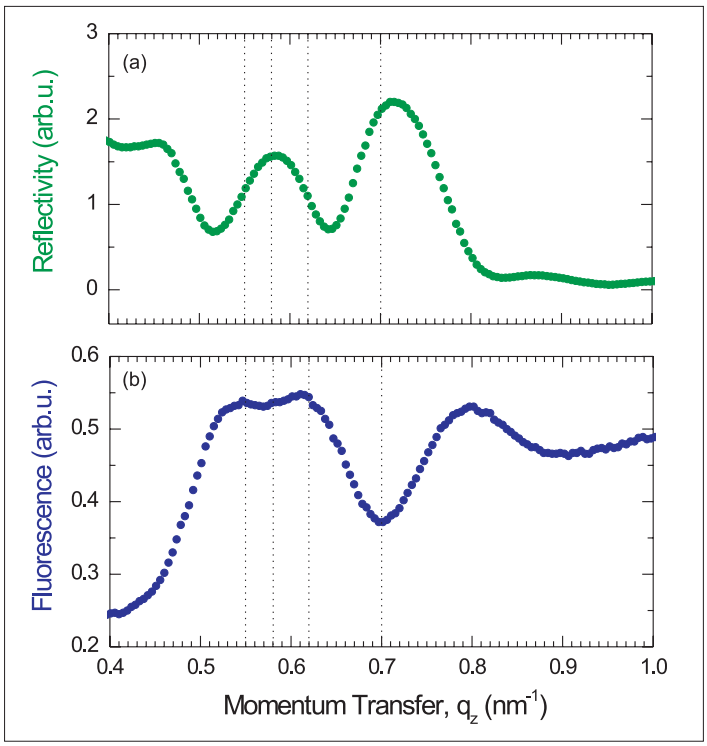

Fig. 3: Fluorescence and reflectivity intensity distribution recorded at 10.3 keV.

Here the capability of this technique is demonstrated in the study of swift heavy ion induced intermixing between a thin metal marker layer and silicon. Metal silicides are important for metallization applications in device production because of their low metal like resistivity, and high temperature stability and high electro-migration resistance. In this context, formation of metal silicides by heavy ion induced mixing has attracted considerable attention [3]. More recently, use of swift heavy ions for in-situ preparation of silicide thin films has been explored [4].

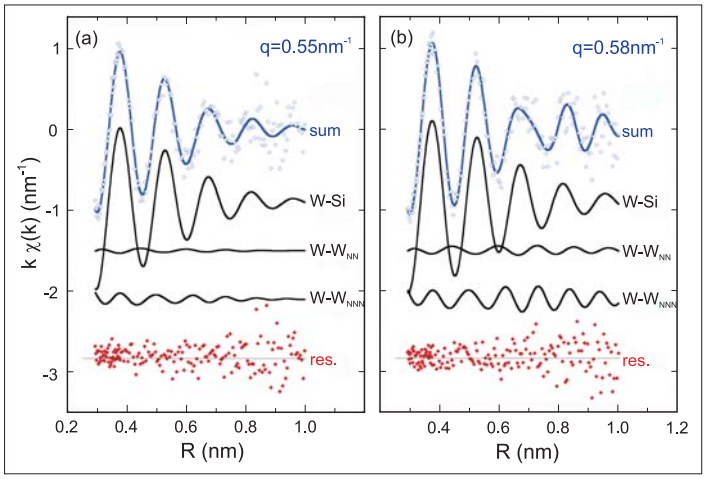

Fig. 4: XAFS data recorded at selected q_z together with considered fitting contributions.

The mechanism of energy transfer from the electronic system to atomic motion and subsequent intermixing is still not properly understood. Thus, a systematic study is needed in order to refine the model of ion-solid-interaction. Since intermixing can be as small as a nanometre or less, such studies require depths profiling techniques with a resolution of better than 1 nm. X-ray fluorescence measurements under standing wave conditions can provide the required depth resolution.
A waveguide structure was deposited on commercial Si substrate using magnetron sputtering. Details of the multilayer structure are given in Fig. 2. X-ray fluorescence patterns of the samples were recorded prior and after irradiation with 600 MeV Au ions from the ion beam laboratory ISL at the Hahn-Meitner-Institut Berlin. The bending magnet beamline KMC2 at the Berlin synchrotron radiation facility BESSY was used to set up the nanoprobe XAFS system. The x-ray beam in an energy range of 10 keV to 14 keV was monochromized by a double-graded-crystal monochromator and collimated in both directions using two slit systems and a collimating mirror. PIN diode detectors were utilized to measure both, the reflected beam and the fluorescence signal of the sample.

Fig. 3 shows the experimentally observed reflectivity (a) and tungsten L-edge fluorescence intensity (b) curves versus momentum transfer q_z recorded at 10.3 keV incidence energy. Maxima in fluorescence yield occur whenever an antinodal region of the XSW field coincides with the W marker layer. Different maxima correspond to different modes of the XSW. For the reflectivity signal, a reversed behaviour is expected and experimentally observed.

Fig. 4 shows tungsten L-edge data for two selected but only slightly different q_z together with the contributions which where taken into account for fitting. Even for only very small differences in, i.e., changes in information depth in the sub-nanometre range, significant changes in the XAFS signal and the fitting contributions were observed. The experimental data of the pristine sample as well as of the irradiated samples were fitted with a three-shell model: i) a W-Si shell, which is the main contribution to the whole XAFS signal, ii) a W-W shell similar to the W-W nearest neighbour distance in metallic W, and iii) a W-W shell which is similar to the W-W next nearest neighbour dis-

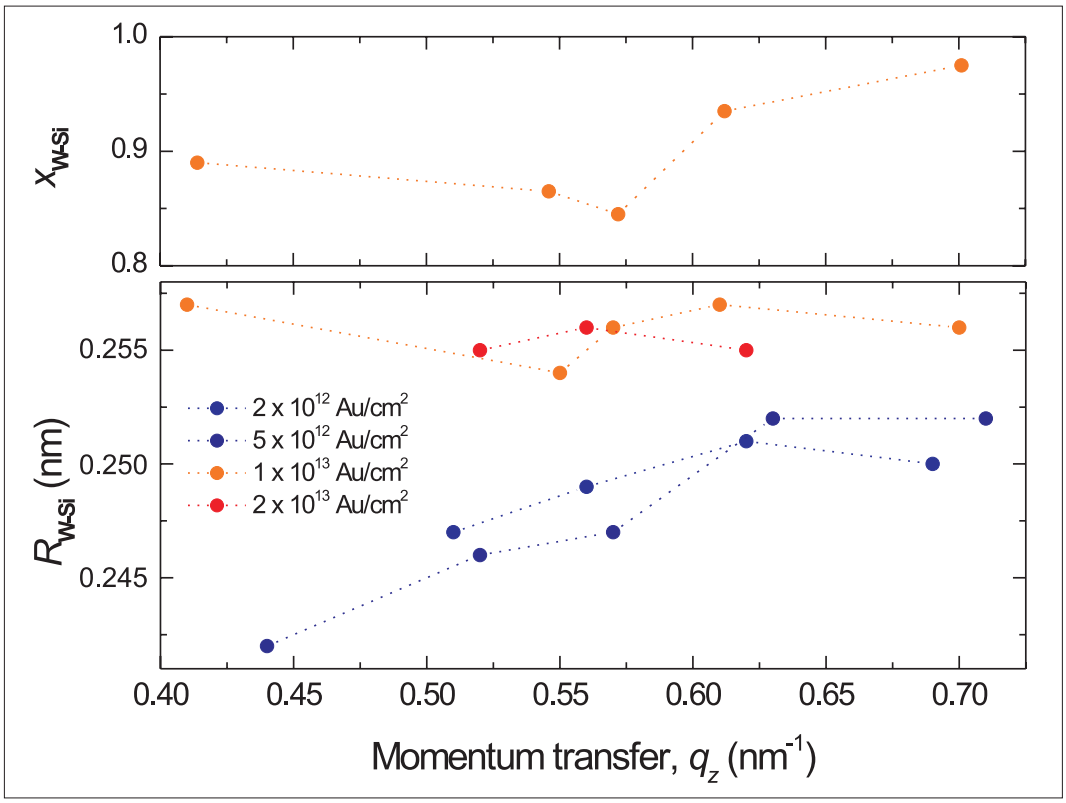

Fig. 5: Fluorescence and reflectivity intensity distribution recorded at 10.3 keV.

tance in metallic W. The XAFS data of the pristine sample suggest about 60% W in metallic environment and 40% in WSi_2. Irradiation provokes partial dissolution of W in Si giving rise to a higher fraction of W-Si correlation.

Fig. 5 shows the variation of fraction of W-Si bonds (a) and the W-Si bond length (b) as a function of q_z. A minimum of $x_{W\text{-}Si}$ is found at q_z=0.57nm^{-1}, i.e., at the position of the marker layer. $R_{W\text{-}Si}$ clearly depends on the irradiation fluence Φt. For $\Phi t \geq 1\times10^{13}$Au/cm^2 W-Si correlations dominate while metallic W contribution decreases. Φt is depth independent, indicating large intermixing. For $\Phi t \geq 1\times10^{13}$Au/cm^2 $R_{W\text{-}Si}$ is systematically shorter and increases with depth. A small $R_{W\text{-}Si}$ value is consistent with W-rich structures like W_5Si_3, whereas larger W-Si distances point to Si-rich WSi_2 phase. Depth resolved information about the various phases formed after irradiation are valuable for understanding the mechanisms of mixing, i.e., give insights into the interaction between high energetic ions and solid matter.

[1] S.K. Ghose, B.N. Dev, A. Gupta, Phys. Rev. B **64**, 233403 (2001)
[2] A. Gupta, R. Rajput, V.R. Reddy, M. Gupta, S. Bernstorff, H. Amenitsch, Phys. Rev. B **72**, 075436 (2005)
[3] R. Ayache, E. Richter, A. Bouabelleou, Nucl. Instrum. Methods B **216**, 137 (2004)
[4] P. Dhuri, A. Gupta, S.M. Chaudhari, D.M. Phase, D.K. Avasthi, Nucl. Instrum. Methods B **156**, 148 (1999)

Corresponding author:
N. Darowski
darowski@hmi.de

Element sensitive imaging of rodent and insect brains in 2D and 3D with neutrons and photons

M Kühbacher[1], B Grünewald[2], G Falkenberg[3], F Beckmann[4] and A Kyriakopoulos[1]
■ 1 HMI, SF6 ■ 2 Institut für Neurobiologie, Freie Universität Berlin, Berlin, Germany
■ 3 Hamburger Synchrotronstrahlungslabor HASYLAB at Deutsches Elektronen-Synchrotron DESY Hamburg, Germany ■ 4 GKSS-Research Center Geesthacht, Institute for Materials Research, Geesthacht, Germany

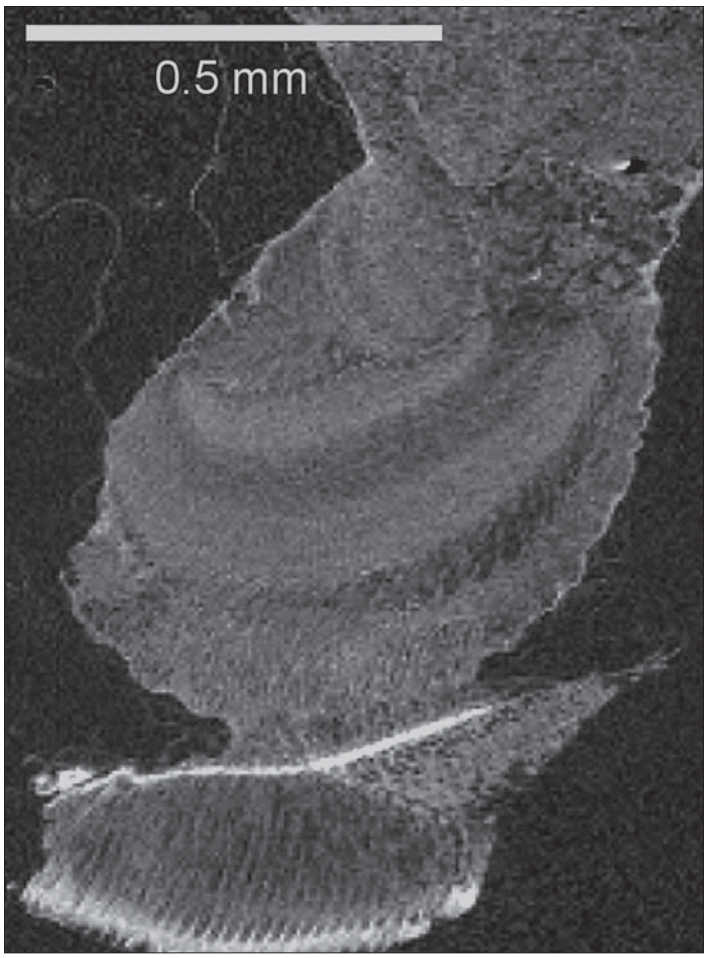

Fig. 1: Visualized section of a part of the brain of a honeybee after tomographic reconstruction.

The combination of radiotracers produced with neutrons at the reactor of the Hahn-Meitner-Institut and photons produced at HASYLAB and BESSY constitutes a powerful scientific toolkit for 2D and 3D chemical imaging of metal- and metalloid-containing proteins is in specific tissues - in particular in the central nervous system. In a series of experiments, this combination was used to allow new insights into the way nature solved complex structural and physiological chemical tasks.

In living organisms, metals and metalloids are involved in the production of free radicals – the causing factor for oxidative stress. However, metals and metalloids are also necessary components of specific antioxidant enzymes. The identification of metalloproteins, i.e. metal containing proteins, and the determination of their cellular and subcellular distribution will provide valuable hints with regard to the function and biological role of the metals and metalloids in question. Metalloproteomics, i.e. proteomics focused on metalloproteins, requires specific bioanalytical tools to identify these compounds and to study their distribution and biological functions.

A micro-synchrotron radiation X-ray fluorescence procedure (μ-SRXRF) was developed as such a bioanalytical tool. The procedure allows fast scanning of histological tissue sections with a focused X-ray beam and determination of the trace elements distributed among the brain areas by means of their characteristic X-ray emission. With new X-ray optics, a spatial resolution down to the micrometer range is achievable. The third spatial dimension of the elemental distribution pattern can be investigated by tomographic techniques. Microtomography using synchrotron radiation allows us to visualize the internal microscopic structure of small brains like the brain of the honeybee. While classical tomography provides a spatial resolution in the millimetre range, microtomography is expanding the spatial resolution down to a few micrometers. Beside other tomographic techniques based on absorption, phase-contrast, or X-ray scattering, X-ray fluorescence computed tomography achieves multielement capability by recording characteristic X-ray emission. The brains of diverse insects were investigated by

synchrotron radiation-based computered microtomography at BESSY and HASYLAB.

By labelling rats with radiotracers, the labelling techniques were optimized and the limit of detection improved to such an extent that even those labelled compounds present in the brain at very low concentrations could be detected. Fig. 3 shows the autoradiogram of a 10 µm thin brain-section of a rat radiolabelled with ^{73}As.

Fig. 2: Micro-tomographic data obtained by X-ray absorption tomography. The brain and the antennae of the honeybee head are visualized by segmentation.

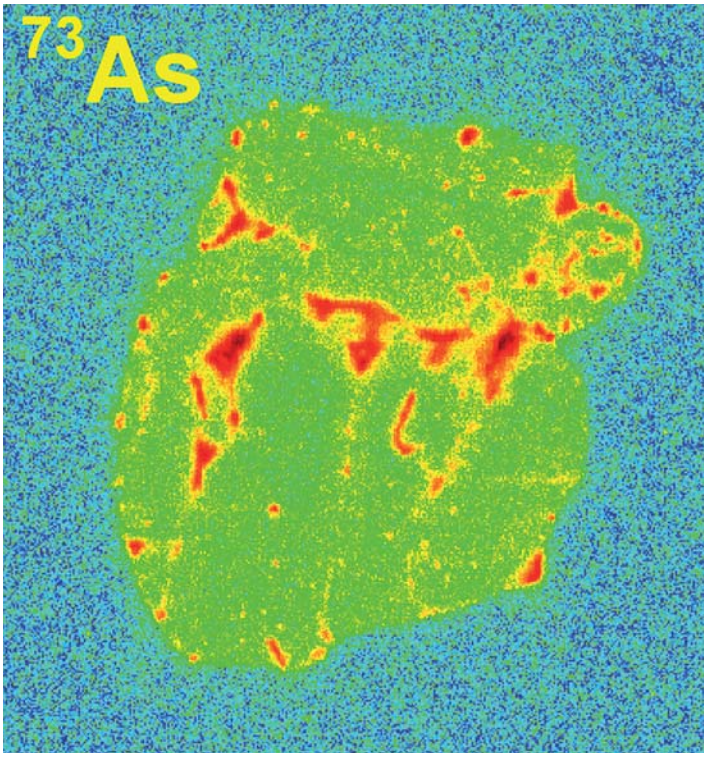

Fig. 3: Autoradiogram of ^{73}As in a 10 µm thin brain-section of a radiolabelled rat. The colours indicate the intensity of the radionuclide (red = high, blue = low).

Corresponding author:
M. Kühbacher
kuehbacher@hmi.de

Structure of the ^{10}Be nucleus: shell-model versus cluster structures

H. G. Bohlen[1], T. Dorsch[1,2], Tz. Kokalova[1], W. von Oertzen[1,3], Ch. Schulz[1], and C. Wheldon[1]
■ 1 HMI, SF7 ■ 2 TU München, Department E12 ■ 3 FU Berlin, Fachbereich Physik

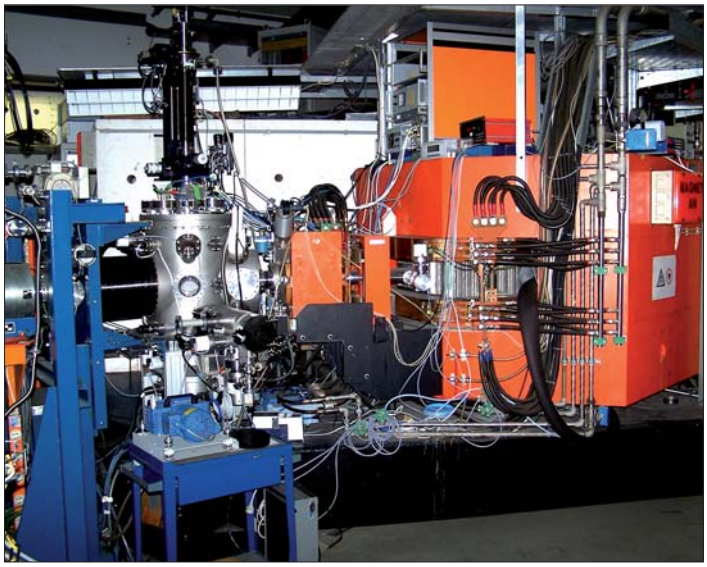

Fig. 1: The Q3D magnetic spectrograph at the HMI cyclotron. The quadrupole magnet and a small multipole magnet is seen in front of the first of three big dipoles (on the right). The beam line enters from the left into the cylindrical scattering chamber. From here the reaction products have to go a distance of 7.5 m to the focal plane, where they are detected.

In light nuclei, as for example Beryllium or Carbon isotopes, a competition exists between structures, (i) where all nucleons are bound in a central potential giving rise to shell-model states, or (ii) where α-clusters (^{4}He) with their high internal binding energy create a multi-centre structure. In the latter case even molecular states can be formed, i. e., for isotopes with neutron excess, where the exchange of the valence neutrons between the clusters gives rise to some extra binding energy. These effects are especially strong for states at excitation energies near the α-particle separation energy S_α [1], where an α-cluster is only weakly bound or is in a resonance state. In that case extra neutrons can be bound in molecular σ- and π-orbits for p-shell nuclei [2] with large distances between the clusters. Band structures result for such strongly deformed states. For a rotational band, which is built on a specific shell-model configuration, the maximum angular momentum is determined by the participating shell-model orbits. But higher angular momenta are possible for cluster or molecular structures, as has been shown by many theoretical calculations. In ^{10}Be such structures have been already identified some time ago [2].

We studied these structures of ^{10}Be at HMI's accelerator facility ISL using the ^{12}C(^{12}C,^{14}O)^{10}Be reaction at 211.4 MeV. The measurements were performed at the Q3D magnetic spectrograph (Fig. 1) at ISL. In Fig. 2 the excitation energy spectrum of ^{10}Be is plotted versus the scattering angle within the angular acceptance. Angular distributions were measured in this way for all the observed states in two angular sections (see the black and red data sets in Fig. 3). In this specifically chosen reaction the shape of the angular distributions is characteristic for the spin and parity of the states.

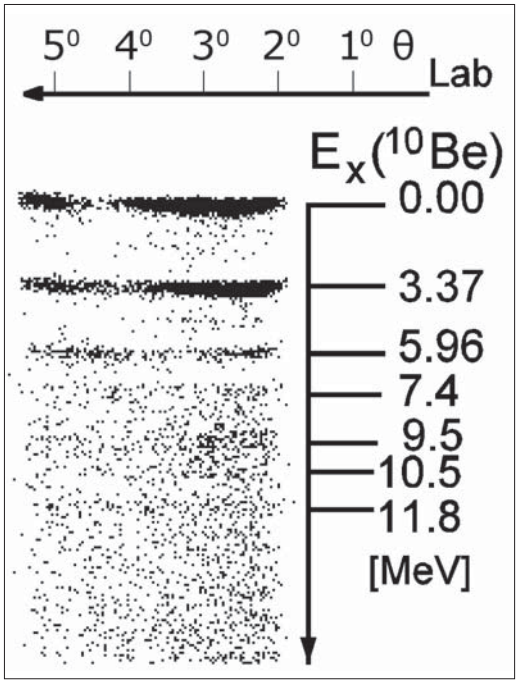

Fig. 2: Two-dimensional plot of the excitation energy E_x (in MeV)of ^{10}Be versus the scattering angle θ_{Lab} for out-going ^{14}O particles from the ^{12}C(^{12}C, ^{14}O)^{10}Be reaction. States of ^{10}Be up to 11.8 MeV excitation energy are observed.

Four bands have been identified in ^{10}Be (see Fig. 4). The structure information is deduced using the well known relation between angular momentum J and excitation energy E_x for members of a rotational band, where the inverse of the moment-of-inertia Θ of the rotating object enters as proportio-nality factor (these correspond to the slopes in Fig. 4). Information about the size and shape is deduced from the experimental value of Θ by comparing it to results from different models.

For the ground-state band (0^+_1, 2^+_1, 4^+) properties of the first two states can be described by shell-model (SM) calculations. However, a 4^+ member does not exist in the SM, whereas cluster models (CM) predict such a state at excitation energies in the range 10 – 13 MeV. In our measurement we identified this 4^+ state uniquely at E_x= 11.8(1) MeV by the shape of its angular distribution. This is in very good agreement with the CM-predictions. Detailed calculations within the cluster-model show a pronounced oblate shape. The second

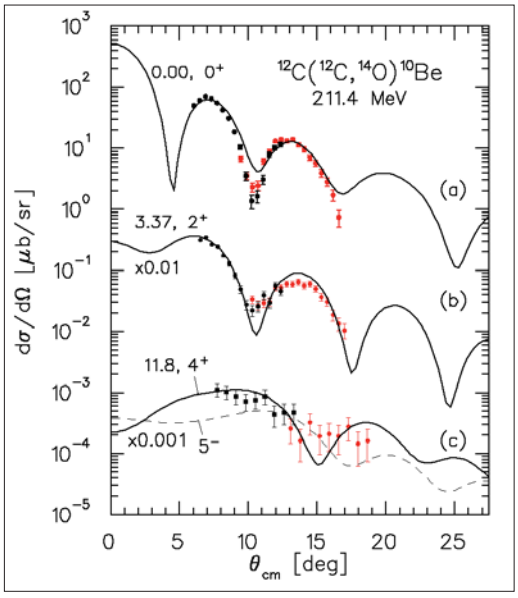

Fig. 3: Angular distributions of the 0^+, 2^+ and 4^+ states, which form the ground-state rotational band. The different shapes, especially at scattering angles below 15°, are characteristic for the spin and parity of corresponding states. Solid and dashed lines correspond to results from coupled-channels calculations.

band (K=2^+ in Fig. 4) has only two members, a 2^+_2 and a 3^+ state. The latter could be identified in our measurement by the decomposition of the angular distribution from the peak observed in Fig. 2 at 9.5 MeV. Both states have a large prolate deformation.

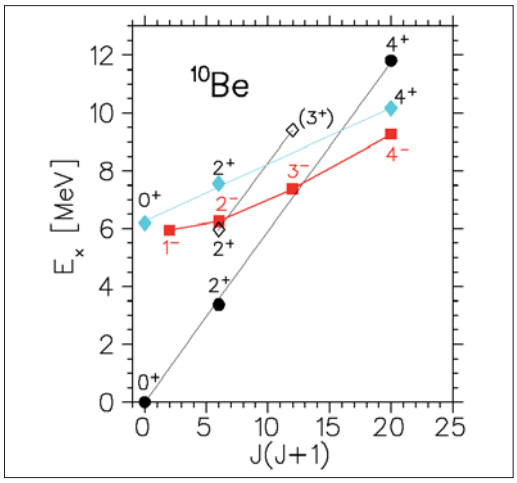

Fig. 4: Four different bands of ^{10}Be:
1. Ground state band (black dots)
2. K=2^+ band (open diamonds).
3. Molecular band (blue diamonds)
4. Odd-parity band (red squares)

The second 0^+ rotational band (0^+_2, 2^+_3, 4^+) built on the 0^+ state at 6.18 MeV. It is known to have a molecular structure: two α-particles at a mean distance of about 5.9 fm form a two-centre cluster system. The additional two neutrons of ^{10}Be are both in σ-orbits of the 1p-shell and stabilize the 2α-system as particle-stable structure. The 4^+ state of this band has also been uniquely identified recently [3] at 10.15 MeV. Such a *molecular* band does not exist in SM-calculations. The members of the odd-parity band (1^-, 2^-, 3^-, 4^-) are strongly populated in one-neutron transfer reactions on ^{9}Be$_{g.s.}$($3/2^-$). These states are described by the coupling of the $3/2^-$ core to a one-neutron configuration in the (sd)-shell. However, the excitation energies obtained from the SM are about 2 MeV too high (except for the 1^- state), whereas the CM describes these energies correctly with a σ- and a π-orbit for the neutrons.
Further information can be found in [4].

[1] K. Ikeda, Suppl. Prog. Theor. Phys. (Japan), Extra Number (1968).
[2] W. von Oertzen, Z. Physik A **357** (1997) 355.
[3] M. Freer et al., Phys. Rev. Lett. **96** (2006) 042501.
[4] H.G. Bohlen et al., Phys. Rev. C **75** (2007) 054604

Corresponding author:
H.-G. Bohlen
bohlen@hmi.de

The role of excited S multiplets in the magnetic relaxation of the high anisotropy barrier Mn_6 Single Molecule Magnet.

T. Guidi[1], O. Pieper[1,2], B. Lake[1,2], S. Carretta[3], P. Santini[3], G. Amoretti[3], J. Van Slageren[4], M. Russina[5], A. Buchsteiner[6], C.J. Milios[7], E.K. Brechin[7]

■ 1 HMI, SFN1 ■ 2 Technische Universität Berlin, Germany ■ 3 Dipartimento di Fisica, Universita' di Parma, Parma, Italy ■ 4 Physikalisches Institut, Universität Stuttgart, Stuttgart, Germany ■ 5 HMI SF1 ■ 6 HMI SF2 ■ 7 School of Chemistry, University of Edinburgh, Edinburgh, UK

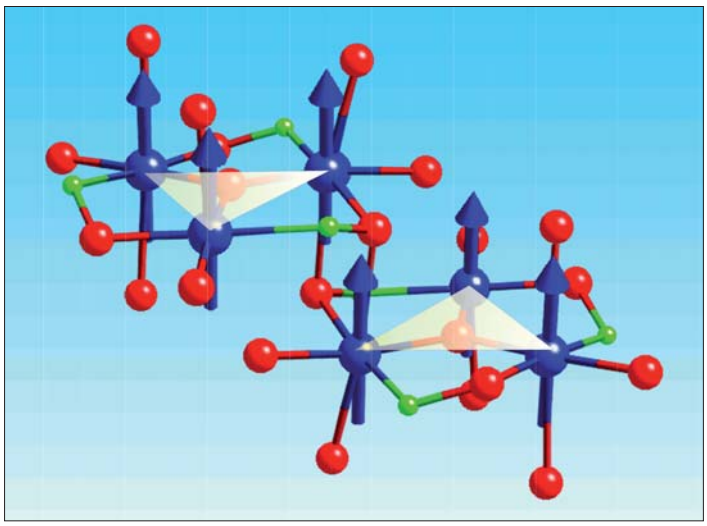

Fig. 1: Structure of the Mn_6-(Et $saoH_2$) molecular core. The Mn(III) ions are located at the vertices of two oxo-centered triangles. Color scheme: Mn, blue, O, red, N, green. H and C ions are omitted for clarity.

The present technology for data storage devices is dominated by magnetic hard disk drives. During the last decades, the ever-increasing demand for high performing, light and reduced-sized devices has driven the exponential increase of areal density storage. This behaviour is foreseen to end when the so called 'superparamagnetic limit' is reached. The continuous shrinking of the volume of the magnetic particles, which store one bit of information, is limited. When the magnetic energy stored in one grain, which is proportional to the volume of the particle, is comparable to the thermal energy, the magnetization M will freely fluctuate resulting in a loss of information. Therefore new concepts and systems are needed to provide a solution for the next generation of technology.

Single Molecule Magnets (SMM) are promising systems for the realisation of ultra-fast/ultra-high density classical bits. They are clusters consisting of a small number of transition metals ions, exchange coupled via organic ligands and arranged in a crystal lattice with a negligible interaction between different magnetic units. The dominant exchange interactions between the spins of the ions give rise to a high-spin ground state S associated with the cluster. At the same time, the presence of a large easy-axis magneto-anisotropy determines the Zero-Field Splitting (ZFS) of the S state sublevels, with an energy barrier that separates the "spin-up" (S_z=S) and "spin-down" (S_z=–S) states, of height given by U~|D|S^2 (where D is the axial anisotropy parameter). These systems thus represent a bottom-up approach to nanoscale magnetism. The main focus of the research in this field is to find the right ingredients for the synthesis of systems with high enough anisotropy to hinder thermal fluctuations, and allow storage of a bit of information in just one single molecule.

Considerable effort has been devoted to increasing the barrier height and thus making technological applications feasible at temperatures higher than the cryogenic range. Up to now, the maximum height for the anisotropy barrier (about 74 K) has been obtained for the Mn_{12} cluster [1].

Recently, a new series of Mn_6 clusters of generic formula $[Mn_6O_2(oxime)_6(carboxylate)_2(EtOH)_n(H_2O)_m](EtOH)_y$, displaying a SMM behaviour has been synthesized.

The magnetic core consists of six Mn(III) (s=2) ions arranged into two $\{Mn_3(\mu_3\text{-}O)\}$ triangular subunits bridged together by two oximato oxygen atoms (Fig. 1). By changing the nature and the arrangement of ligands, a series of compounds with different Mn-Mn exchange couplings and total spin ground state S has been obtained.

In particular, the $[Mn_6O_2(Et\text{-}sao)_6(O_2CPh)_2(EtOH)_4(H_2O)_2]\cdot{}_2EtOH$ (**2**·2EtOH) compound (briefly Mn_6-(Et $saoH_2$)) has a high-spin S=12 ground state due to the dominant intra- and inter-triangle ferromagnetic (FM) interactions. A preliminary fit of the magnetization data indicates an axial ZFS parameter D=–0.62 K, leading to an upper-limit estimate for the anisotropy barrier of U=|D| S^2≈89K, the highest so far. However, a much

smaller value for the experimental effective anisotropy barrier U_{eff} (~53 K) has been deduced from relaxation data [2]. This large discrepancy has been tentatively attributed to the presence of low-lying excited states, which could play a role in the relaxation dynamics and lower the energy barrier for the reversal of M.

To shed light on this issue, an accurate determination of the low-energy eigenstates and eigenvalues is required. Hence, we have used the NEAT time of flight spectrometer to investigate the spin dynamics of the Mn_6-(Et $saoH_2$).

By measuring with an incident wavelength of 4.6 and 5 Å, we have directly observed the inter-multiplet transitions from the S=12 ground state to the low-lying S=11 excited spin states (Fig. 2). These measurements provide essential information to determine the intra- and inter-triangles exchange parameters and the single-ion anisotropies. In particular, we have found that there are many excited multiplets (with S<12) partially nested within the S=12 ground state multiplet (see Fig. 3). This nesting leads to a very large degree of S mixing [3] of the spin wavefunctions and strongly influences the relaxation behavior. In fact, several inter-multiplet relaxation paths, via a combination of multi-step Orbach and tunneling processes, contribute to the decay of the molecular magnetization. This leads to a large reduction of the effective energy barrier.

To model this system the full spin Hilbert space has to be included in the calculations and all the main local crystal-field (CF) parameters (at least three for each inequivalent Mn ion) have to be considered. Preliminary fits of the neutron cross section are shown in Fig. 2, which account very well for the main features of the low-resolution spectra.

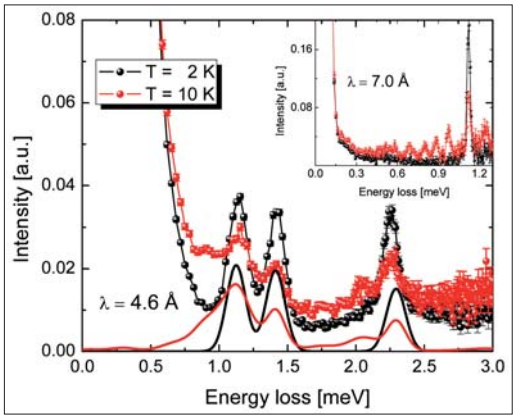

Fig. 2: Inelastic neutron spectra of Mn_6-(Et $saoH_2$) sample collected on NEAT time-of-flight spectrometer using an incident wavelength of 4.6 Å and 7 Å (inset) for two different temperatures, 2 K (black) and 10 K (red). The continuous lines represent the spectra calculated with the best fit exchange and anisotropy parameters.

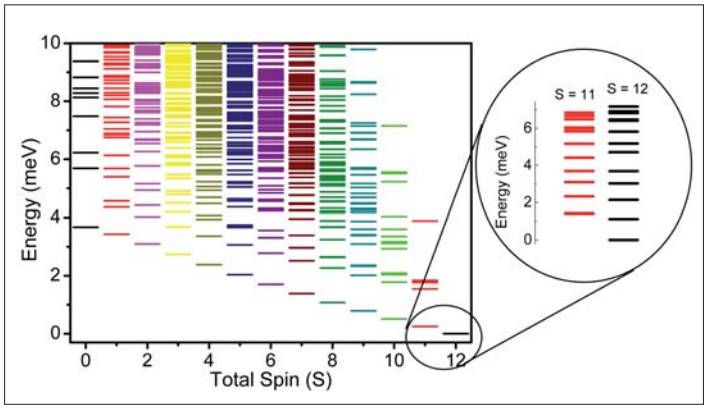

Fig. 3: Eigenvalues of the isotropic part of the Hamiltonian as a function of the total spin quantum number S. The magnification shows the anisotropy energy level splitting of the two lowest energy S states evidencing the nesting of excited states within the S=12 ground multiplet.

To investigate in detail the anisotropic part of the Hamiltonian, we have performed high-resolution measurements at = 7Å and at two different temperatures, 2 and 10 K. Several excitations within the ground S=12 multiplet and within the lowest excited S=11 multiplet (Fig. 2, inset) have been observed, confirming the nesting of the lowest excited S multiplets within the ground one. Theoretical work is in progress to definitely fix the CF parameters.

Recently, a chemical engineering of the material by further changing the ligands has resulted in the synthesis of an analog Mn_6 compound, Mn_6O_2(Et-sao)$_6$ $(O_2CPh(Me)_2)_2(EtOH)_6$) [4], with a stronger FM exchange and hence higher-lying excited spin multiplets. This reduces their role in magnetic relaxation and substantially increases the effective barrier to U_{eff} = 86.4 K. This new Mn_6 compound has to date the highest effective barrier of any SMM, including Mn_{12}.

[1] Sessoli, R.; Gatteschi, D.; Caneschi, A.; Novak, M. A. Nature 1993, **365**, 141; N.E. Chakov, J. Lee, A. G. Harter, S. O. Hill, N. S. Dalal, W. Wernsdorfer, K. A. Abboud and G. J. Christou,J. Am. Chem. Soc., **128**, 6975 (2006)

[2] Milios, C. J.; Vinslava, A.; Wood, P. A.; Parsons, S.; Wernsdorfer, W.; Christou, G.; Perlepes, S. P.; Brechin, E. K. J. Am. Chem. Soc. 2007, **129**, 8.

[3] S. Carretta, P. Santini, G. Amoretti, T. Guidi, J. R. Copley, Y. Qiu, R. Caciuffo, G. Timco, and R. E. Winpenny, Phys. Rev. Lett. **98**, 167401 (2007).

[4] C. J. Milios, A. Vinslava, W. Wernsdorfer, S. Maggach, S. Parson, S. P. Perlepes, G. Christou, E. K. Brechin, J. Am. Chem. Soc. **129**, 2754, (2007).

Corresponding author:
T. Guidi
tatiana.guidi@hmi.de

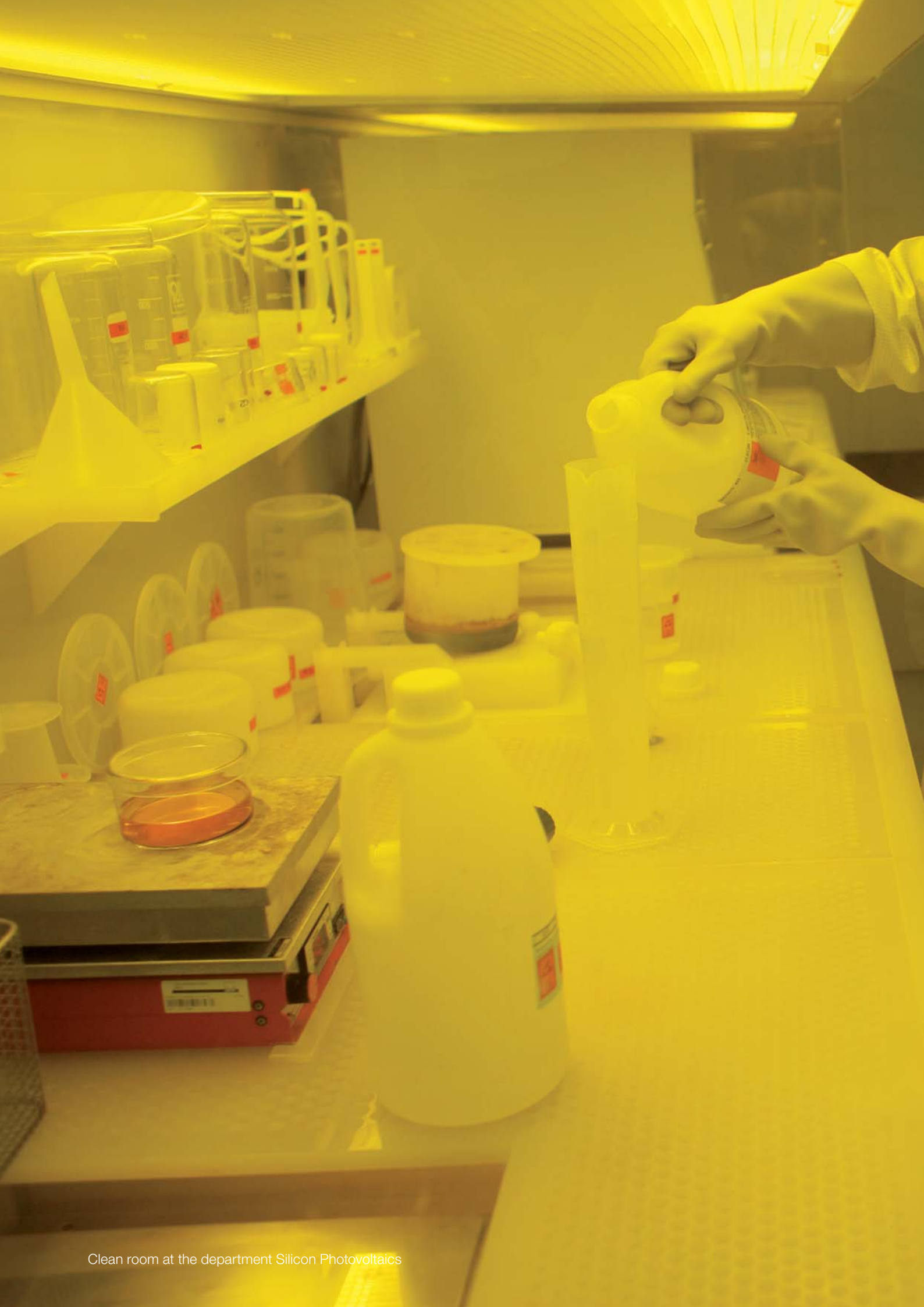

Clean room at the department Silicon Photovoltaics

Scientific Highlights
Solar Energy Research 2006

Electronic states in *a*-Si:H/*c*-Si heterostructures

L. Korte, A. Laades, M. Schmidt
■ HMI, SE 1

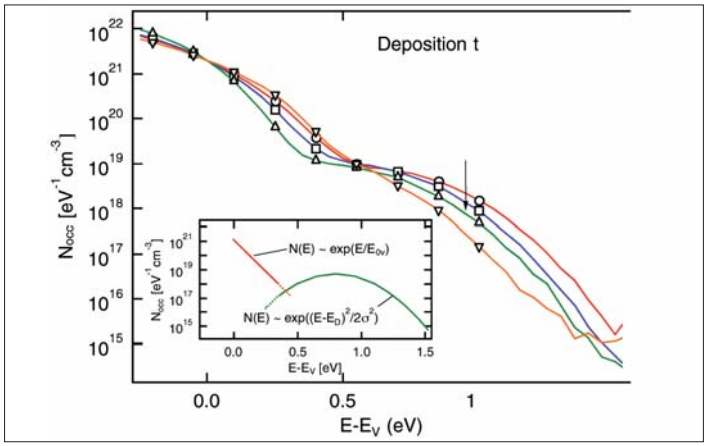

Fig. 1: Density of occupied gap states N_{occ}(E) of a series of *a*-Si:H(i)/*c*-Si(p) samples with variation of the *a*-Si:H deposition temperature T_S. E_V is the origin of the abscissa. Arrows mark the Fermi level positions. The spectra are normalized to $2 \cdot 10^{21}$ states/(eV·cm^3) at the valence band edge. Inset: Decomposition of the DOS into Urbach tail and dangling bond distribution (schematic).

Introduction

The key to obtaining high cell efficiencies of amorphous-crystalline (*a*-Si:H/*c*-Si) heterojunction solar cells with monocrystalline or polycrystalline silicon absorbers is the quality of the *p/n* heterojunction formed by the deposition of *a*-Si:H emitter. The use of heterostructures for the realisation of *p/n* junctions requires a careful analysis of electronic states in the involved solids and at their hetero-interface.

The main parameters determining charge transfer and recombination activity are the band offsets and the Fermi level position at the *a*-Si:H/*c*-Si interface as well as the density and energetic distribution of defect states (DOS) at the interface and in the thin amorphous layer. Little is known about the electrical properties of ultra-thin films and their interfaces. In recent years, we have developed experimental techniques that are especially well-suited to the characterisation of such films and their interface to the substrate [1,2,3].

Sample Preparation

All investigated *a*-Si:H layers, with thicknesses of 12 to 17 nm, were deposited on <111> oriented silicon by RF excited PECVD (13.6 MHz, P_{RF} = 13 mW/cm^2) using silane, SiH_4, as precursor. Prior to *a*-Si:H deposition, all wafers were cleaned (standard RCA-procedure), followed by an HF dip (1% HF, 1 minute) and immediate transfer into the PECVD system.

Constant Final State Photoelectron Spectroscopy

The *a*-Si:H density of states (DOS) was obtained using photoelectron spectroscopy in the so-called constant final state yield spectroscopy mode (CFSYS) [4,5]. Here, instead of the photoelectron analyser energy, the energy of the exciting photons is varied. This has the advantage that for all points in the spectrum (photoelectron yield γ_{int} *vs.* photon energy $h\nu$), photoelectrons excited into the same conduction band state(s) – final states – are measured. Thus, details of the conduction band structure have no influence on the shape of the spectrum. In general, this technique is only available at tuneable photon sources such as synchrotrons; our set-up provides the same functionality – albeit at a very limited photon energy range of $h\nu$=3–7eV – in a conventional UPS/XPS laboratory system. From the measured spectra, the position of the Fermi level E_F, of the valence band edge E_V and the distribution of occupied states N_{occ}(E) normalised to units of [states/(cm^{3}eV)] are obtained. The measured distribution is a weighted average of the DOS of the sample up to a depth of 7 to 10 nm. For further details see [1,2,5].

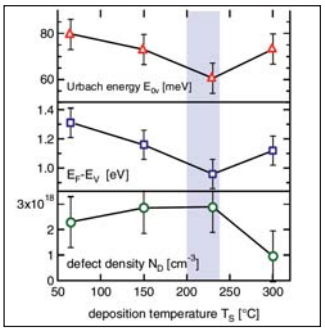

Fig. 2: Data derived from the series shown in Fig. 1: Dependence on T_S of (i) Urbach energy E_{0v}, (ii) Fermi level position $E_F - E_V$ and (iii) integrated defect density N_D.

Surface Photovoltage

To determine the band bending in the *c*-Si and a characteristic time constant for recombination at the *a*-Si:H/*c*-Si interface, surface photovoltage

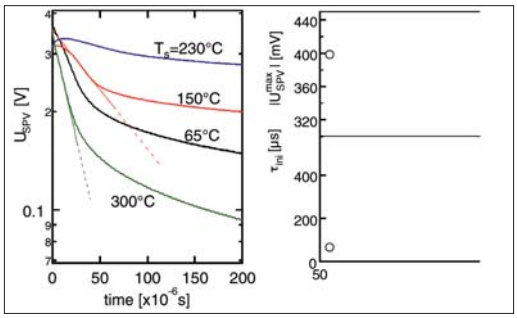

Fig. 3: Left: Surface photovoltage transients measured on the deposition temperature series shown in Fig. 1. For T_S=150 and 300°C, exponential fits to obtain τ_{ini} are plotted. Right: Dependence of the maximum photovoltage $|U^{max}_{SPV}|$ and the slope parameter of the initial fast decay τ_{ini} on T_S. ○: for the series of Fig. 1, □: for an additional series deposited under the same conditions. Lines are guides to the eye.

(SPV) [6,7,8] measurements were used. Upon intense illumination of the sample by a laser pulse ($h\nu$ = 1.35 eV, pulse duration 160 ns, intensity 10^{19} photons/(cm^{2}s)), excess charge carriers are generated, leading to a flattening of the bands and a split-up of the quasi Fermi levels of electrons and holes. The surface photovoltage of the sample is then measured capacitively as photovoltage pulse U_{SPV}. Because the sample is illuminated at a photon energy smaller than the band gap of *a*-Si:H (~1.7 eV), the latter acts as a window layer, the excitation of charge carriers takes place in the crystalline substrate. Their recombination can be characterised via the time dependent U_{SPV} decay.

Results

The densitiy of occupied states $N_{occ}(E)$ is shown in Fig. 1. The usual features, i.e. an exponential decay of the DOS at $E-E_V$ = 0...~0.4 eV and a Gaussian-shaped defect distribution up to E_F are observed. Fig. 2 shows parameters derived from Fig. 1: The Urbach energy E_{0v}, E_F and the integrated defect density of deep defects N_D *vs.* substrate temperature T_S during *a*-Si:H deposition. Both Urbach energy and E_F depend on deposition temperature and have a minimum at T_S=230°C. In contrast, N_D shows, within the accuracy of the measurement, no appreciable variation and is slightly higher than the value of $8\cdot10^{17}$ cm^{-3} reported for thick films. The shift of E_F correlates with a shift of the deep defect (Fig. 1). The corresponding SPV transients are presented in Fig. 3. The decay of the transient is an image of the recombination of photo-generated excess carriers that occurs predominantly at the *a*-Si:H/*c*-Si interface. The first ~50 µs of the decay are exponential, described by a time constant τ_{ini} that has a pronounced maximum at T_S ~ 200 – 230°C. The minimum of the initial photovoltage U^{max}_{SPV} lies at the same deposition temperature. As shown in [3], photoluminescence and the efficiency of solar cells processed with *n*-doped emitters prepared under identical conditions have a maximum at the same T_S.

In ref. [2], we calculate the Fermi level at the *a*-Si:H/*c*-Si interface. We find that E_F crosses the interface at only 45 meV above midgap. In Shockley-Read-Hall recombination statistics, the effective recombination velocity increases when E_F approaches midgap. However, the measured τ_{ini} is highest for E_F at the interface closest to midgap. Thus, the interface state density, which is assumed to be predominantly related to Si dangling bonds with back-bonds to the *c*-Si substrate, must be reduced after the deposition of *a*-Si:H under optimised conditions. Deposition under sub-optimal conditions, however, leads to an increase of the density of localised states in the gap, but close to the band edges (E_{0v} is increased). This causes enhanced recombination, which can be attributed to tunnel hopping of charge carriers into *a*-Si:H tail states and subsequent recombination via *a*-Si:H gap states (Fig. 4), as shown by EDMR measurements [9].

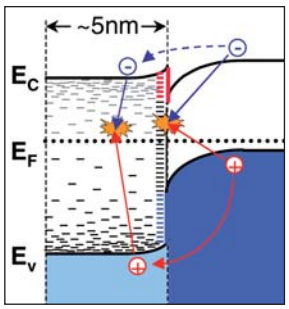

Fig. 4: Schematic band diagram of the *a*-Si:H/*c*-Si interface, arrows show the proposed tunneling and recombination paths.

[1] M. Schmidt, A. Schoepke, L. Korte, O. Milch, W. Fuhs, J. Non-Cryst. Sol. **338-340** (2004) 211.
[2] L. Korte, A. Laades, M. Schmidt, J. Non-Cryst. Sol. **352** (2006) 1217.
[3] K. v. Maydell, L. Korte, A. Laades, R. Stangl, E. Conrad, F. Lange, M. Schmidt, J Non-Cryst. Sol. **352** (2006) 1958.
[4] M. Sebastiani, L. D. Gaspare, G. Capellini, C. Bittencourt, F. Evangelisti, Phys. Rev. Lett. **75** (1995) 3352.
[5] L. Korte, PhD thesis, U Marburg / Hahn-Meitner-Institut Berlin, 2006 (HMI-Bericht Nr. 611, ISSN 0936-0891).
[6] A. Laades, PhD thesis, TU Berlin / Hahn-Meitner-Institut Berlin, 2005 (ISBN 978-3-86664 078-8).
[7] Y. Lam, J. Phys. D: Appl. Phys. **4** (1971) 1370.
[8] W. Füssel, M. Schmidt, H. Angermann, G. Mende, H. Flietner, Nucl. Instrum. Meth. Phys. Res. B **377** (1996) 177.
[9] C. Boehme, J. Behrend, K.v. Maydell, M. Schmidt, K. Lips, J. Non-Cryst. Sol. **352** (2006) 1113.

Corresponding author:
M. Schmidt
schmidt-m@hmi.de

Optical quenching of hydrogen donor states in zinc oxide

N. H. Nickel
■ HMI, SE 1

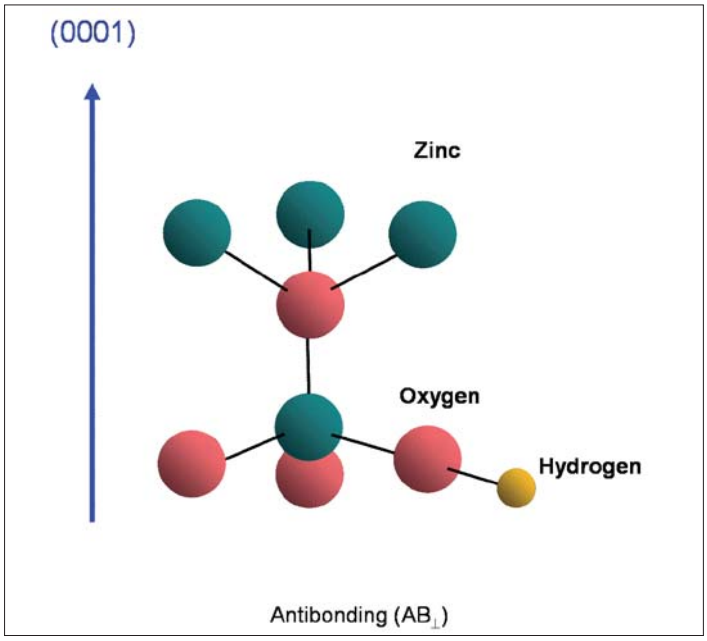

Fig. 1: Schematic depiction of the hydrogen shallow donor complexes in zinc oxide.

To fabricate fully transparent optoelectronic devices it is essential to grow n-type and p-type wide band-gap semiconductors. One of the materials of choice is ZnO. However, one of the major drawbacks is the fact that most available ZnO bulk crystals and thin films exhibit n-type conductivity. Interestingly, the unique properties of hydrogen in semiconductors have been identified as one of the major problems hindering p-type doping of ZnO [1,2]. Recently, the microscopic structure of H shallow donors was identified as O-H donor complexes in the antibonding configuration AB⊥ with a characteristic vibrational frequency of 3326.4 cm^{-1} [3]. The microscopic structure of this donor complex is schematically depicted in Fig. 1.

Post-hydrogenation of ZnO single crystals was achieved using ampoule hydrogenation. Then the samples were characterized with Fourier transform infrared spectroscopy using an instrumental resolution of 0.5 to 1.0 cm^{-1}. All measurements and light soaking were performed at 5 K. For light soaking a high efficiency LED was used that emitted blue light with a wave length of $\lambda = 450$ nm.

IR spectra of hydrogenated ZnO single crystals are shown in Fig. 2. Hydrogenation produces a strong local vibrational mode at $\nu = 3326.6$ cm^{-1} (Fig. 2(a)) that is due to the formation of O-H donor complexes where the hydrogen atom resides at the anti- bonding site [3]. Prior to the illumination the IR line associated with the H shallow donor shows the largest intensity. Then the ZnO sample was illuminated at 5 K for 2 min and the O-H absorption line was measured again. The intensity of the O-H vibrational mode decreased upon illumination (Fig. 2(b)). The quenching of the O-H infrared absorption line due to sub band-gap illumination is completely reversible. When the specimen was annealed at 100 K for 5 min the O-H absorption line recovered completely (Fig. 2 (c)).

The annealing behavior of the quenched O-H vibrational line was investigated in more detail. For this purpose a hydrogenated ZnO specimen was illuminated with blue light until the infrared signal was minimized. Then, the sample was heated to the desired temperature where it was annealed for 5 min. Subsequently the ZnO crystal was cooled to 5 K and the O-H absorption line was measured again. In Fig. 3 the change of the integrated O-H intensity, ΔI_{OH}, due to isochronal annealing is plotted as a function of the annealing temperature, T_A. With increasing annealing temperature ΔI_{OH} reaches a maximum at 45 K and then decreases to a value below zero at $T_A = 70$K. At higher annealing temperatures ΔI_{OH} exhibits a pronounced increase and eventually saturates at $T_A \geq 100$ K indicating that the intensity of the O-H vibrational line was completely recovered.
The temperatures at which quenching and recovery of the O-H absorption line occurs suggest that the underlying process is governed by charge carriers. Without changing the number of O-H complexes an increase or decrease of the infrared absorption line can only occur when the dipole moment, p, and hence, the infrared effective charge e^* changes $(p \propto e^*)$.

From the integral of the O-H absorption line, which amounts to 5.934 cm^{-1}, the effective charge of the O-H dipole can be estimated [4]. Assuming that all H atoms form ionized $O\text{-}H^+$ complexes an effective charge of the $O\text{-}H^+$ complex of $e^* = 0.135\ e$ was obtained. Since the number of H atoms accommodated in $O\text{-}H^+$ complexes might be lower than the total H concentration the calculated value for e^* denotes a lower limit.

When the sample is illuminated photo generated electrons are trapped in the O-H complex, which lowers the concentration of $O\text{-}H^+$ centers. This should result in the appearance of an additional vibrational mode due to $O\text{-}H^0$ complexes. However, an additional line due to the change of the dipole moment was not observed. This suggests that the dipole moment of the $O\text{-}H^0$ complex is too small to permit the observation of a vibrational mode by IR absorption.

The decrease of ΔI_{OH} between T_A = 50 and 75 K is unexpected and indicates that the underlying mechanism is more complex than the simple ionization of neutral O-H complexes. A decrease of ΔI_{OH} can only occur when electrons are captured by $O\text{-}H^+$ complexes. Since the annealing experiments were performed at low temperatures the capture of free electrons is unlikely. However, defect states that reside deeper in energy at E_D (see sketch in Fig. 3) can act as an efficient source of electrons.

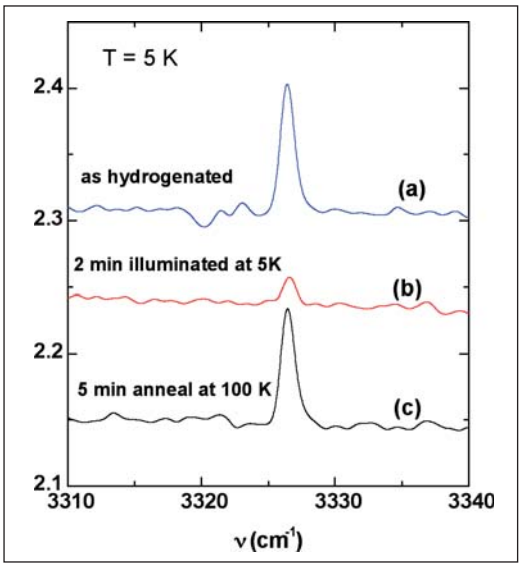

Fig. 2: IR absorption spectra of hydrogenated ZnO single crystals measured at T=5 K. (a) after hydrogenation, (b) after illumination at 5 K for 2 min, and (c) after a subsequent anneal at 100 K for 5 min.

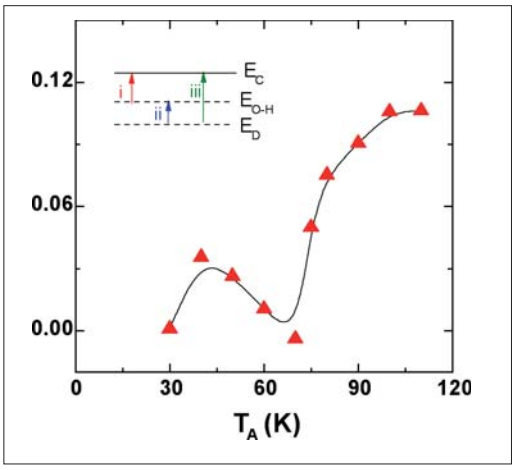

Fig. 3: Change of the integrated O-H vibrational line, ΔI_{OH}, as a function of the annealing temperature, T_A. Prior to each anneal the sample was illuminated with light from a blue LED. All spectra were measured at 5K.

During illumination these defect states also have captured electrons. With increasing T_A electrons trapped at E_D are thermally excited and recaptured by $O\text{-}H^+$ complexes (process ii in Fig. 3). For the experimental conditions chosen this results in a pronounced decreases of ΔI_{OH} for annealing temperatures between 50 and 75 K. Eventually as T_A increases further, electrons from E_D can also be excited into the conduction band (iii in Fig. 3). Consequently ΔI_{OH} increases rapidly.

In summary, we have shown that infrared absorption of the O-H vibrational line is very sensitive to sub band-gap illumination. Illumination at liquid-helium temperatures results in a pronounced decrease of the O-H absorption line. This effect is completely reversible by annealing the specimens at temperatures above T_A=30 K. The observed changes are attributed to the capture and release of electrons by O-H complexes. Although the H shallow donors can be neutralized at low temperatures to achieve p-type conductivity the incorporation of hydrogen atoms that act as shallow donors should be avoided.

[1] C. G. Van de Walle, Phys. Rev. Lett. **85**, 1012 (2000).
[2] D. M. Hofmann, Hofstaetter, A.,Leiter, F., Zhou, H., Henecker, F., Meyer, B. K., Orlinskii, S. B., Schmidt, J., Baranov, P. G., Phys. Rev. Lett. **88**, 045504 (2002).
[3] S. J. Jokela, McCluskey, M. D., Phys. Rev. B **72**, 113201 (2005).
[4] N. H. Nickel, phys. stat. sol (b) **243**, R51 (2006).

Corresponding author:
N. Nickel
nickel@hmi.de

Electrical detection of coherent ^{31}P spin quantum states in silicon

K. Lips[1], C. Boehme[1,2], A.R. Stegner[3], H. Huebl[3], M. Stutzmann[3], M.S. Brandt[3]
■ 1 HMI, SE1 ■ 2 University of Utah, Physics Department, Salt Lake City, Utah, USA
■ 3 Walter Schottky Institut, Technische Universität München, Garching, Germany

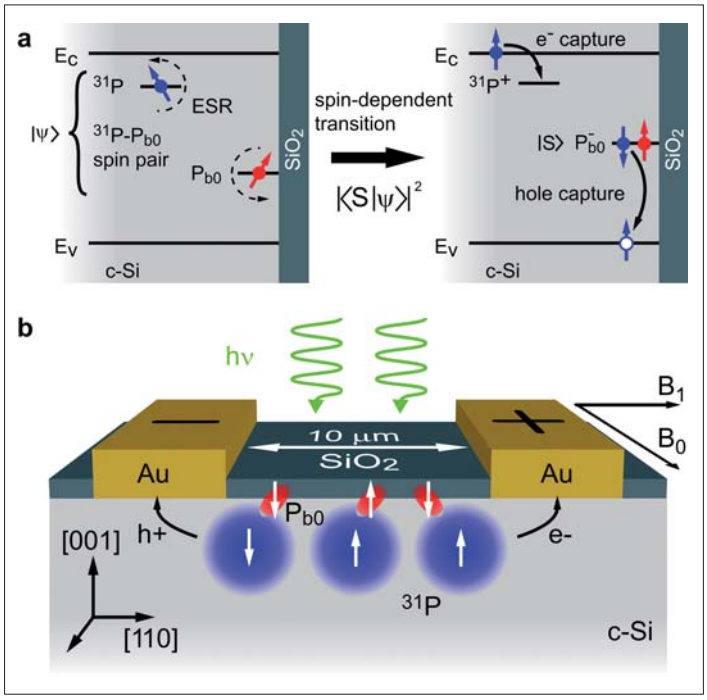

Fig. 1: Read-out scheme for ^{31}P electron spin qubits. (a) Sketch of the band diagram of the Si/SiO_2 interface and the spin-dependent process involving ^{31}P and P_{b0} states. (b) Sketch of the Si device used to demonstrate the electrical spin read out [4].

It is the insatiable demand of modern society for energy and information that has strongly promoted two fields of research that seem to be antipodal with respect to the physical requirements involved, namely photovoltaics (PV) and quantum computing (QC), respectively. Whereas in PV a high degree of separation of photo-generated charge is mandatory and not the conservation of coherence[1], the opposite holds for QC. In QCs, information is encoded in quantum states, so called qubits. These qubits are manipulated by a physical procedure that is determined by the mathematical problem that has to be solved. During these manipulations the qubit is not allowed to lose its quantum coherence until the final read-out process. In search of such ideal qubits, the proposal by Bruce Kane [1] of a silicon (Si) based QC where the qubits are formed by the nuclear spin of phosphorus donors (^{31}P) has brought the two research areas closer together due to their common material issues.

One of the key problems of Kane's original concept concerns the actual readout of the ^{31}P quantum state. For this a specific nuclear spin is encoded in the ^{31}P electron spin through hyperfine interaction. Since a single electron spin cannot be detected with common electron spin resonance (ESR) (lack in sensitivity by over 10 orders of magnitude), the realization of spin-to-charge transfer is the key prerequisite for a successful implementation of single spin phosphorus (^{31}P) readout devices, capable of determining the actual spin state (spin up $|\uparrow>$ or spin down $|\downarrow>$). Such a coherent spin-to-charge transfer was experimentally verified for the first time in thin-film silicon absorber layers at HMI using pulsed electrically detected magnetic resonance (pEDMR) [2] and a spin based qubit readout concept was proposed [3] and recently experimentally verified on a 15 nm thin layer of P-doped crystalline silicon (*c*-Si) (see Fig. 1b) [4]

Fig. 1(a) illustrates the readout scheme based on spin-dependent recombination in silicon. In order to probe ^{31}P electron spins, spin-dependent recombination through P_{b0} centers is used. P_{b0} centers are trivalent Si atoms at the $c\text{-}Si/SiO_2$ interface that introduce paramagnetic states in the Si band gap. If a neutral P_{b0} center is located in the vicinity of a ^{31}P donor, both their electrons can form a coupled spin pair. This spin pair can relax by a transfer of the electron from the ^{31}P to the P_{b0}, forming a negatively charged defect (P_{b0}^-). This transition probability depends strongly on the relative spin orientation of the two electrons of the pair. Since the spin configuration can be changed by ESR, the capture probability at the P_{b0} can be altered and hence the fingerprint of the paramagnetic states involved can be observed in the photocurrent.

[1] *Note that in a PV device charge separation of photo-generated states automatically destroys quantum coherence*

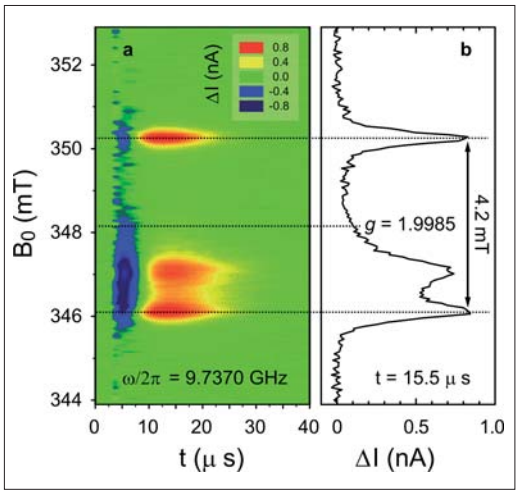

Fig. 2: (a) Contour plot of the photcurrent transient change induced by a short microwave burst at T=5K. (b) Intensity distribution taken at t = 15.5 μs showing the typical ^{31}P ESR fingerprint in the current [4].

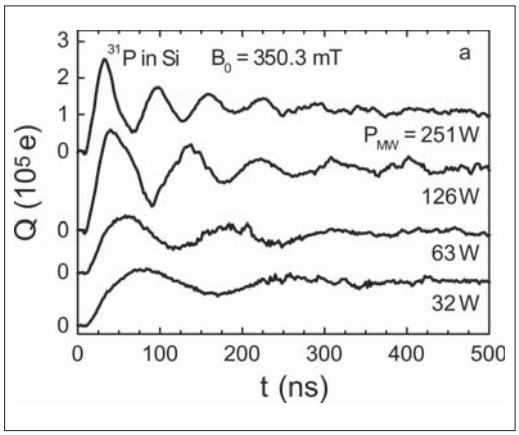

Fig. 3: Rabi oscillation observed at a magnetic field position of 350.3 mT (ESR resonance of ^{31}P) in Fig. 2b for various microwave powers. The Rabi frequency increases linearly with microwave field amplitude. Since the electron spins of ^{31}P and P_{b0} are in the triplet state (both spins parallel) before the ESR pulse is applied, the maximum of Q indicates $|\uparrow\rangle$ of ^{31}P, a minimum corresponds to $|\downarrow\rangle$.

Fig. 2a shows the change ΔI of the photocurrent as a function of time t after the ESR microwave pulse was turned off. The plot shows three resonances exhibiting identical dynamics. The intensity plot taken at t=15.5 μs as shown in Fig. 2b clearly shows two hyperfine split features separated by 4.2mT (g value 1.9985). This is the characteristic ESR fingerprint of the ^{31}P donor electron in Si. The two lines stem from the two spin orientations of the ^{31}P nuclear spin. The broader peak at 347.1mT originates from P_{b0} centres.

When the current behaviour is analysed on the same time scale (ns-scale) as the driving ESR microwave field induces Rabi oscillations between energy levels of the spin pairs, oscillations in the photocurrent are observed (Fig. 3). The fact that the oscillation frequency increases with increasing ESR microwave power indicates that the ^{31}P spin state can be detected coherently in the photocurrent. Rabi echo experiments (not shown) reveal that the fast decay of the Rabi oscillations in Fig. 3 is not due to incoherence but is caused by an inhomogeneous microwave field, which leads to a fast coherent dephasing of the spin ensemble. The true dephasing time was determined to be above 1μs.

The experiments have been carried out on ensembles of ^{31}P. The charge noise achieved so far is about 10^4 e resulting in a detection limit that is around 11 orders of magnitude lower than for conventional nuclear magnetic resonance and about 7 orders of magnitude lower than for ESR. The results shown are an important step towards the realization of an electrical spin readout of donors. The proof-of-principle experiments demonstrate a spin-to-charge transfer mechanism required for ^{31}P electron spin readout via ^{31}P–P_{b0} pairs and show that this spin pair is sufficiently weakly coupled so that the ^{31}P hyperfine interaction can be observed, ultimately allowing the electrical detection of the nuclear spin state. However, although inclusion of this readout scheme into a scalable architecture is in principle conceivable via local gates, electrostatically controlling the ^{31}P–P_{b0} coupling, there remain a variety of physical and technological issues to be solved before application of the readout scheme to quantum information processing.

[1] B. E. Kane, Nature **393** (1998) 133
[2] C. Boehme and K. Lips, Phys. Rev. Lett. **91** (2003) 246603
[3] C. Boehme and K. Lips, phys. stat. sol. (b) **233** (2002) 427
[4] A. R. Stegner, C. Boehme, H. Huebl, M. Stutzmann, K. Lips, and M. S. Brandt, Nature Physics **2** (2006) 835

Corresponding author:
K. Lips
lips@hmi.de

Stability of $CuInS_2$ Module Test Structures under Reverse Bias Stress

Ch. Köble[1], J. Klaer[2], R. Klenk[1]
■ 1 HMI, SE2 ■ 2 HMI, SE3

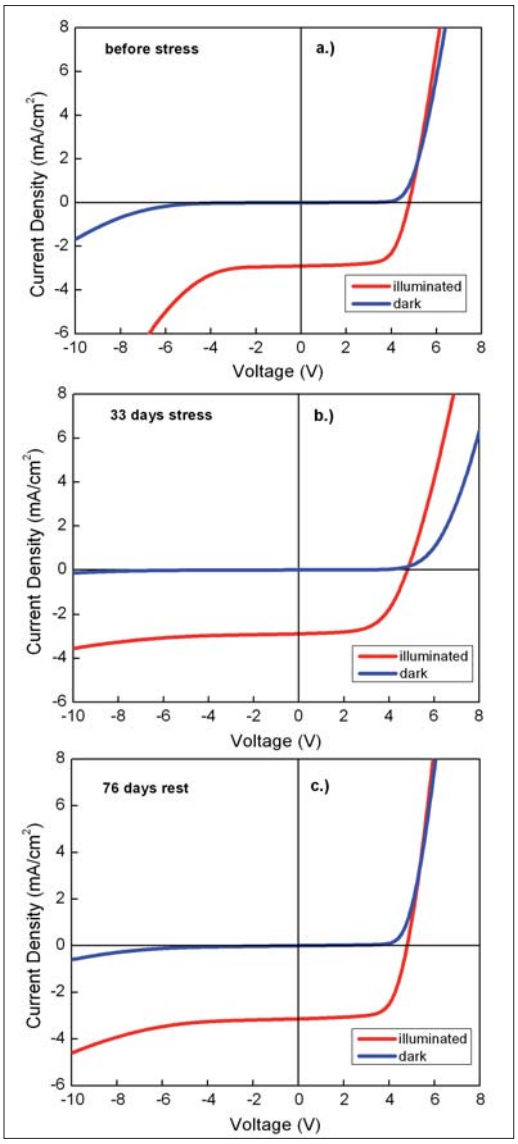

Fig. 1: Voltage-current curves of $CuInS_2$ module test structures (seven cells connected in series by monolithical integration). After 33 days of reverse-bias stress the rectification properties are enhanced but an apparent series resistance and a distinct cross-over have developed. In the following rest period the forward characteristics are fully restored confirming that there is no permanent damage has been caused.

Thin-film chalcopyrite-based modules are known to maintain a comparably high efficiency when partially shaded. This constitutes a significant advantage over conventional silicon modules and contributes to a high annually averaged output in terms of kWh/kWP even in difficult applications, e.g., building integration. During standard certification procedures (IEC 61646), such as the test for degradation under ultraviolet light, the module may also be illuminated inhomogeneously. Under any of these conditions, the cells that see little or no illumination are biased in reverse. In this work we have studied the stability of monolithically interconnected test structures (mini-modules) under such conditions. We find that prolonged current flow in reverse direction without illumination modifies the *jV*-curve of $CuInS_2$ mini-modules. Rectification properties are significantly enhanced. A degradation of the fill factor is observed immediately after the stress test but the fill factor eventually recovers completely. None of the investigated samples was irreversibly damaged. We conclude that $CuInS_2$ modules can be operated safely under partial illumination without the need for protection by bypass diodes.

In contrast to $Cu(In,Ga)Se_2$-based cells, typical $CuInS_2$-based devices show an illumination-dependent reverse breakthrough at relatively low voltages (Fig. 1). In principle this is advantageous because it minimizes the power consumed within a reverse-biased cell. During the stress period, the reverse breakthrough "flattens" as seen in Fig. 1, resulting in a substantial increase of the breakthrough voltage. This could imply that the efficiency $CuInS_2$ module under prolonged partial shading is not quite as high as previously assumed. The slope of the forward characteristics reduces due to an increasing apparent series resistance, resulting in lower fill factor. In addition we note a more pronounced cross-over between illuminated and dark *jV*-curves. The open circuit voltage of the mini-modules changed only slightly, and not in a systematic way. The photo current density stayed on the same level. In some cases we observed a spontaneous healing of shunts. After removing the reverse bias from the mini-modules, the samples were stored under un-

specified ambient conditions for recovery. During the recovery period the apparent series resistance diminishes relatively fast. This allows the forward characteristics to recover to the original shape and the fill factor to increase again. In all cases the module performance under illumination was eventually restored or even slightly exceeded the one determined before the experiment. The reverse breakthrough behaved somewhat different. In some cases the reverse characteristics continued the trend observed during the stress period before reversing eventually. In other cases the breakthrough voltage decreased right away, albeit with a very long time constant. Within these experiments we have not seen a single sample where the reverse breakthrough has returned to the original curve, not even after 7 months.

The apparent series resistance in forward direction and more distinct cross-over of dark and light *jV*-curves are clearly meta-stable effects as the fill factor recovers completely after removing the external bias. In some aspects similar observations have been reported by M. Igalson et al. for $Cu(In,Ga)Se_2$-based solar cells [1,2]. In their case the *jV* curve develops a kink or S-shape and the apparent series resistance observed here may be interpreted as a milder case of the same effect. The cross-over between light and dark *jV* is present in both cases. These non-linear effects were explained by deep acceptors close to the interface and a modification of their occupation probability under non-equilibrium conditions, in extension of a model described earlier by A. Niemegeers et al. [3]. Ionization of the acceptors results in a p^+ layer impeding the current flow. However, it is assumed for these models that there is a surface layer (ordered vacancy compound, OVC) with a band gap wider than that of the bulk material [4]. Consequently, there is a hole barrier in the valence band which decouples the deep acceptor states in this surface layer from the hole distribution in the chalcopyrite valence band. The non-linear effects in this model depend critically on the existence of such a hole barrier. It is at the moment unclear whether a hole barrier exists in $CuInS_2$ solar cells. On one hand, the material is prepared under copper excess and more or less lattice-matching OVC phases are not reported in the equilibrium phase diagram ($CuIn_5S_8$ has a completely different spinel structure). On the other hand the surface composition after chemical removal of the CuS segregations is reported to be deficient in copper and there are indications of at least a small widening of the surface band gap [5]. A more detailed investigation of the reverse-bias-induced effects could therefore be valuable in clarifying the band structure and recombination mechanisms of $CuInS_2$ cells in the vicinity of the interface. This is especially valid if a model can be formulated that describes both, modification of the current transport in reverse as well as in forward direction.

[1] M. Igalson, M. Bodegard, L. Stolt, Solar Energy Materials & Solar Cells **80** (2003) 195
[2] P. Zabierowski, U. Rau, M. Igalson, Thin Solid Films **387** (2001) 147
[3] A. Niemegeers, M. Burgelman, R. Herberholz, U. Rau, D. Hariskos, H.W. Schock, Progress in Photovoltaics **6** (1999) 407
[4] D. Schmid, M. Ruckh, F. Grunwald, H.W. Schock, J. Appl. Phys. **73** (1993) 2902
[5] L. Weinhardt, O. Fuchs, D. Groß, G. Storch, E. Umbach, N.G. Dhere, A.A. Kadam, S.S. Kulkarni, C. Heske, Appl. Phys. Lett. **86** (2005) 062109

Corresponding author:
R. Klenk
klenk@hmi.de

Replacing Indium in chalcopyrite-type thin film solar cells by abundant elements

I.M. Kötschau, A. Weber, S. Schorr, H.-W. Schock
■ HMI, SE3

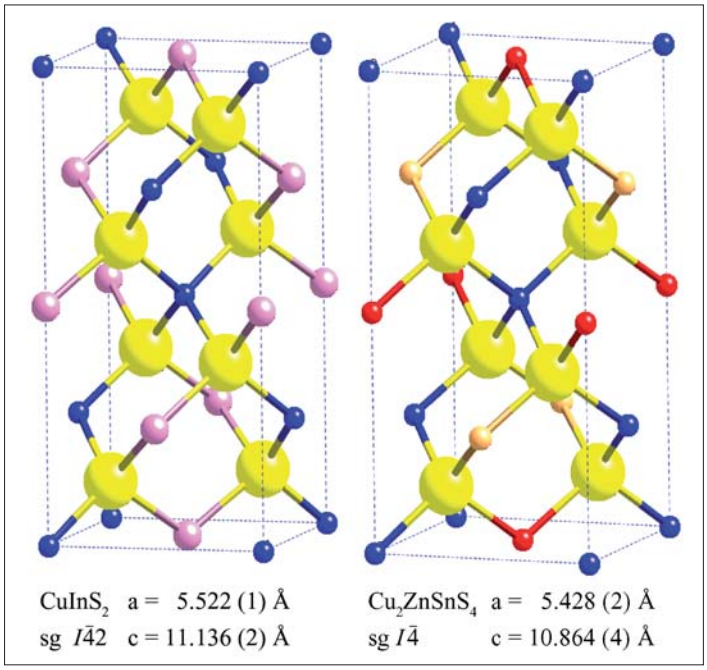

Fig. 1: Comparison of the chalcopyrite type (left) and the kesterite type (right) structure. Both structures show tetragonal symmetry but belong to different space groups (sg). (blue – Cu; pink – In; red – Sn; orange – Zn; yellow – S).

Highly efficient thin film solar cells based on compound semiconducting materials such as $Cu(In,Ga)Se_2$ show a current record efficiency of 19.5% on the laboratory scale [1]. Solar cells made of plain $CuInS_2$ have not reached these record efficiencies yet but are also of significant interest due to a number of advantages in comparison with the more widely investigated selenium containing chalcopyrites. Both, solar cells made of $Cu(In,Ga)Se_2$ as well as $CuInS_2$, are on the verge to large scale industrial production.

Since the availability of indium is an object of concern regarding the production on a gigawatt scale, its replacement by more abundant elements at similar efficiency is very desireable. An alternative compound for thin film solar cells is kesterite (Cu_2ZnSnS_4). This compound possesses promising characteristic optical properties with a band gap energy of about 1.5 eV and a large absorption coefficient in the order of 10^4 cm^{-1}. According to the literature the best conversion efficiency obtained with this compound is 5.45% [2]. The chalcopyrite type structure and the kesterite type structure are closely related but non-isotyp (Fig. 1). The main difference consists in a different cation ordering. Both obey tetragonal symmetry and can be foreseen as substitutional derivative ternaries of the cubic sphalerite type structure.

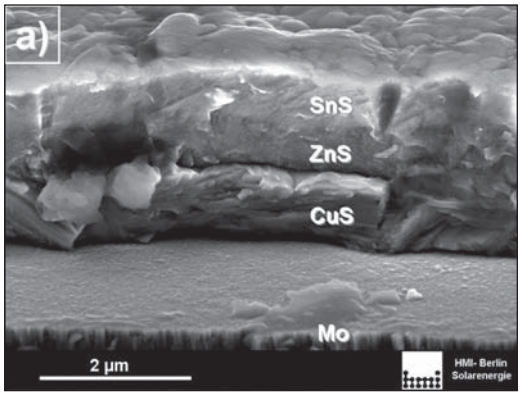

Fig. 2a: Precursor layer of the sequence Mo-CuS-ZnS-SnS (Cu-rich composition). The three layer stack is clearly visible.

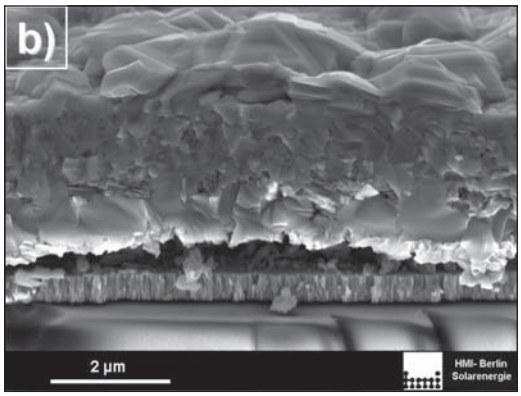

Fig. 2b: Precursor layer after processing according to program in Fig. 3. The copper sulphide (CuS) forms large crystallites on top of the film.

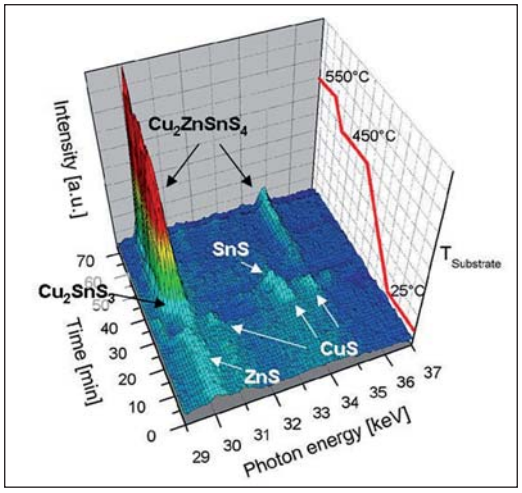

Fig 3: 3D-Plot of EDXRD data gathered during the annealing of the film depicted in Fig. 2b. Before reaching the first annealing period at 450°C most binary sulphides are consumed. At 30 keV the strong diffraction peak of the (densely packed) 112 lattice planes of Cu_2ZnSnS_4 appears. A shoulder of this peak can be assigned to Cu_2SnS_3 and disappears upon further heating to 550°C.

The absorber of the best thin film Cu_2ZnSnS_4 solar cell devices has been processed in two steps. At first a precursor stack with metallic layers or binary sulphides (ZnS, SnS etc.) is deposited by sputtering and evaporation techniques. In the second step the precursor is sulphurized under vacuum conditions at temperatures about 550°C [3]. However, the reactions during the crucial second step of this process have not been investigated yet. Therefore in-situ energy dispersive X-ray diffraction (EDXRD) has been applied to study the formation of Cu_2ZnSnS_4 thin films.

Precursors on Mo-coated glass substrates have been formed by sputtering and sulphurization of copper and subsequently evaporating ZnS and SnS. Different Cu/(Zn+Sn)-ratios and deposition sequences (CuS-ZnS-SnS and CuS-SnS-ZnS) have been investigated. A typical precursor is depicted in Fig. 2a.

The diffraction experiment is based on a process chamber designed for the energy dispersive x-ray beamline F3 at HASYLAB, Hamburg [4]. The setup consists of a pumping system giving base pressures of about 10^{-5} mbar in the chamber, a Knudsen cell for sulphur effusion and a sample holder with an integrated ceramic heater. A small polyimide window allows the white synchrotron radiation (meV-100keV at beamline F3) to enter the process chamber where it interacts with the sample. The scattered light is detected under a fixed angle 2θ of 7.2° by an energy dispersive detector in the range of 5 keV to 57 keV. The substrate temperature rises slowly from room temperature to annealing temperatures of 450°C and 550°C, while sulphur is continuously evaporated from the Knudsen cell to avoid sulphur deficiency in the thin film. Every 15 seconds a complete EDXRD spectrum is recorded which allows one to track the phase sequence in dependence of process time and temperature.

Fig. 3 shows a section of the sequentially recorded EDXRD spectra as a function of energy and time/temperature. The evaluation shows that in a first step (re)crystallisation of binary sulphides occurs. Upon further heating a transition $CuS \rightarrow Cu_{2-x}S$ and $Sn_2S_3 \rightarrow SnS$ can be detected and the formation of ternary Cu_2SnS_3 and quaternary Cu_2ZnSnS_4 starts. Reaching 550°C the Cu_2SnS_3-share diminishes and the spectra can be assigned to Cu_2ZnSnS_4 and $Cu_{2-x}S$ (Cu-rich composition). Figure 2b shows a cross sectional SEM image of the precursor stack after the sulphurization process. Large crystallites of CuS can be found on the surface, whereas the Cu_2ZnSnS_4-layer underneath appears still rather inhomogeneous with small crystallites. Nevertheless we found little impact of the metal ratio and stacking sequence on the reaction sequence and a strong tendency to form the kesterite structure in all studied cases. This is an encouraging result for the future exploratory investigation of the material as a photovoltaic absorber for thin film solar cell devices. Stepping further the study will be extended to the $2(CuInS_2)$-Cu_2ZnSnS_4 system, where the solid solution formation is based on the substitution $2In^{3+} \leftrightarrow Zn^{2+} + Sn^{4+}$. The results of these studies will provide a comprehensive knowledge about microscopic and kinetic aspects of the phase transformation and crystal growth in the Cu-(In/Zn,Sn)-S system. In parallel the results will be used to identify cost effective process pathways suitable and for large scale production processes.

[1] M. Contreras, M.Romero, R. Noufi, Thin Solid Films, **551-512**, p.51 (2006)
[2] H. Katagiri, K. Jimbo, K. Moriya, K. Tsuchida, Proc. 3rd WCPEC, p. 2874 (2003)
[3] H. Katagiri, Thin Solid Films, **480-481**, p.426 (2005)
[4] C. v.Klopmann, J. Djordjevic, R. Scheer, Journal of Crystal Growth, **289**, p. 113 (2006)

Corresponding author:
I. Kötschau
koetschau@hmi.de

Improved insight into the microstructure of chalcopyrite-type thin-film solar cells

D. Abou-Ras, M. Nichterwitz, J. Bundesmann, C.A. Kaufmann, S. Schorr, H.W. Schock
■ HMI, SE3

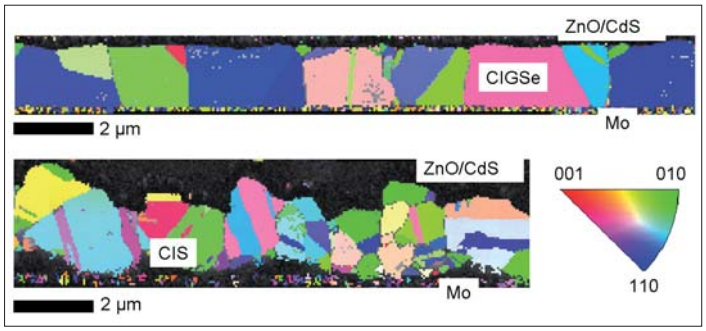

Fig. 1: EBSD maps from ZnO/CdS/CIGSe/Mo/glass (top) and ZnO/CdS/CIS/Mo/glass (bottom) stacks. The colors correspond to various cristallographic directions given by the legend (bottom, right), indicating the local orientations of the CIGSe and CIS thin films. Numerous twins are visible in the CIGSe and CIS layers.

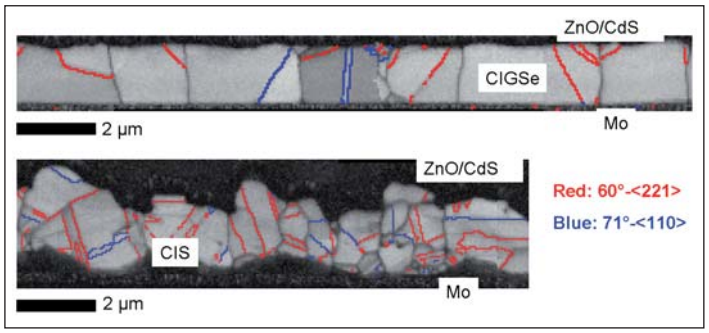

Fig. 2: EBSD maps from ZnO/CdS/CIGSe/Mo/glass (top) and ZnO/CdS/CIS/Mo/glass (bottom) stacks in band contrast (the same sections as shown in Fig. 1). 60°-<221> twins (red) and 71°-<110> boundaries (blue) are highlighted.

In research and development of chalcopyrite-type thin-film solar cells, such as, e.g., those based on $Cu(In,Ga)Se_2$ (CIGSe) – grown by coevaporation of the elements [1] – and $CuInS_2$ (CIS) – grown by rapid-thermal annealing [2] –, it is essential to analyze the effect of parameter variations (e.g. deposition temperature or composition) on the microstructure of the absorber and to compare this information with the solar-cell performance. Electron-backscatter diffraction (EBSD) represents a powerful technique to determine grain sizes, grain orientations and grain boundaries in polycrystalline materials, providing high precision and good statistics. The information gathered on the microstructure in the thin films is of much higher quality than that of, e.g., „apparent" grain sizes from scanning electron micrographs. Since the current conduction in a thin-film solar cell proceeds perpendicular to the surface, it is important to study the microstructures of chalcopyrite-type thin films in cross-section in order to resolve possible effects of grain sizes and grain boundaries on the electrical properties of the solar cells.

For the first time, EBSD studies have been conducted on polished cross-sections of CIGSe and CIS thin-film solar cells. The EBSD maps shown in Fig. 1 were acquired using a point-to-point distance of 50 nm. The microstructures of the CIGSe and CIS thin films are well resolved. The difference in grain size of both layers is apparent. Numerous twins are visible in both layers, formed probably during growth or during the cool-down phase after the deposition.

The nature of the grain boundaries was determined with high precision. The most frequent types of grain boundaries found in CIGSe and CIS thin films are 60°-<221> and 71°-<110> twin boundaries. Both grain-boundary types have a Σ value of 3, which can in general be attributed to lowest grain-boundary energies. In Fig. 2, EBSD maps from ZnO/CdS/CIGSe/Mo/glass (top) and ZnO/CdS/CIS/Mo/glass (bottom) stacks in band contrast are shown with 60°-<221> (red) and 71°-<110> twin boundaries (blue) highlighted.

The rotation transformations characterized by 60°-<221> and 71°-<110> transform certain {112} crystal planes to other {112} planes (e.g., (112) to (112)); i.e., the most grain boundaries in CIGSe and CIS thin films are coherent or quasi-coherent along {112} planes. This fact can be related directly to the importance of {112} planes for the topotactical growth of $CuInS_2$ and $Cu(In,Ga)Se_2$ thin films.

Apart from local orientations and grain boundaries, also grain sizes can be determined with high precision. It was found that all grain-size distributions from CIGSe and CIS thin films are rep-

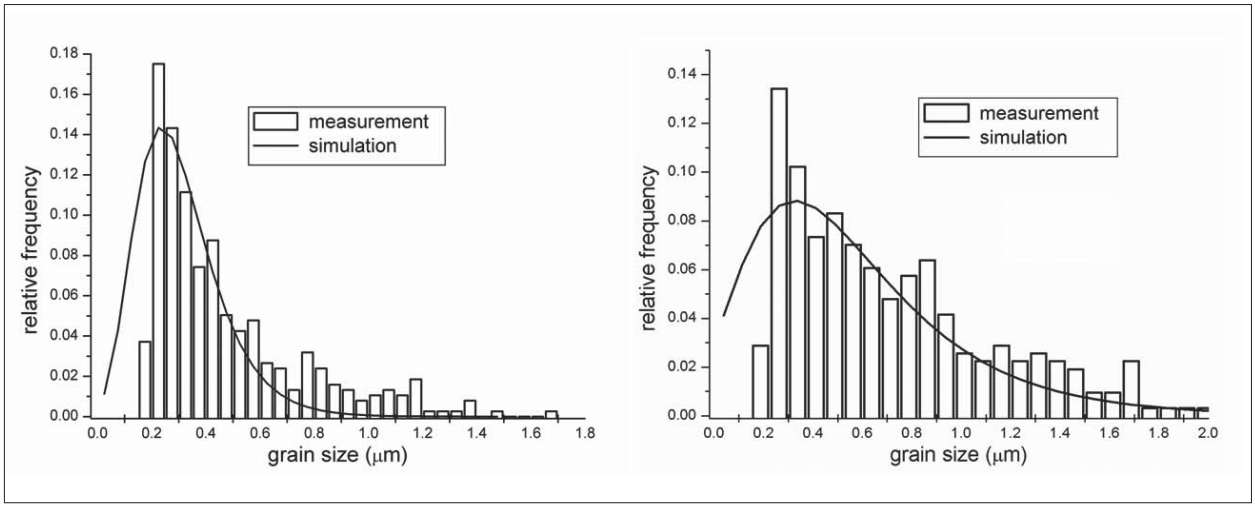

Fig. 3: Grain-size distributions of CIGSe (left) and CIS (right) thin-film absorbers in completed solar cells. The measured grain sizes (bars) can be represented well by lognormal distributions (solid lines).

resented well by lognormal-distribution functions (Fig. 3). According to literature, lognormally distributed grain sizes are typical for surface-controlled growth - the growth mechanism broadly accepted for the CIGSe and CIS thin films studied in the present work.

In conclusion, a detailed study of the microstructure of CIGSe and CIS thin-film solar cells with high precision and good statistics was performed for the first time, acquiring EBSD maps on cross-section samples. The most frequent grain boundaries were identified, and the importance of {112} planes during the topotactical growth of the thin films was revealed. Furthermore, grain-size distributions from CIGSe and CIS thin films can be related to the surface-controlled growth of these layers.

The authors would like to thank Peter Schubert-Bischoff (SF1) and Ulli Bloeck (SE4/SF3) for the help with the sample preparation.

[1] C.A. Kaufmann, T. Unold, D. Abou-Ras, J. Bundesmann, A. Neisser, R. Klenk, R. Scheer, K. Sakurai, H.-W. Schock, Thin Solid Films, to be published, doi:10.1016/j.tsf.2006.12.095.
[2] J. Klaer, R. Klenk, D. Abou-Ras, R. Scheer, H.W. Schock, D. Schmid, W. Eisele, J. Hinze, I. Luck, C.v. Klopmann, A. Meeder, U. Rühle, N. Meyer, Proceedings of the 21st European Photovoltaic Solar Energy Conference and Exhibition, Dresden, Germany, September 4-8, 2006, pp.1801-1805.
[3] D. Abou-Ras, S. Schorr, H.W. Schock, submitted.

Corresponding author:
D. Abou-Ras
daniel.abou-ras@hmi.de

InGaAsP/InGaAs double junction solar cells

U. Seidel, B.E. Sağol, K. Schwarzburg, T. Hannappel
HMI, SE4

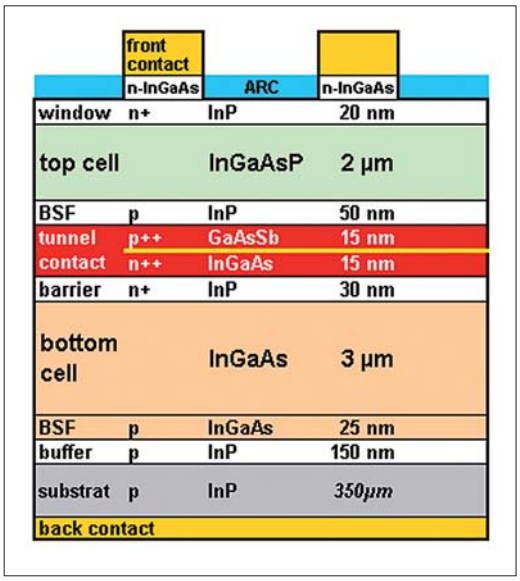

Fig. 1: Layer structure of the MOVPE-grown low bandgap double junction solar cell. For the serial connection of the bottom cell (InGaAs) and the top cell (InGaAsP) a tunnel diode, made up of n-InGaAs and p-GaAsSb, was used.

Recently, multi-junction III-V solar cells in the form of a triple junction cell grown on a germanium crystal have exceeded the 40% conversion efficiency barrier [1]. Even higher values can be achieved [2], if more than three appropriate subcells were realized with optimized band gaps. Theoretical calculations show, that a band gap E_{gap} in the range of 1eV is highly desirable for solar cells with multiple junctions. The idea of an InGaAsP/InGaAs tandem solar cell with low band gaps is to replace the bottom Ge sub-cell of the world record cell by a more efficient double junction bottom cell, and to combine the top and bottom tandem cells by means of mechanical stacking, wafer bonding, or separation of the solar spectrum.

For this purpose, we prepared InGaAsP/InGaAs tandem solar cells monolithically on p-InP(100) in our Aixtron MOVPE reactor (AIX-200), using non-gaseous precursors that are less toxic than the conventional gaseous precursors. As shown in Fig.1 the serial connection between the InGaAs bottom cell (E_{gap} = 0.75eV) and the InGaAsP top cell (E_{gap} = 1.1eV) was realized by an Esaki-diode-like tunneling junction including thin layers of highly n-doped InGaAs and highly p-doped GaAsSb. This asymmetric material combination was used because of their favorable band offsets. For achieving the best performance of the tunnel diode and the solar cell, the interface between the n-InGaAs and p-GaAsSb layers has to be as sharp as possible. Therefore, the influence of different preparation procedures on the InGaAs/GaAsSb-interface was investigated in detail by optical in-situ spectroscopy, i.e. reflectance difference/anisotropy spectroscopy (RDS/RAS). These in-situ signals were benchmarked via a contamination-free transfer from MOCVD to UHV and surface science tools like low energy electron diffraction (LEED) and photoelectron spectroscopy (XPS/UPS).

A sharper InGaAs/GaAsSb-interface was achieved, if the growth of the GaAsSb layer was performed on an InGa-rich surface reconstruc-

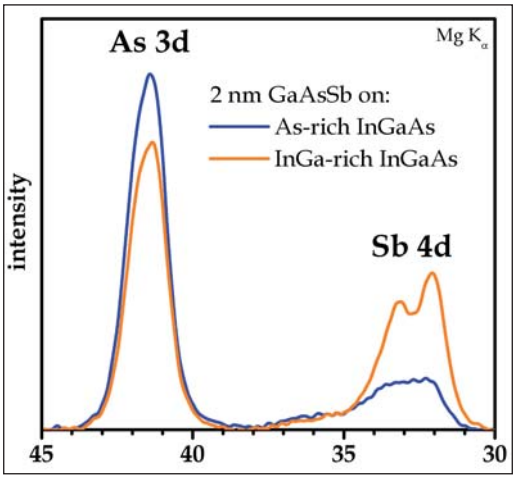

Fig. 2: As 3d and Sb 4d core levels, measured with XPS on 2nm GaAsSb, grown on As-rich (blue) and on InGa-rich (orange) InGaAs surface. The growth on the InGa-rich InGaAs surface leads to more Sb in the GaAsSb layer.

tion. Starting on As-rich InGaAs resulted in a much less Sb content within the first monolayers of the GaAsSb layer, which was detected by XPS (see Fig.2). Analysis of the Sb 4d and the As 3d core level peak areas revealed, that the Sb to As ratio was more than three times higher for the GaAsSb grown on InGa-rich InGaAs, than for the GaAsSb grown on As-rich InGaAs [4]. Direct comparison of these results to a standard As-rich GaAsSb surface [5] showed that the Sb to As ratio of the III-rich interface preparation was much more suitable than the V-rich preparation.
I-V curves of InGaAsP/InGaAs low band gap double junction solar cells are shown in Fig.3. I-V measurements were performed with the in-house solar simulator (SE2). It shows the characteristics under full AM1.5g spectrum (blue curve) and additionally the response to the filtered AM1.5g illumination (red curve). For the filtered measurement a RG850 (Schott) filter was used for simulating the illumination conditions for the operation of the double junction solar cell below a GaAs-based top cell. An open circuit voltage of 840 mV, a short circuit current density of 12.1 mA/cm^2, a fill factor of 73% and a solar conversion efficiency of 7.3% were obtained without an antireflection coating (ARC).

If this efficiency value is compared with the 4.6% of efficiency, which had been achieved with a germanium sub-cell employed in such a high efficiency triple-junction solar cell (GaInP/GaInAs/Ge) [6], the potential of the InGaAsP/InGaAs double junction solar cells is obvious. By the optimization of the absorber layer thickness and the AR-coating, an improvement of the efficiency for filtered sunlight to around 10% should be possible. In combination with a GaAs-based high bandgap multi-junction solar cell, a total conversion efficiency around 45% could be achievable.

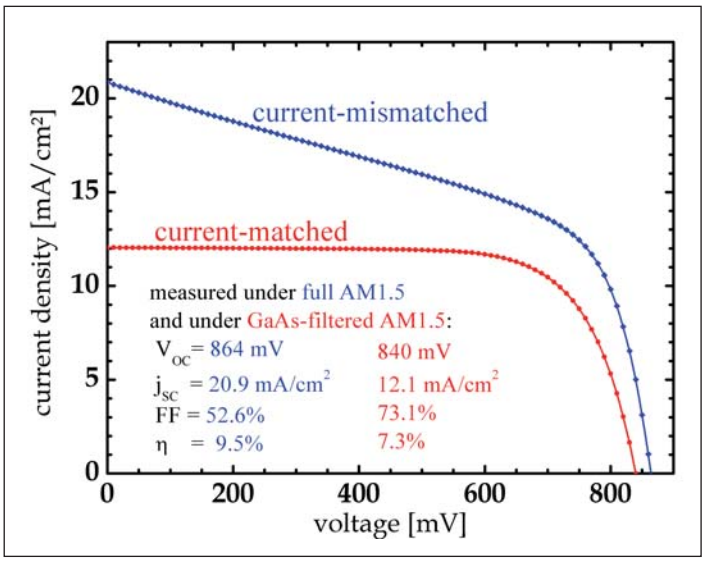

Fig. 3: I-V characteristic of an InGaAs/InGaAsP double junction solar cell measured under a full (blue curve) and a RG850-filtered (red curve) / spectrum.

[1] http://compoundsemiconductor.net/articles/news/10/12/5/1
[2] A. Marti, G.L. Araujo, Solar Energy Materials and Solar Cells **43** (1996) 203
[3] F. Dimroth, C. Baur, A.W. Bett, K. Volz, W. Stolz, Journal of Crystal Growth **272** (2004) 726
[4] U. Seidel, H.-J. Schimper, Z. Kollonitsch, K. Möller, K. Schwarzburg, T. Hannappel, J. Cryst. Growth **298** (2007) 777-781
[5] Z. Kollonitsch, H.-J. Schimper, U. Seidel, K. Möller, S. Neumann, F.-J. Tegude, F. Willig, T. Hannappel, J. Crystal Growth **287** (2006) 536-540
[6] C. Baur, M. Meusel, F. Dimroth, A. W. Bett, Conference Record of the 31st IEEE PV Specialists Conf., IEEE, Piscataway, NJ, USA 2005 675

Corresponding author:
T. Hannappel
hannappel@hmi.de

Electrical Response of Wet Chemically Grown ZnO Nanorods for Photovoltaic Applications

J. Tornow[1], K. Ellmer[2], K. Schwarzburg[1]
■ 1 HMI SE4 ■ 2 HMI SE5

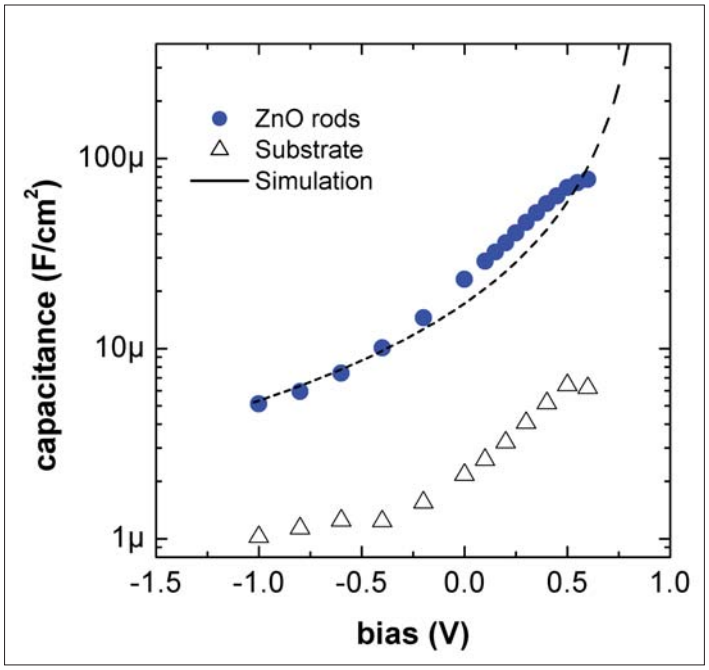

Fig. 1: Bias dependent capacitance of a nanorod electrode (filled circles) and the substrate alone (open triangles).

Vertically aligned ZnO nanorods were reported recently as an alternative oxide substrate for a dye sensitized solar cell (DSSC) [1] and for solar cells with extremely thin solid state absorbers [2]. Replacing the network of TiO_2 nano colloids in standard DSSC is expected to bring improvements in charge carrier transport due to the much higher electron diffusion coefficient of ZnO. The open rod structure gives a much greater flexibility in deposition processes for the application in a ultra thin absorber solar cells. ZnO nanorod electrodes can be grown by several methods ranging from gas phase epitaxy on patterned substrates that gives nearly perfectly aligned periodic structures to low cost methods like chemical bath deposition. We have prepared Zinc oxide nanorod electrodes by covering a fluorine doped tin oxide glass substrate with a compact layer of sputtered ZnO and subsequently placing this substrate in an aqueous solution containing $Zn(NO3)_2$ (0.01M) and NaOH (0.36M) at 80°C. Using different growth times of 5 to 120 minutes resulted in rod lengths of less than 0.5µm up to more than 2 µm with typical rod diameters ranging from 10 nm to 200 nm. Samples were post annealed at 450°C for one hour. First experiments indicate that these electrodes are indeed a very promising candidate for ultra thin absorber solar cells with respect to inner geometry (aspect ratio~10-20), scalability and potential costs. Knowledge about electronic properties of the ZnO nanorod material and electrical behavior in test devices is essential for the successful development of such solar cells. We have carried out extensive electrical measurements and simulations to better understand in particular the role of the geometry on the electrical response. An easy method to measure the electrical responce of the ZnO nanorod electrodes is to employ them in a dye sensitized solar cell configuration [1]. By measuring stationary currents, impedance and photocurrent transients of such DSSC test devices it turned out, that the ZnO nanorod electrode contributes a capacitive component to the electrical response of the cell. Compared to most other solar cells the full frequency (0-10MHz) and time response (t>5ns) is rather complicated but can be modeled very well by making reasonable assumptions. The cause for the complicated response is the large capacitance of around $10uFcm^{-2}$ for a ZnO electrode with an aspect ratio of ~10. The low impedance of the ZnO electrode makes the cell response sensitive to other low impedance elements in the cell, in particular the counter electrode in the DSSC configuration. Nevertheless, by studying the bias dependency of the impedance response or the photocurrent response under varying amounts of additional series resistors, the ZnO capacitance could be identified.

Fig.1 shows the bias dependency of the ZnO capacitance extracted from an impedance measurement. The measured capacitance scales linearly with the length of the nanorods (not shown

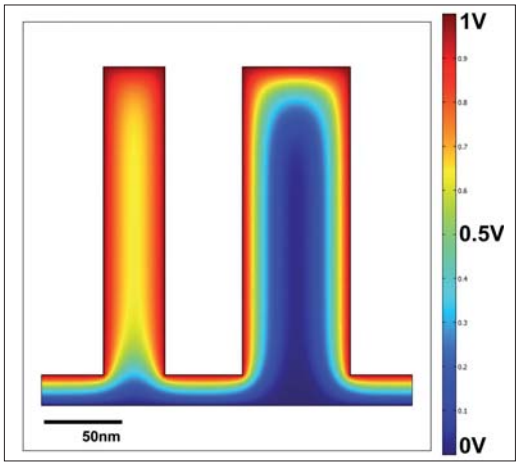

Fig. 2: Simulated potential distribution in a thin (40 nm) and a thick (80 nm) nanorod at 1V voltage drop across the interface for a charge carrier concentration of $10^{18}cm^{-3}$.

here). While the overall transient response of the cells is almost as slow as in genuine Grätzel cells using the nanoporous TiO_2 substrate, it is not related to a slow electron transport in the ZnO but rather to the stationary electron distribution in the ZnO. The latter is evident by considering that the ZnO rods could be modeled with a static capacitance and by considering the bias- and rod-length dependencies of the capacitance values. It is instructive to visualize the distribution of the electrical potential in a nanorod. Fig.2 shows a FEM simulation of the potential distribution for thin and thicker rods with an electron concentration of $10^{18}cm^{-3}$ at 1V potential drop between the substrate and the rod. The potential drop inside the 40 nm thin rod is small and corresponds to a very low electron concentration. This almost field free situation is the accepted scenario for the colloid based DSSC solar cell. Since the assumed intrinsic electron concentration is rather high, an increase in the rod diameter to 80 nm already establishes a depletion layer inside the rod. The electron concentration in the middle of the rod is close to the intrinsic value ($10^{18}cm^{-3}$). Clearly, from the measurements (Fig.1) we can conclude that this is also the case for at least the majority of thicker rods in our electrodes. By calculating the carrier distribution at various potentials one can construct a plot of the rod capacitance vs. the voltage bias. A carrier density of around $10^{19}cm^{-3}$ and an average rod diameter of 80 nm gave a rough fit to the data (Fig.1 ‚simulation'). Depending on the actual values, the typical rod diameters of 10 – 100nm and carrier densities of $10^{17}cm^{-3}$ – $10^{19}cm^{-3}$ for ZnO rods can easily produce either the ‚fully depleted' or the ‚depletion layer' case. It is not yet clear which one of the 2 cases is favorable for a nanorod solar cell. This will depend on several factors such as the magnitude of tunneling currents and needs to be studied further both theoretically and experimentally.

[1] M. Law, L. Greene, J. Johnson, R. Saykally, P. Yang, Nature Materials **4** (2005) 455-459.
[2] C. Levy-Clement, R. Tena-Zaera, M. Ryan, A. Katty, G. Hodes, Advanced Materials **17** (2005) 1512-1515.

Corresponding author:
K. Schwarzburg
schwarzburg@hmi.de

Preparation and analysis of III-V on Si(100) growth

T. Bork, T. Hannappel
■ HMI, SE4

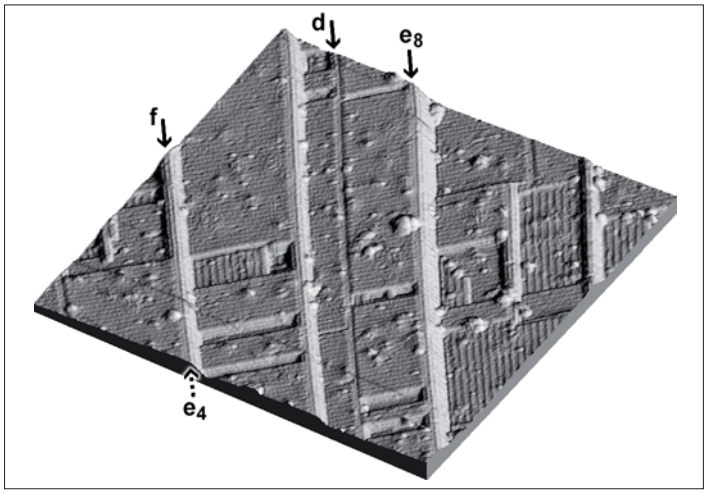

Fig 1: This surface was annealed at 725°C under 42 mtorr AsH_3. '5-7-5' line structures partially relieve tensile stress generated by As-As dimers. Four representative structures have been labeled (corresponding to Figure 2). Shallow craters form where AsH_3-etching of a terrace converts a step into a ridge (‚e4' into ‚f', for example). The subscripts ‚4' and ‚8' indicate step height in monolayers (1 ML = 1.36 Å).

For various applications of III/V-based devices and for the integration with the mature silicon (Si)-technology, the successful hetero-epitaxial growth of III–V films on Si(100) substrates are a prerequisite. High-efficiency multijunction solar cells on Si for example have long been a goal of researchers in the field of photovoltaics. Here, different stages of the III-V nucleation occurring during the metamorphic growth of InP on Si(100) surfaces were studied. The arsenic terminated Si(100) (As:Si(100)) surface is the standard starting point of most state-of-the-art III/V on Si growth procedures, even for III/V compounds that do not contain As. Hence, the As:Si(100) surface has been investigated as a possible substrate for the integration of III–V devices with Si-based technologies. As:Si(100) surface structures were observed with surface sensitive tools like scanning tunneling microscopy (STM), low-energy electron diffraction (LEED), reflectance difference/anisotropy spectroscopy (RDS/RAS), and photoemission (PES) after preparation of the As:Si(100) surface with metal organic chemical-vapour-deposition (MOCVD). The thus emerging As:Si(100) surface structure is completely different compared to the surface structure developing via preparation in ultra-high-vacuum (UHV) with molecular beam epitaxy (MBE) [1].

Various preparation procedures of the initial III-V on Si(100) nucleation were applied, in-situ monitored via RDS, and benchmarked in UHV employing a contamination-free MOCVD to UHV transfer system [2]. For the first time, tertiarybutylarsine was employed as non-gaseous, much less-toxic precursor compared to arsine to prepare clean arsenic-terminated Si(100). Cleaning of the surface and deoxidation occurred at temperatures of around 900°C, which is significantly lower than it is known for UHV (MBE) preparation [3]. The thickness of the passivating As-termination was about one atomic monolayer. Even and odd-numbered atomic steps occurred on the surface always resulting in a (2x1)/(1x2) two-domain surface (Fig.1). The domain structure of the Si(100) surface was independent from the angle and the degree of the misorientation, also including exactly oriented Si(100).

Different, non-bulk-like double row structures were observed on the As-terminated Si(100) surface via STM. These double row structures have been modeled and described theoretically as so-called '5-7-5' atomic ring structures at the National Renewable Energy Lab by McMahon et al. [4], where concomitant studies have been performed in collaboration in perfect agreement. In these studies, an entire family of trenches, ridges and steps on the nanometre-scale has been observed on TBAs- and AsH_3-exposed Si(100) (Fig. 2). These atomic ring structures do not appear on Si(100) surfaces treated with pure arsenic. They are energetically favorable compared to MBE-prepared bulk-like steps and flat surfaces and occur at steps, trenches, and ridges. These lines are very long and straight, and could potentially serve as templates for nanowires. Theoretical modelling showed that they are all built around a stress-relieving '5-7-5'- ringed atomic structure in which two 5-atom rings bracket a central 7-atom ring (Fig.2). '5-7-5' line structures

partially relieve tensile surface stress generated by As-As dimers. MOCVD-sample preparation was particularly favourable for the formation of '5-7-5' structures. The most reasonable explanation is that AsH_3 decomposition at the surface releases atomic H, which converts Si into SiH_4. Atomic H released by AsH_3 decomposition also explains why the Si deoxidisation temperature can be lowered significantly below 900°C in an TBAs or AsH_3 flux [3]. No modelling was ever done, because no model existing at the time fit with experimental observations. Here, the energetic stability of '5-7-5' structures, structures ‚a', ‚b', ‚d', and ‚e' of Fig. 2, were modelled theoretically using the Plane-Wave Pseudopotential Method with projector-augmented waves [4].

In-situ reflectance difference (RD) spectroscopy signals taken of the As-terminated Si(100) surface showed the same fingerprint as single-domain, (2x1)-reconstructed surfaces obtained in UHV via MBE by Kipp et al.[5], although LEED images of samples prepared in this work displayed a (2x1)/(1x2) two-domain surface. For the first time, temperature-resolved RD spectra down to 20 K were measured and did not show any energetic shift of the RDS peaks [6]. Thus, the origin of the RD spectra appears to be different from the attribution made by Kipp et al. in their theoretical calculations, i. e. electron phonon interaction and reduced lattice vibration [6].

On the two-domain, As-terminated Si(100) surface a 40 nm InP nucleation layer and, finally, a >1 µm P-rich state-of-the-art InP film was grown that displayed a (2x1), single-domain structure [6]. AFM displayed that the nucleation layer was formed by about 20-400 nm crystallites with orientations parallel to the crystal axis. The defect density of the InP film was dependent on the size of these crystallites. For the first time, the entire growth process was monitored with in-situ RDS [6].

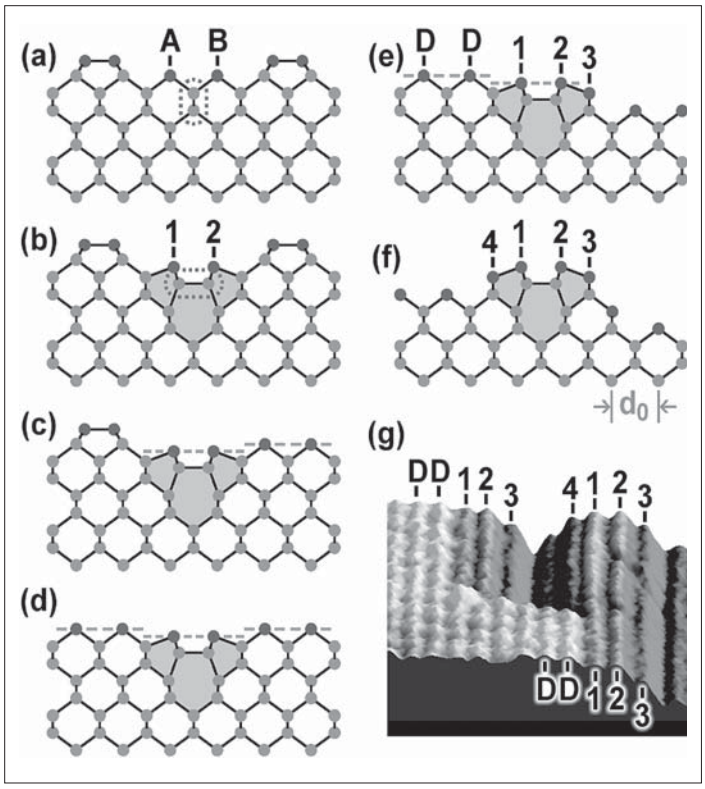

Fig. 2: Structures ‚a' -‚f': (a) Bulk-like type-A trench, (b) '5-7-5' type-A trench, (c) '5-7-5' 1-ML type-A step, (d) '5-7-5' type-B trench, (e) '5-7-5' type-B step, and (f) '5-7-5' ridge. As-As dimer bonds on the left-side terrace are either perpendicular (type 'A') or parallel (type 'B') to the line structure. All surface atoms are triply-bonded As (dark gray). All sub-surface atoms are quadruply-bonded Si (light gray). (g) STM image, artificially illuminated from the right. Continuity of a '5-7-5' core structure is seen where AsH_3-etching of the upper terrace has converted part of a type-B step into a ridge. To better show height differences, the ratio of height to width has been increased by 72%. V_{sample} = -2.5 V, I_{tun} = 0.04 nA.

[1] T. Bork, W.E. McMahon, J.M. Olson, T. Hannappel, J. Cryst. Growth **298** (2007) 54
[2] T. Hannappel, S. Visbeck, L. Töben, F. Willig, Rev. Sci. Instrum. **75** (2004) 1297.
[3] T. Hannappel, W.E. McMahon, J.M. Olson, J. Cryst. Growth **272** (2004) 24
[4] W.E. McMahon, Iskander G. Batyrev, T. Hannappel, J.M. Olson, S.B. Zhang, Phys. Rev. B **74** (2006) 033304
[5] L. Kipp, D.K. Biegelsen, J.E. Northrup, L.-E. Swartz, R.D. Bringans, Phys. Rev. Lett. **76** (1996) 2810.
[6] T. Bork, PhD theses (2006) HU Berlin

Corresponding author:
T. Hannappel
hannappel@hmi.de

Fractal Photocorrosion of Silicon

M. Lublow and H.J. Lewerenz
■ HMI SE5

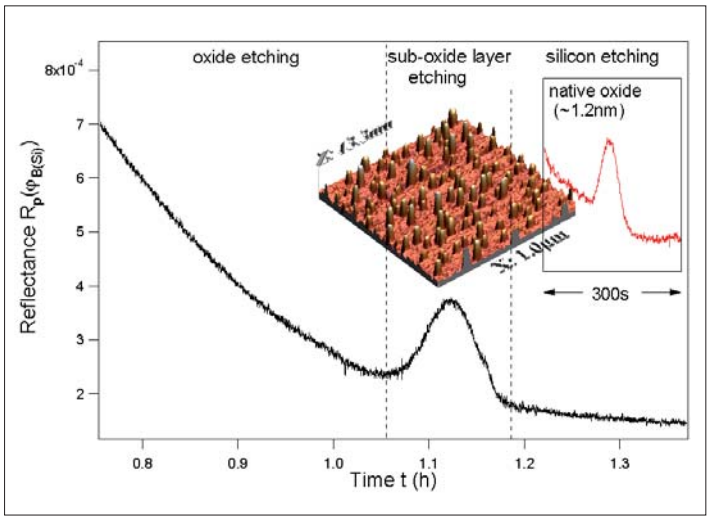

Fig. 1: Time dependence of the in-situ reflectance of thermally oxidized Si(111) at the bulk Brewster angle for λ=500nm (photon energy 2.48eV) in 40% NH_4F at open circuit potential. Inset: corresponding curve for native silicon oxide and AFM image of reaction products sticking to the surface during fast sublayer etching.

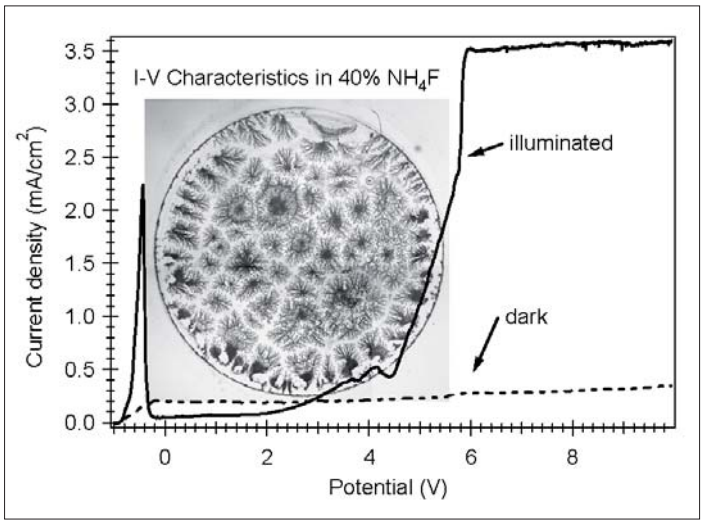

Fig. 2: Photocurrent-voltage curve for n-Si(111) in 40% NH_4F, pH~8; light intensity 5mWcm^{-2}; scan rate 10mVs^{-1}; potential vs. Ag/AgCl electrode. Inset: micrograph of the sample (diameter 0.8 cm) after electrochemical treatment.

Fractal patterns are wide spread in nature and occur when a perpetual (or abrupt) driving force interferes with obstacles that hinder unlimited forward-moving. Splitting and fractioning of the motion is then a strategy to overcome the boundaries while the process as a whole starts to exhibit recurring geometrical shapes [1]. Self-similarity and periodicity of these patterns turn out to be a possible consequence and are more than of pure mathematical interest. Diffusion phenomena along liquid interfaces, crystalline- or plant growth, dielectric breakdown effects, the ramifying structures of blood or pulmonary vessels, or even fluctuations in economical systems are examples for and accessible to the methods of fractal mathematics. As for silicon, many processes have already been discussed in terms of fractal analysis: surface roughening phenomena, the formation of porous silicon, or pattern recurrence during (electro-) deposition [2-4]. Recently, unusual anisotropic etching effects were observed while studying the morphological change of the silicon oxide/silicon interface during anodic polarization in concentrated ammonium fluoride. Depending on the process parameters, either etch grooves, following the formation mechanism of Diffusion Limited Aggregation (DLA) theory [5], or microfacet ensembles of high symmetry were produced (see below). As a possible application, fractal microfacet formation suggests an alternative route for (photo-) lithography techniques in the field of Microelectromechanical Systems (MEMS) and High Aspect Ratio (HAR) micromachining due to its inherent self-organization principle.

It is well known that crystalline silicon can be prepared atomically smooth using concentrated ammoniumfluoride solutions [6]. The treatment leaves a surface that exhibits single step atomic terraces and, on (111) surfaces, an H(1x1) lattice termination. Recently, we found in Brewster angle analysis of the etching behaviour of thin and ultrathin silicon oxides that a transitory regime with an enhanced etch rate exists [7]. This effect can be related to the roughening and fast dissolution of a strained layer underneath the silicon/silicon oxide interface that contains further suboxides [8]. For etching of a thermal oxide (18.2 nm thickness), for instance, the dissolution of this sublayer commences after 60 minutes exposure and its duration can reach 6 minutes (see Fig.1).

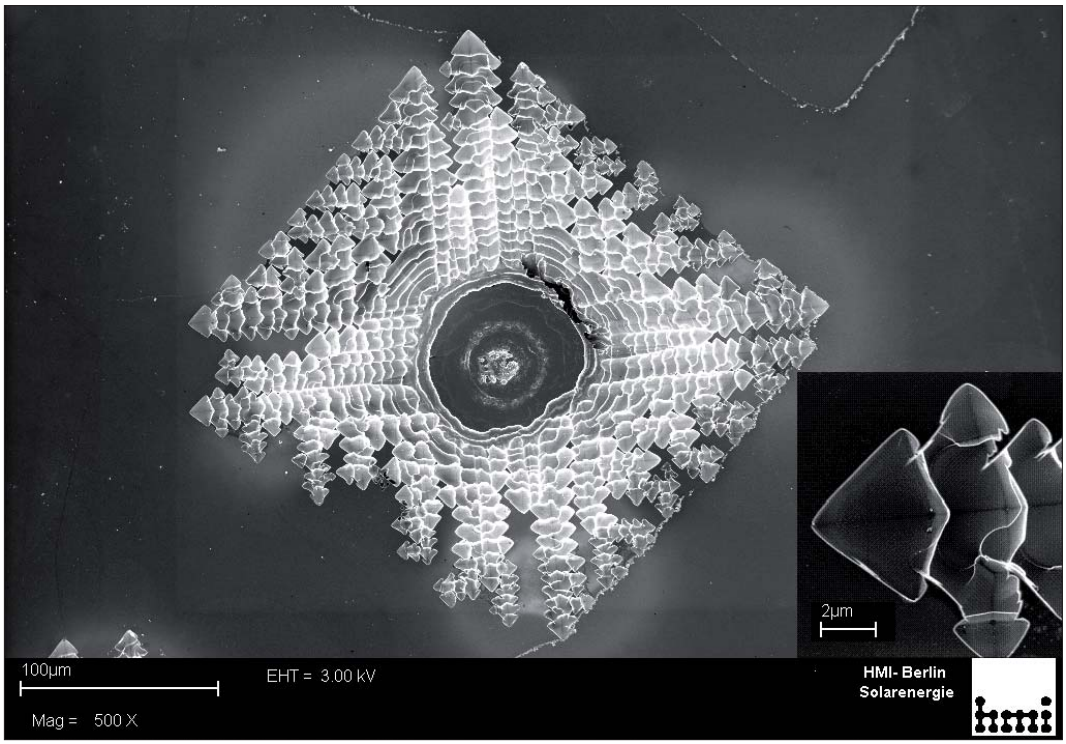

Fig. 3: HR-SEM image of a Si(100) surface after 10 min in 40% NH_4F at 6V; light intensity 7.5mWcm^{-2}. Inset: magnification of (111)-microfacets.

Whereas the surface topography associated with the OCP (open circuit potential) etching shows statistical roughening, a drastically different behaviour was found when the n-silicon electrode is anodically polarized and illuminated: in the plateau range shown in Fig.2, reaching from 5.5V-10V, novel unexpected structures are found that are obviously correlated to the underlying crystal geometry. Figs.3 and 4 show HRSEM images of photocorroded (100) and (111) surfaces after 10 min treatment in the electrolyte. From a circular and nearly unetched area in the center, ramifying etch grooves were initially formed. Enhanced three-dimensional anistotropic etching exposed low-index planes which are assumed to point towards <111> - direction for the Si(100) sample. A more complex ensemble of facets was found on Si(111) samples (Fig. 4). The overall structure reflects the Bravais-geometry of the respective crystal surfaces, i.e. the square and hexagonal lattice structure, respectively. In Fig.5, a profilometric image of a corroded (100) surface is displayed. The grooves have an almost uniform depth of ~6µm. Three-dimensional etching has not yet finished to expose the (111)-facets.

Preliminary element analysis by EDX shows silicon oxide and fluoride signals on the surface indicating that the dissolution process is not divalent, i.e. occurs via direct dissolution of silicon without an oxide intermediate. The process appears to have some similarity with electropolishing where an ultrathin oxide resides on the surface during silicon dissolution. The oxide thickness for the

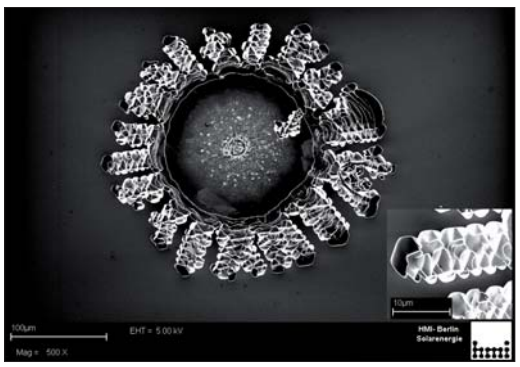

Fig. 4: HR-SEM image of a Si(111) surface after 10min in 40% NH_4F at 6V; light intensity 7.5mWcm^{-2}. Inset: ensemble of periodic microfacets, inclined by different angles with respect to the mean surface plane.

fractal structures is about 5 times larger and, in contrast to electropolishing, the sample roughens in a distinct manner. A marked difference is the observation of oxygen evolution where in the

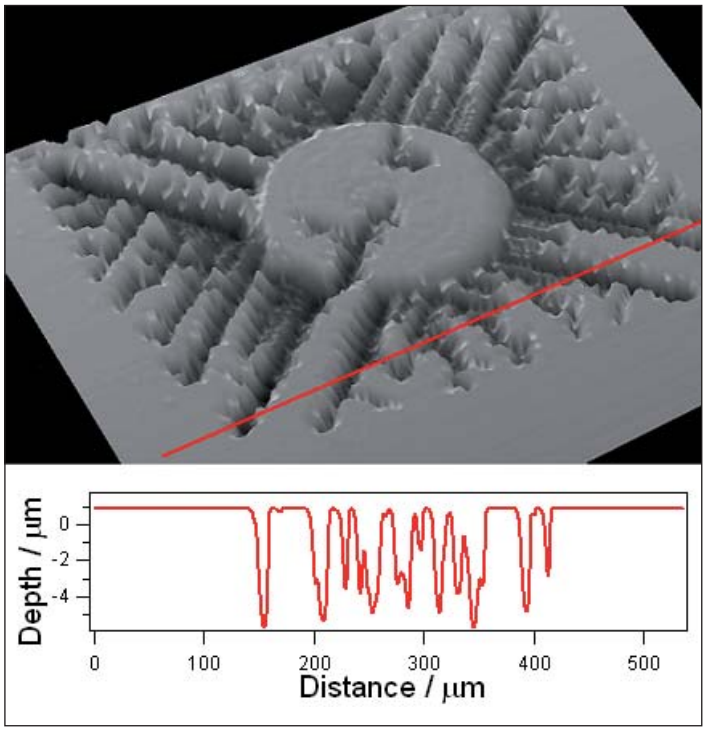

Fig. 5: Profilometric image of Si (100) after 10min in 40% NH_4F at 6V; light intensity 5mWcm^{-2}. Etch grooves have 4-6 µm depth. Three-dimensional etching has not yet exposed the microfacets (compare Fig. 3).

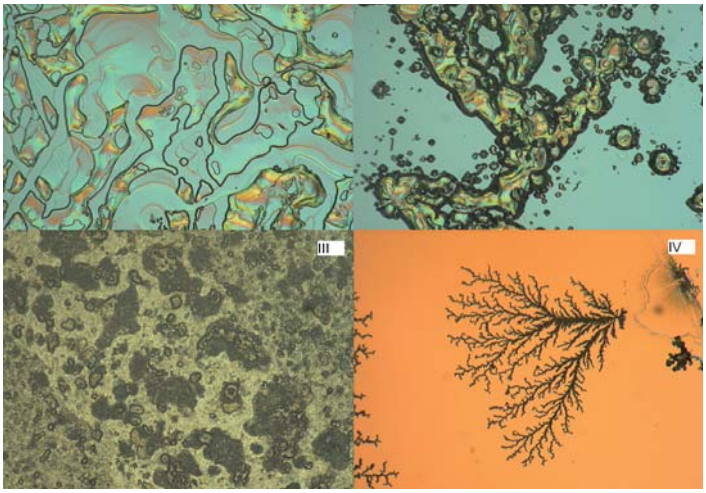

Fig. 6: Assorted micrographs (~1mm x 1.3mm) of different surface topographies after anodic (photo-)corrosion in 40% H_4F at 6V: I) p-Si(111); II) p-Si(110); III) n+-Si(111), all experiments in the dark) n-Si(111), illuminated, light intensity 5mWcm^{-2}.

center and at the periphery of O_2 bubbles residing on the surface (see Figs.3, 4) photocorrosion is initiated. Successive corrosion is highly anisotropic with a lateral dissolution rate that exceeds that for perpendicular processes by a factor of ~30. Also, all observed structures, independent of their sizes, can be attributed to smooth atomic facets. In a separate experiment on p-Si, we show (Fig.6, I, II) that distinctively different topographies are obtained for high supply of holes (in this case majority carriers). This points to a charge transport limited process for the creation of fractal structures with illuminated n-Si. Presently, models which incorporate minority carrier trajectories, oxide formation and porosity and diffusion limited etching/aggregation are derived to describe the morphology. Optical properties of these structures, also w.r.t. light harvesting, will be investigated.

[1] Mandelbrot B. B., 'The Fractal Geometry of Nature', Freeman, New York, 1982
[2] L. Spanos, Q. Liu, E. A. Irene, T. Zettler, B. Hornung, J. J. Wortman, J. Vac. Sci. Technol. **A12** (1994) 2653
[3] V. M. Aroutiounian, M. Zh.Ghoolinian, H. Tributsch, Appl. Surf. Sci., **162-163** (2000) 122-132
[4] M. Zhang, G. Zuo, Z. Zong, H. Chen, Z. He, C. Yang, D. Li, G. Zou, Appl. Phys. Lett. **88** (2006) 203106
[5] Witten, T., and Sandler, L., Physical Review Letters **47** (1981) 1400
[6] G. S. Higashi, R. S. Becker, Y. J. Chabal, and A. J. Becker, Appl. Phys. Lett., **58** (1991) 1656
[7] M. Lublow, H.J. Lewerenz, Surf. Sci. (2007), doi: 10.1016/j.susc.2007.01.038 (in press)
[8] A. Roy Chowdhuri, Dong-Un Jin, J. Rosado, C. G. Takoudis, Phys. Rev. **B 67** (2003) 245305

Corresponding author:
H.J. Lewerenz
lewerenz@hmi.de

Surface modified ruthenium nanoparticles: a promising cathode catalyst for fuel cell application

G. Zehl[1], I. Dorbandt[1], H. Tributsch[1], P. Bogdanoff[1], S. Fiechter[1], A. Hoell[2], S. Haas[2], B. Tesche[3]
■ 1 HMI, SE5 ■ 2 HMI, SF3 ■ 3 Max-Planck-Institut für Kohleforschung, Mühlheim a. d. Ruhr

Fuel cell and catalysts

In the development of devices for an efficient and environmentally compatible conversion of chemical energy into electrical power polymer electrolyte membrane fuel cells (PEM-FC) play a leading part. A wider utilisation of fuel cell modules for mobile power supply systems as well as for stationary applications is of high economic interest, as documented by world wide research activities. However, a commercially wide spread application of PEM-FCs is still impeded by high costs due to the utilisation of expensive membranes (e.g. NAFION®) and of noble metal based catalysts such as platinum. Therefore, cost reductions from increased fuel cell efficiencies as well as an improved system design are major topics of recent research activities.
Besides the phenomenon of instabilities of platinum based catalysts in PEM-FCs leading to a significant power drop at operation time above 1000 hours it is also warned against possible limitations in platinum supply in the long-term. Presuming 1.5 g platinum being needed for 1kW power, a gap of about one order of magnitude is assumed between the availability of platinum in reconnoitred ore deposits on the one hand and the worldwide platinum demand on the other. The distinct disparity between the high quantities of platinum needed and its limited availability reveals the relevance to develop alternative catalysts for PEM-FCs with reduced platinum content or, even more desirable, without any utilisation of platinum at all.

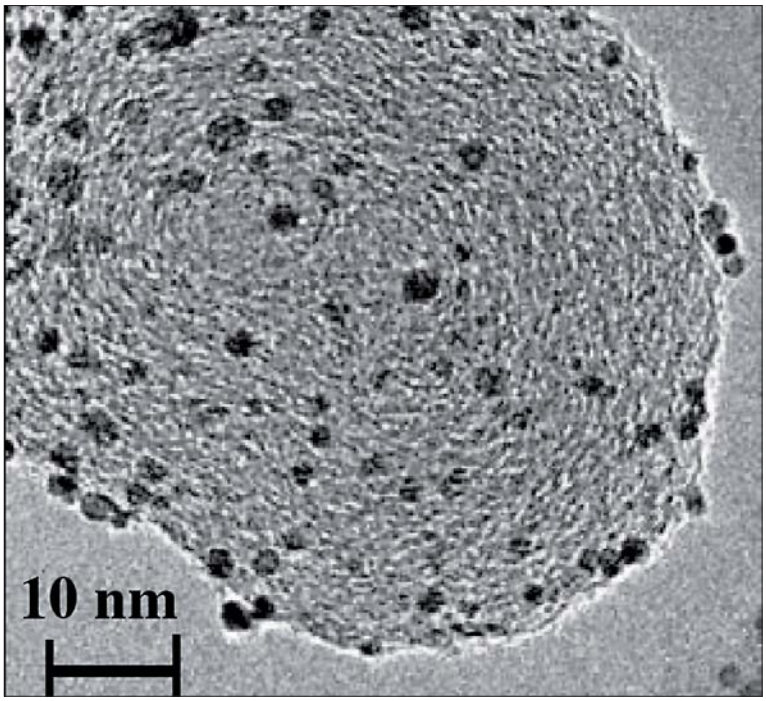

Fig. 1: Transmission Electron Micrograph of platinum particles on the surface of a soot support [1].

As recently successfully demonstrated, ruthenium based catalysts modified with selenium also exhibit high catalytic activity for the oxygen reduction reaction in fuel cells [1]. One advantage of ruthenium is that it is by a factor of 40 more common in the earth crust and its price presently amounts to only 17% of that of platinum. Furthermore, in Direct Methanol Fuel Cells (DMFC) the undesired crossover of methanol through the membrane from the anode space into the cathode compartment is still an unsolved issue. Therefore, platinum cathode catalysts suffer from activity losses due to methanol oxidation. As alternative, carbon supported ruthenium nanoparticles modified with selenium feature absolute methanol tolerance. Although intense studies of these catalysts were performed during the last decade, no definite conclusion with respect to the nature of the catalytically active sites and the constitution of the RuSe nano-particles could be drawn. But only a better understanding of the underlying principles is believed to pave the way towards higher active catalysts, thus making DMFCs more efficient and reliable.

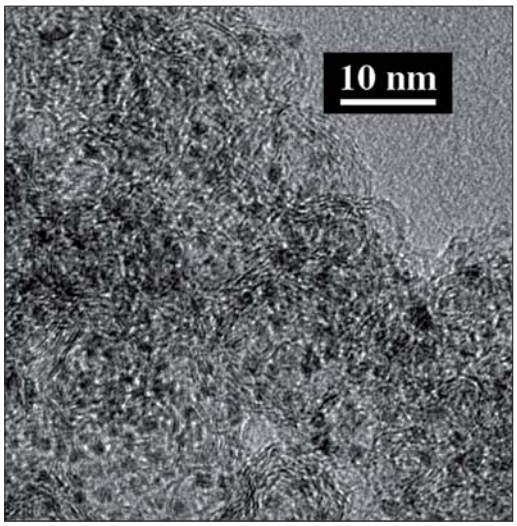

Fig. 2: Transmission Electron Micrograph of selenium modified ruthenium particles embedded in a thermally pre-activated carbon Black Pearls 2000® substrate.

Particle size and carbon support in electro-catalysts

Electrocatalysts in a fuel cell typically consists of two components:

- a carbon support (soot) allowing electrons to migrate from or to the catalytic centers passing an electric consumer and
- nanometer sized particles of a transition metal or cores of metal complexes attached to or integrated in the carbon support to guarantee efficient electron transfer.

Under fuel cell conditions, platinum nano-particles migrate on the surface of the carbon support. Therefore, it is observed that nano-sized particles coalesce after a short time forming larger particles. Since the catalytic activity is corroborated with the number of active sites on the metallic nano particle surface, the catalytic activity of such a catalyst decreases with decreasing surface. It has been demonstrated that ruthenium nano-particles can be properly fixed into nano-groves of the carbon support so that no migration of the metallic particles can occur. Fig. 1 shows a soot particle with an onion like structure of the carbon lattice planes with platinum particles on top of its surface [2]. In Fig. 2 the situation is illustrated for ruthenium particles embedded in the highly structured carbon matrix obtained via CO_2-activation.

While the Pt particles in Fig. 1 are located on the smooth outer surface of the carbon support $RuSe_x$ counterparts are found within easy accessible nano-cavity of a random oriented graphene layer network.

Structural analysis by X-ray scattering methods

Investigating RuSe electrocatalysts, data about the Se distribution over the catalyst's surface are particularly aspired, because catalytic activity and long term stability strongly depend on the Se content of the RuSe catalysts and the interaction between these two metals. Anomalous Small Angle X-ray Scattering (ASAXS) represents a powerful tool that yields structural parameters for element sensitive analysis of nano-structures, whereas also useful data about the chemical composition in the sub-nanometer scale can be obtained. Using the ASAXS technique one takes advantage of the so-called anomalous or resonant behaviour of the atomic scattering amplitude of an element near its absorption edge to separate its scattering contribution from other elements containing in the sample.

To clarify the structural features of the catalytically active Se-modified ruthenium nano-particles, carbon supported RuSe catalytsts were prepared by impregnating a previously CO_2 activated commercial carbon black (Black Pearls 2000® from Cabot) with $RuCl_3$ followed by reduction under hydrogen. Se modification of this Ru/C intermediate (ruthenium particle size 2-4 nm) was done by impregnation with $SeCl_4$ and subsequent reductive annealing at 800°C.

A complete set of samples, including the final working RuSe catalyst, and some intermediate preparation states such as non-modified (selenium free) ruthenium nano-particles or the bare carbon support were studied by ASAXS. The scattering curves were taken at 5 energies for that the anomalous scattering amplitude ‚f', varies equidistant in the vicinity below the selenium and the ruthenium K absorption edges, respectively. We took special care to extend the q-range up to larger values, according to get structural information also from sub nanometer structures.

Fig. 3 left shows that Ru and Se form nano-structures that alter the shape of the Black Pearls scattering curve dramatically. The sample which contains Selenium (Fig. 3 right) shows a small hump at $Q \sim 7\ nm^{-1}$ that is visible also at the Ru-K edge (Fig. 3 left). It was deduced that selenium within the sample generates clearly detectable and analyzable sub nanometer sized structural features.

Taken into account the energy dependences (the anomalous dispersion effect in the vicinity of the Se- and the Ru-edge as well) of the scattering intensity of all measured samples, a structure model of the catalytically active metallic nano-particles has been deduced, suggesting a nearly spherical Ru particles with mean diameters of 2.3 nm decorated with Se aggregates. These structures onto the ruthenium nano-crystallites feature a diameter less than 0.6 nm. These results are supported by data from XRD and EXAFS measurements, obtained from the same materials [3, 4]. Even so, the real shape of these of only few atoms consisting selenium clusters is not yet finally clarified. However, it is suggested to represent a symmetric ring like observed for free selenium clusters [5].

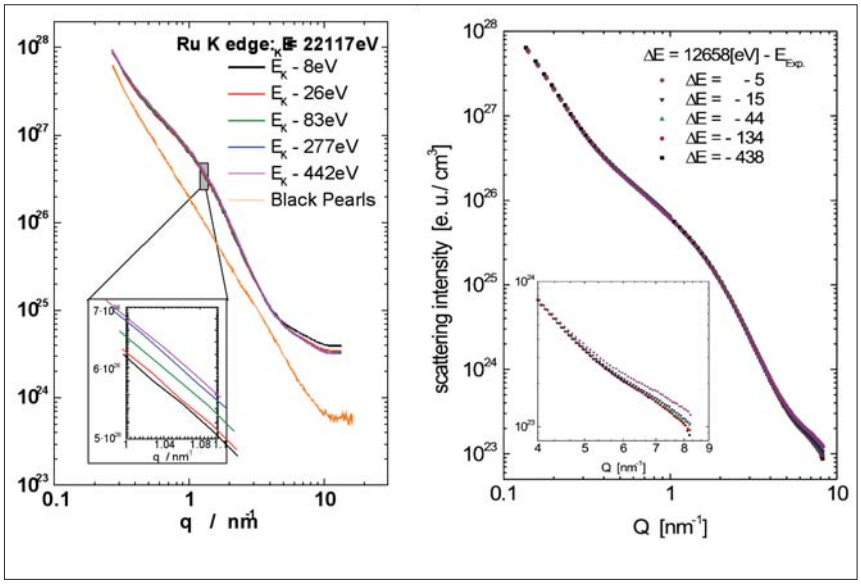

Fig. 3: The ASAXS curves measured near below the K-absorption edges of ruthenium (left) and selenium (right) allowed to distinguish three structural elements.

We also confirmed by ASAXS that the selenium modification renders the ruthenium nano-particles extremely resistant against agglomeration and particle growth. The average particle size of the ruthenium particles was found to remain below 2.5 nm in diameter even after long annealing at 800°C.

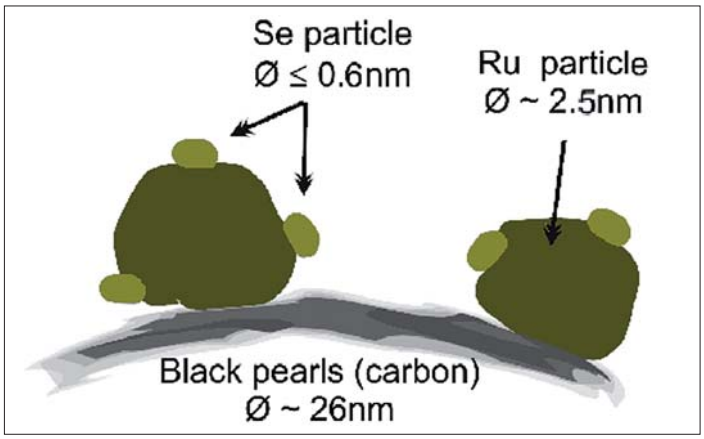

Fig. 4: Suggested scattering equivalent structural model for ruthenium based electrocatalysts supported on activated carbon and modified with selenium.

[1] Alonso-Vante, N.; Bogdanoff, P.; Tributsch, H.: On the Origin of the Selectivity of Oxygen Reduction of Ruthenium - Containing Electrocatalysts in Methanol - Containing Electrolyte; J. Catalysis **190** (2000) 240.

[2] U. Paulus, PhD-Thesis, ETH Zürich, 2002.

[3] Fiechter, S.; Dorbandt, I.; Bogdanoff, P.; Zehl; G.; Schulenburg, H.; Tributsch, H.; Bron, M.; Radnik, J.; Fieber-Erdmann, M.: Surface modified Ruthenium nanoparticles: structural investigation and surface analysis of a novel catalyst for oxygen reduction; Journal of Physical Chemistry C **111** (2007) 477-487.

[4] Zehl, G.; Dorbandt, I.; Fiechter, S.; Bogdanoff, P.: On the Influence of Preparation Parameters on the Catalytic Properties of Carbon Supported Ru-Se Electrocatalysts; Journal of New Materials for Electrochemical Systems, submitted.

[5] Becker, J.; Rademann, K.; Hensel, F.: Ultraviolet photoelectron studies of the molecules Se_5, Se_6, Se_7 and Se_8 with relevance to their geometrical structure; Z. Phys. D. - Atoms, Molecules and Clusters **19** (1991) 229.

Corresponding author:
S. Fiechter
fiechter@hmi.de

Novel approaches to quasi solid state electrolytes in dye sensitized solar cells

M. Junghänel and H. Tributsch
■ HMI, SE5

Introduction

Dye sensitized solar cells (DSC, Fig.1) have attracted significant attention over the last decade [1-3] and appear to be close to enter the market. A wide bandgap semiconductor (TiO_2) is sensitized with an organic dye molecule (most often Ru-complexes) yielding conversion efficiencies of 10,4 % [4]. Since the cell concept is based on the transport of majority charge carriers, the purity of the materials is less important compared to conventional Si solar cells making the device potentially very cheap. Though intrinsic stability has been proven [5] in several studies, the employment of a liquid electrolyte demands a hermetic sealing for at least 20 years which is an unsolved problem so far. At HMI the nano surface conductivity solar cell (NSCSC) is developed that is based on a quasi solid state electrolyte which is in equilibrium with the ambient atmosphere making an extra sealing redundant.

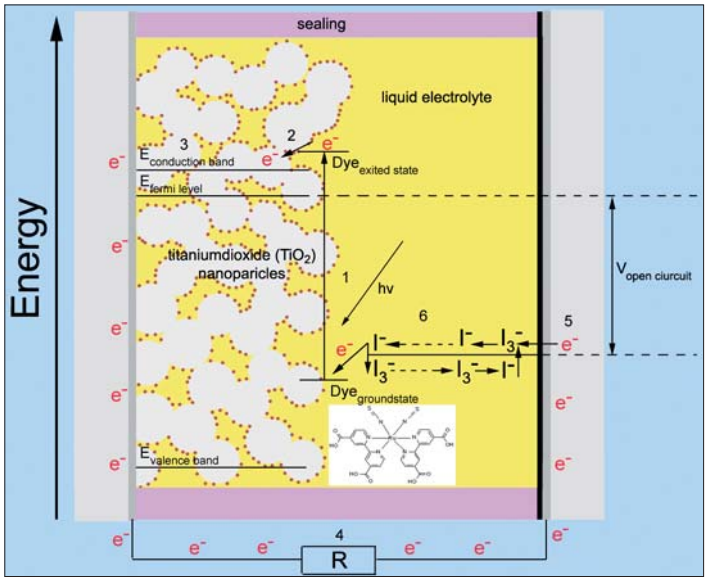

Fig. 1: operation principle of a dye sensitized solar cell

Preparation of nano surface conductivity solar cell

The preparation is based on low-cost techniques and materials trying to make the cell assembly as simple as possible. On a $F:SnO_2$ coated glass (sheet resistance 10 Ω/□) a 10 µm thick layer of nanoporous TiO_2 particles (diameter 20 nm) is screen printed. The electrode is stained by dipping it into a 0,5 mM dye solution of a Ru-bipyridil-complex (s. Fig 1).
On top a layer of carbon particles is deposited by doctor blading that acts both as a rectifying contact and as a catalyst for electron regeneration. It replaces the expensive noble metal platinum that is employed in classical DSC. Finally the TiO_2 surface is covered with litiumiodide (LiI) by dip coating. Any remaining solvent is removed under reduced pressure (10^{-6} mbar for 2 hours). After equilibration with the ambient atmosphere the hygroscopic LiI is partly hydrated. It is proposed that by partial oxidation of iodide long poly iodide chains are formed that allow charge transport by a Grotthus-type mechanism. A cross section SEM picture is shown in Fig. 2.

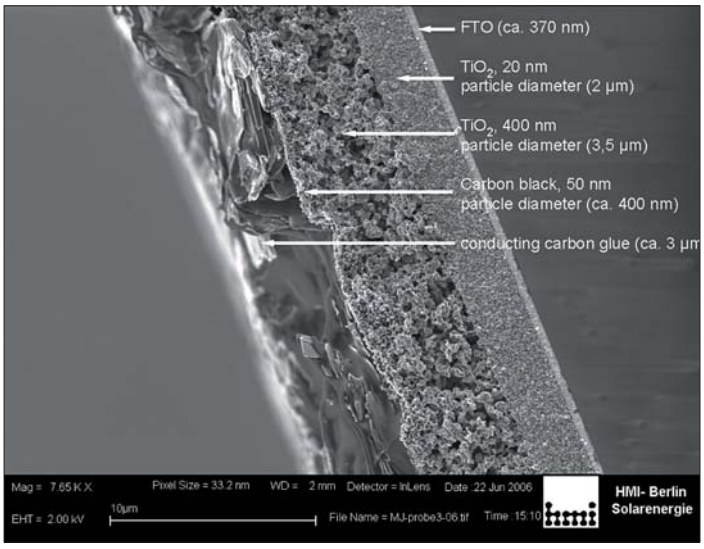

Fig. 2: SEM cross section of a nano surface conductivity solar cell

Thermogravimetric analysis (TGA)

Iodine with a vapor pressure of 0,41 hPa at RT might be susceptible to evaporation if it is not chemically bound. TGA-MS analysis revealed that up to 80 °C no iodine desorbs from the surface making cell operation without sealing possible even at higher temperature (Fig. 3). However, water reversibly desorbs from the surface for temperature >40 °C, lowering the conductivity of the LiI/I-film and thus limiting the photocurrent. The best performance is achieved for temperatures between 35-40 °C.

Cell efficiency and outlook

The cell parameters of an average NSCSC cell are $I_{SC} = 3{,}4\ mAcm^{-2}$, $V_{OC} = 635\ mV$, efficiency = 1,1 %. The cell efficiency is limited by an insufficient current collection. Photovoltage transient measurements revealed that there is a significant charge transfer resistance between the TiO_2 nanoparticles an the FTO working electrode. It is the main challenge to lower this energy barrier and enhance charge extraction.

The recombination rate between conduction band electrons and electron acceptors on the TiO_2 surface is already comparable to conventional DSC. At 1 sun the electron lifetime is between 2-4 ms. Current research focuses on the long term stability of the device and a better understanding of the hole transport mechanism.

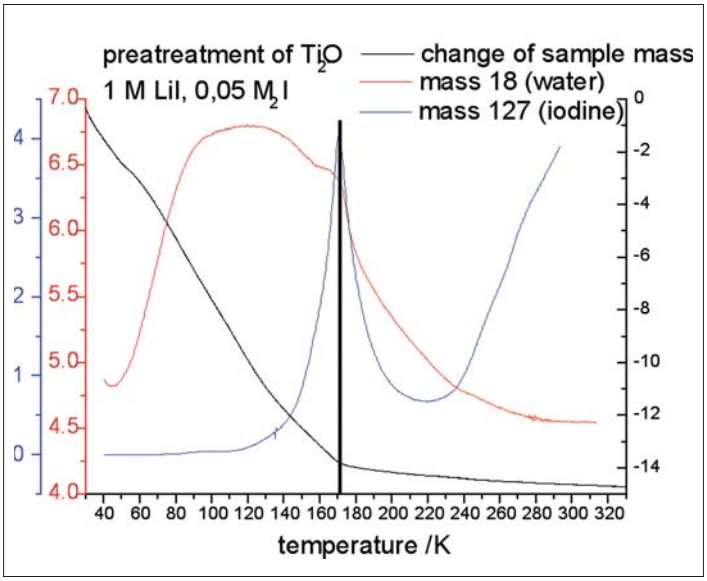

Fig. 3: Thermogravimetric analysis (TGA) of nano surface conductivity solar cell

[1] H. Tributsch, Photochem. Photobiol. **14**, 95 (1971)
[2] B. O'Regan, M. Grätzel, Nature **353**, 737-739 (1991)
[3] M. Junghänel, H. Tributsch, J. Phys. Chem. B **109**, 22876-22883 (2005)
[4] M. A. Green, K. Emery, D. L. King, Y. Hishi kawa, W. Warta, Prog. Photovolt: Res. Appl. **14**, 455-461 (2006)
[5] P. Wang, C. Klein, R. Humphrey-Baker, S. Zakeeruddin, M. Grätzel, Applied Physics Letters **86**, 123508 (2005)

Corresponding author:
M. Junghänel
junghaenel@hmi.de

Nanostructured Injection Solar Cell with Tungsten Disulfide Absorber

M. Thomalla, H.Tributsch
■ HMI, SE5

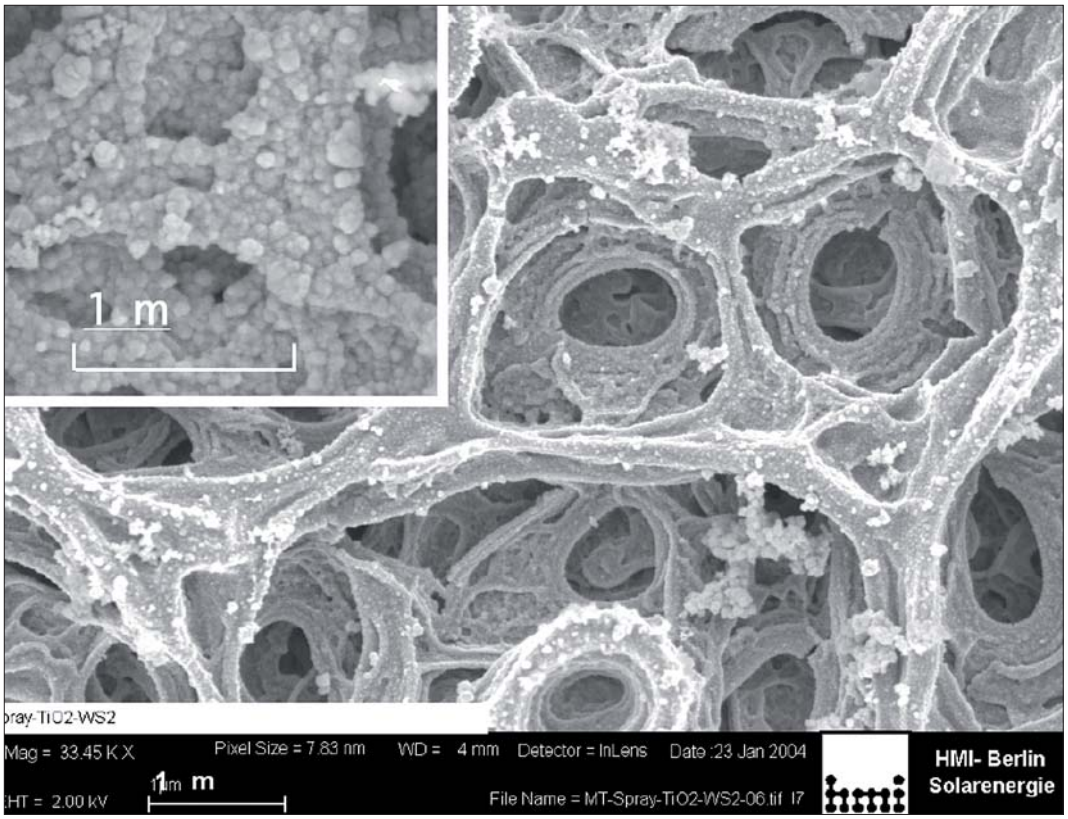

Fig. 1: TiO_2 substrate spray pyrolysis

Nanostructured photoelectrochemical solar cells have received considerable attention in recent years as an alternative to conventional solar cells. In particular, the solar cell developed by Grätzel and his group with its high solar energy conversion of up to 11% has increased the research efforts in this fieldi. Unfortunately the original cis-$RuL_2(SCN)_2$ with L = 2,2'-bipyridyl-4,4'-dicarboxylatoacid (bpca) dye has not the desirable stability of 20 years [2,3,4,5] and in addition the chemical stability of the iodine redox system, the volatility of the solvent and the sealing of the cells remain unsolved. An interesting approach is to replace the organic dye with an inorganic semiconductor quantum dot. Semiconductor quantum dots have several advantages. Firstly, their band gap can be easily adjusted by changing the size of the particle to match the solar spectrum and the band gap of TiO_2. Secondly, they may be selected to possess a high absorption coefficient, which allows to produce very thin absorber and to reduce the amount of materials needed. And most important, it may be possible to apply a metallically conducting nano-contact as they are used in traditional solid states solar cells.

Porous, nanostructured sol gel - TiO_2 (100 nm) has been sensitized with WS_2 quantum sheets (~5 nm) with the help of chemical bath deposition (CBD has been chosen out of several deposition methods which have been tested, e.g. electrochemical bath deposition, inverse micelles, sputtering, nanotubes). The absorber has been characterized with help of EDX, TEM, SEM, Ra-

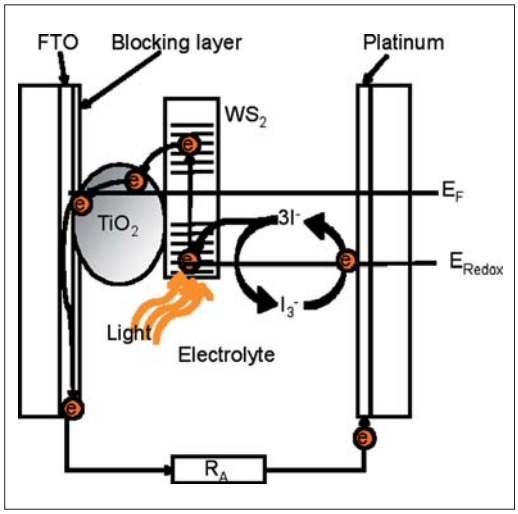

Fig. 2: Schematic presentation of TiO_2-WS_2 injection solar cell

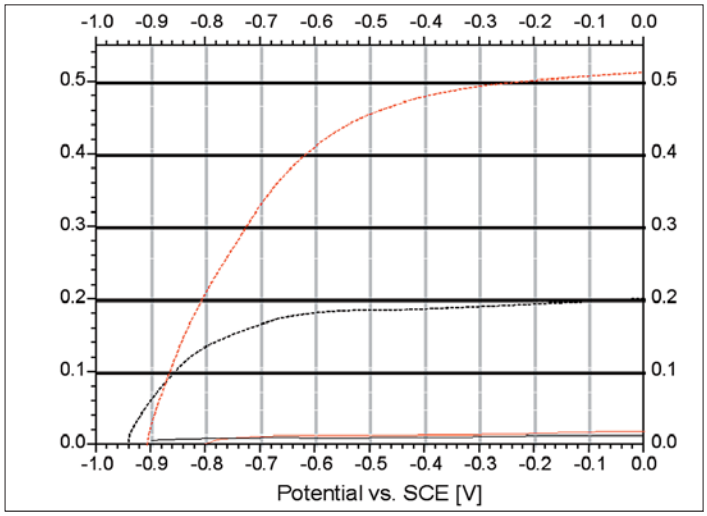

Fig. 3: *I-U* curve of a sensitization solar cell before (black curve) and after (red curve) of the TiO_2-WS_2 electrode with cystein

man spectroscopy and light absorption measurements. The photosensitization was confirmed via electrochemical measurements. The surface of TiO_2 has been modified by a thin Al_2O_3 film, which significantly enhanced the photocurrent density to $0.4\text{-}0.7\ mA/cm^2$.

The TiO_2 layers which serve as substrates for the absorber had to be optimized. The best and stabile substrates were produced with sol gel method and spray pyrolysis (Fig. 1). The geometry of the cell is shown in Fig. 2.

Treating the electrode with various chemicals e.g. cysteine, which is well known as electron transfer molecule in biological system, increased the photocurrent significantly, as can be seen in Fig. 3. It is suggested that cysteine can on the one hand passivate the dangling bonds of the WS_2 nano sheets and therefore decrease recombination processes. On the other hand due to its unique electronic structure and the ability to conduct electrons in only one direction it could serve as a bridge between the electrolyte and the absorber increasing the photocurrent.

[1] B. O'Reagan, M. Grätzel, Nature **353** (1991) 737
[2] H. Greijer Agrell, J. Lindgren, A. Hagfeldt Solar Energy, **75** (2003), 169-180
[3] M. Turrion, B. Macht, P. Salvador, H. Tributsch, Z. Phys. Chem. **212** (1999) 51
[4] B. Macht, M. Turrion, A. Barkschat, P. Salva dor, K. Elmer, H. Tributsch, Solar Energy Mater. Solar Cells **73** (2002) 163
[5] M. Thomalla, H. Tributsch, J. Phys. Chem. B.; 2006, 110, 12167-12171.

Corresponding author:
M. Thomalla
thomalla@hmi.de

Epitaxial SiC-ZnO interfaces, electronics and morphology

S. Andres, T. Seyller, C. Pettenkofer
■ HMI, SE6

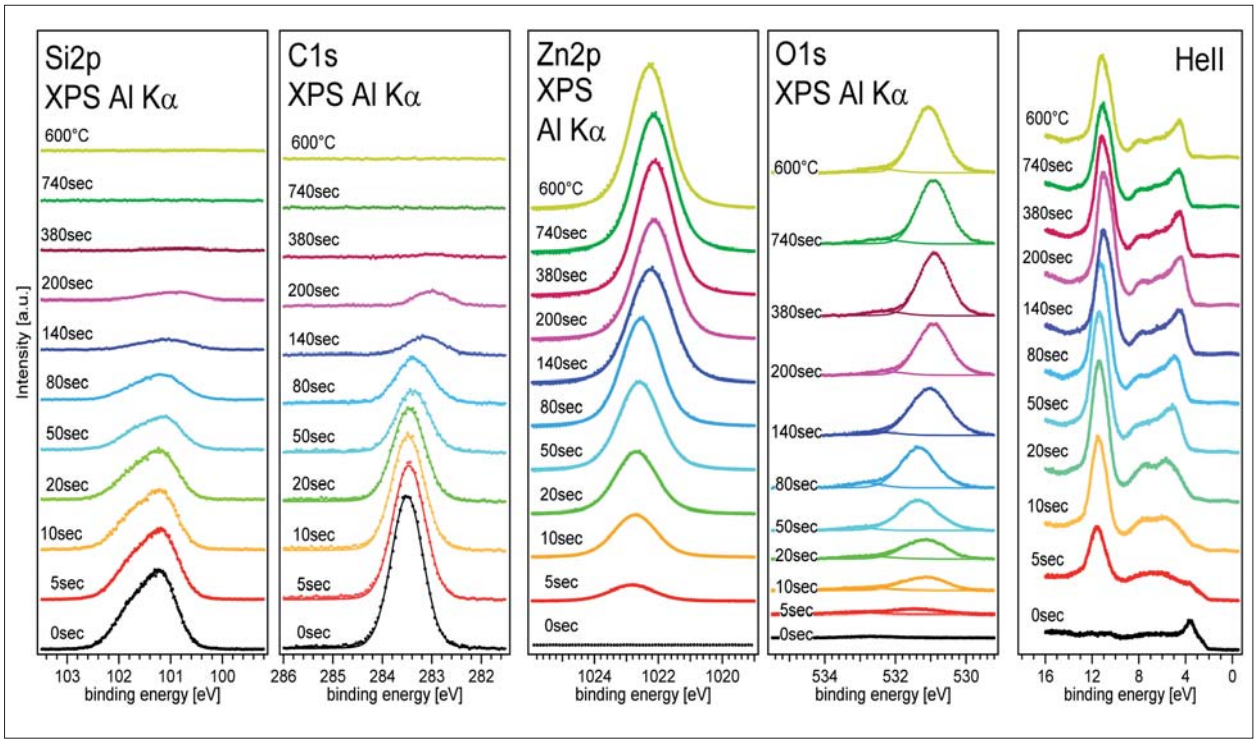

Fig. 1: Valence and Corelevel spectra in the course of ZnO deposition on (0001) 6H SiC

Transparent electronics are a hot topic in today's material research. We report here on the fabrication and surface characterization of a simple heterostructure made from the wide band gap materials ZnO and 6H-SiC. Due to the necessary wide band gap needed for the contact partners in a transparent diode, doping and interface properties play a crucial role in the process of contact formation.

n-type 6H-SiC (0001) surfaces were hydrogen terminated [2,3] and found to be free of oxide and hydrocarbon contaminations on a sub monolayer level. ZnO is deposited by a specifically developed MOMBE technique [1]. All preparation and analysis steps were performed in a true ultra high vacuum environment to ensure a contamination free investigation of the device during all steps of the fabrication. The electronic structure of the interface is monitored by surface sensitive electronspectroscopies like UPS and MXPS (Ultraviolet and Monochromatic X-ray Photoelectron Spectroscopy).

Substrate and film core level and valence band spectra (Fig.1) show nicely the layer by layer growth of an clean and non-reactive abrupt ZnO

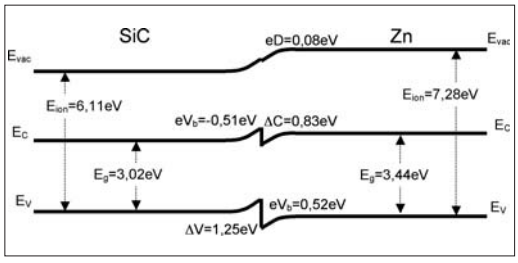

Fig. 2: Band alignment of the SiC-ZnO heterojunction as derived from the data displayed in Fig. 1

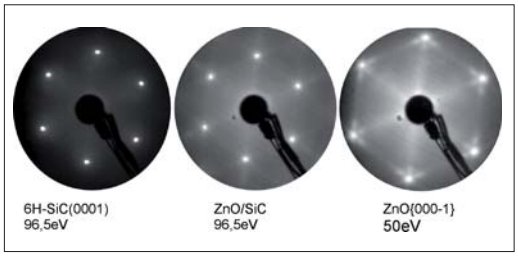

Fig. 3: LEED pattern for the substrate, film and at different energy showing the facets of the Zn-terminated surface

interface on the SiC substrate. Which means no chemical intermixing between the contact partners takes place. LEED data proof the crystallinity and order of the growing (0001) ZnO film forming a diode device. From Fig 1 the band alignment of the diode may be derived as shown in Fig 2.

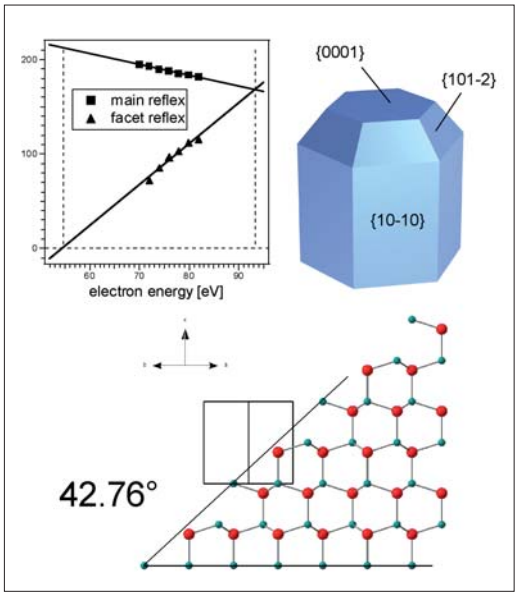

Fig. 4: Evaluation of the facet type from the LEED data for the epitaxial (0001) ZnO surface

The data reveal the band bending in the substrate and film as a consequence of the charge carrier distributions in the interface region, given by the doping of the film and the substrate. The band offsets e.g. the difference of the valence band edges for both contact phases are given by the local atomic and electronic structure direct at the contact plane. The specific atomic arrangement and the electronic states present at a particular surface determine the offsets, which by itself determine the functionality of the device.

Here we see the unusual case that no resulting interphase dipole is detected as to be seen as a nearly smooth transition in the vacuum level from SiC to ZnO. Often a dipolar contribution in the order of 1eV is detected in heterodiodes influencing the band alignment. The missing interface dipole gives the opportunity to vary the band alignment in the band offsets according to the needs of a particular device by introducing bond modifications in the contact plane. As our LEED-data proof, the oxygen termination of the (0001) ZnO surface forms the interface to the SiC surface. A modification by the introduction of a specifically designed interfacial layer is a promising perspective to taylor the electric properties of the diode. The morphology of the prepared diode is derived from the LEED data.

The ZnO film grows epitaxial in a layer by layer growth mode with a faceting of the ZnO surface which is indicative for a Zn termination of the vacuum interface of the film. Consequently an oxygen termination has to be present for this polar crystal surface at the SiC-ZnO interface. The evaluation of the facet is given in Fig 3. The behavior of the LEED spots responsible for the (000-1) surface with respect to the facet signals is plotted against the electron energy. The obtained angle of 43° is in good agreement to the proposed (101-2) facet, which is appearing due to the lower energy needed to build a non polar surface with respect to the purely Zn-terminated (000-1) surface. This evaluation is shown in Fig 4.

This example shows nicely the power of surface analytical tools in the characterization of the morphology and electronic properties of a proposed device. Even the perspectives of a future improvement of the device can be deduced from the obtained data. Future work will be directed to variations in the doping of the SiC substrate, as a p-doped SiC for our first investigations was not available. Further attempts will be made to grow p-type ZnO layer.

[1] Andres A.; Pettenkofer C.: Epitaxial deposition of ZnO. In: Ellmer K. ; Stadermann G. [Eds.] : TCO für Dünnschichtsolarzellen und andere Anwendungen III : Workshop 10. - 12.04.2005 in Freyburg / Unstrut. Berlin: Forschungsverbund Sonnenenergie c/o Hahn-Meitner-Institut, 2005 p.25-27

[2] T. Seyller, J. Phys.: Condens. Matter **16**, S1755 2004

[3] N. Sieber, B. F. Mantel, T. Seyller, J. Ristein, L. Ley, T. Heller, D. R. Batchelor, and D. Schmeißer, Appl. Phys. Lett. **78**, 1216 2001.

Corresponding author:
C. Pettenkofer
pettenkofer@hmi.de

Part of a formula describing the behaviour of semi-flexible polymers

Facts and Figures

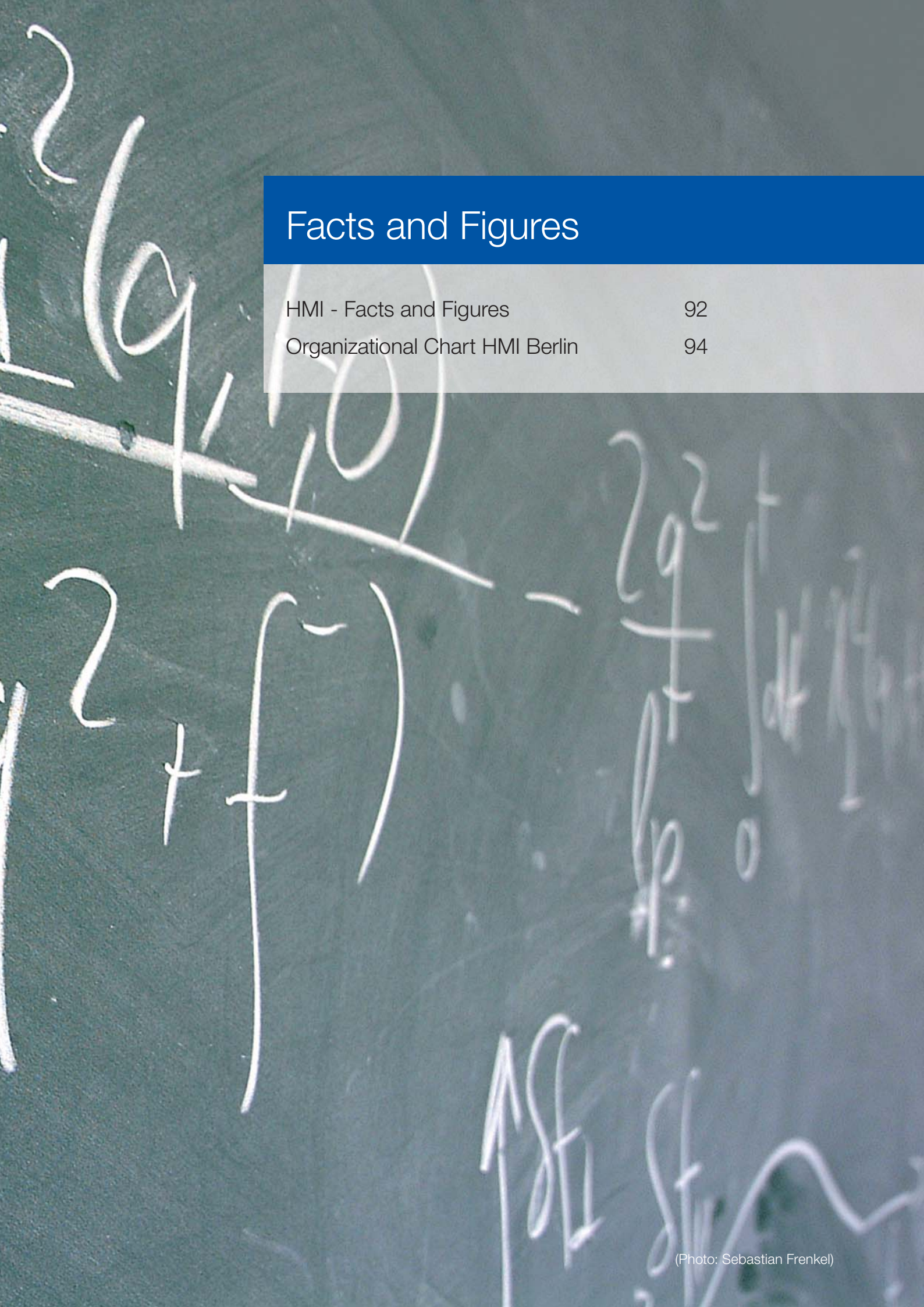

(Photo: Sebastian Frenkel)

HMI – Facts and Figures

Founded in 1959

Locations:
Main campus: Berlin Wannsee
Second campus: Berlin-Adlershof

Member of the Helmholtz Association of German Research Centres

Legal Status: limited liability company (GmbH)

Directors:
Prof. Dr. Michael Steiner, Scientific Director
Dr. Ulrich Breuer, Administrative Director

Scientific divisions: Structure Research and Solar Energy Research

Budget:

Financed by the shareholders:
German Federal Government (90 %)
City State of Berlin (10 %)

In 2006, HMI's complete budget amounted to 73 Million Euros, including 5 Million Euros Third Party funding

Personnel:

In 2006, HMI employed 610 people (full time equivalents). In addition to that, there were 60 apprentices in various professions

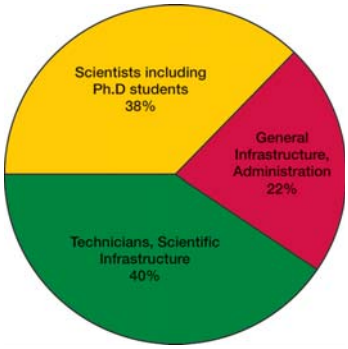

Composition of staff

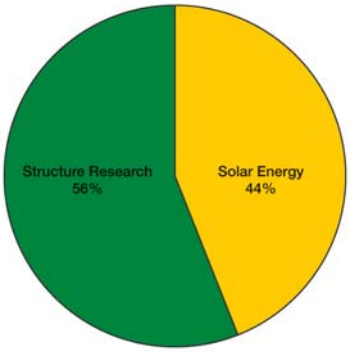

Distribution of scientific staff among the two scientific divisions

Board of Governors

Dr. Beatrix Vierkorn-Rudolph
Federal Ministry of Education and Research

Wolfgang Eckey
Senate Department for Education, Science and Research of the City State of Berlin

Dr. Bruno Broich
Technology Foundation Berlin

Dr. Jan Grapentin
Federal Ministry of Education and Research

Hans Jürgen Hardt
Federal Ministry of Finance

Hans-Jürgen Reil
Senate Department for Finance of the City State of Berlin

Prof. Dr. Ulrich Merkt
Institute of Applied Physics and Centre for Microstructure Research at the University of Hamburg

Prof. Dr. Eberhard Jaeschke
BESSY GmbH

Dr. Andrea Denker
HMI – Department SF4

Dr. Reiner Klenk
HMI – Department SE2

Scientific Advisory Board

Prof. Dr. Hans Henrik Andersen
Ørsted Laboratory, Copenhagen, Denmark

Prof. Dr. T.W. Clyne
Department of Materials Science and Metallurgy, Cambridge, UK

Prof. Dr. Dame Julia Higgins
Polymer Sciences Department of Chemical Engineering Imperial College London, London, UK

Dr. Franz Karg
Shell Solar GmbH, Munich, Germany

Prof. Dr. Bernhard Keimer
Max-Planck-Institut für Festkörperforschung, Stuttgart, Germany

Prof. Dr. H.J. Kreuzer
Department of Physics and Atmospheric Science, Halifax, Nova Scotia Canada

Prof. Dr. Helmuth Möhwald
Max Planck Institute of Colloids and Interfaces, Potsdam-Golm, Germany

Prof. Dr. Antonio Luque López
Instituto de Energia Solar Universidad Politechnica Madrid, Madrid, Spain

Prof. Dr. W.C. Sinke
Solar Energy, Energieonderzoek Centrum Nederland (ECN) Petten, The Netherlands

Prof. Dr. William George Stirling
European Synchrotron Radiation Facility (ESRF), Grenoble, France

Prof. Dr. Martin Stutzmann
Physics Department (E25), Technische Universität München, Munich, Germany

Prof. Dr. Alexander Wokaun
Paul-Scherrer-Institut, Research Dept.: General Energy (ENE) Villigen-PSI, Switzerland

Prof. Dr. Dr. Hartmut Zabel
Chair of Experimental Physics/Condensed Matter Physics, Faculty of Physics and Astronomy, Ruhr-Universität Bochum, Bochum, Germany

Dr. Ehrenfried Zschech
AMD Saxony LLC & Co. KG, Dresden, Germany

Organizational Chart HMI Berlin

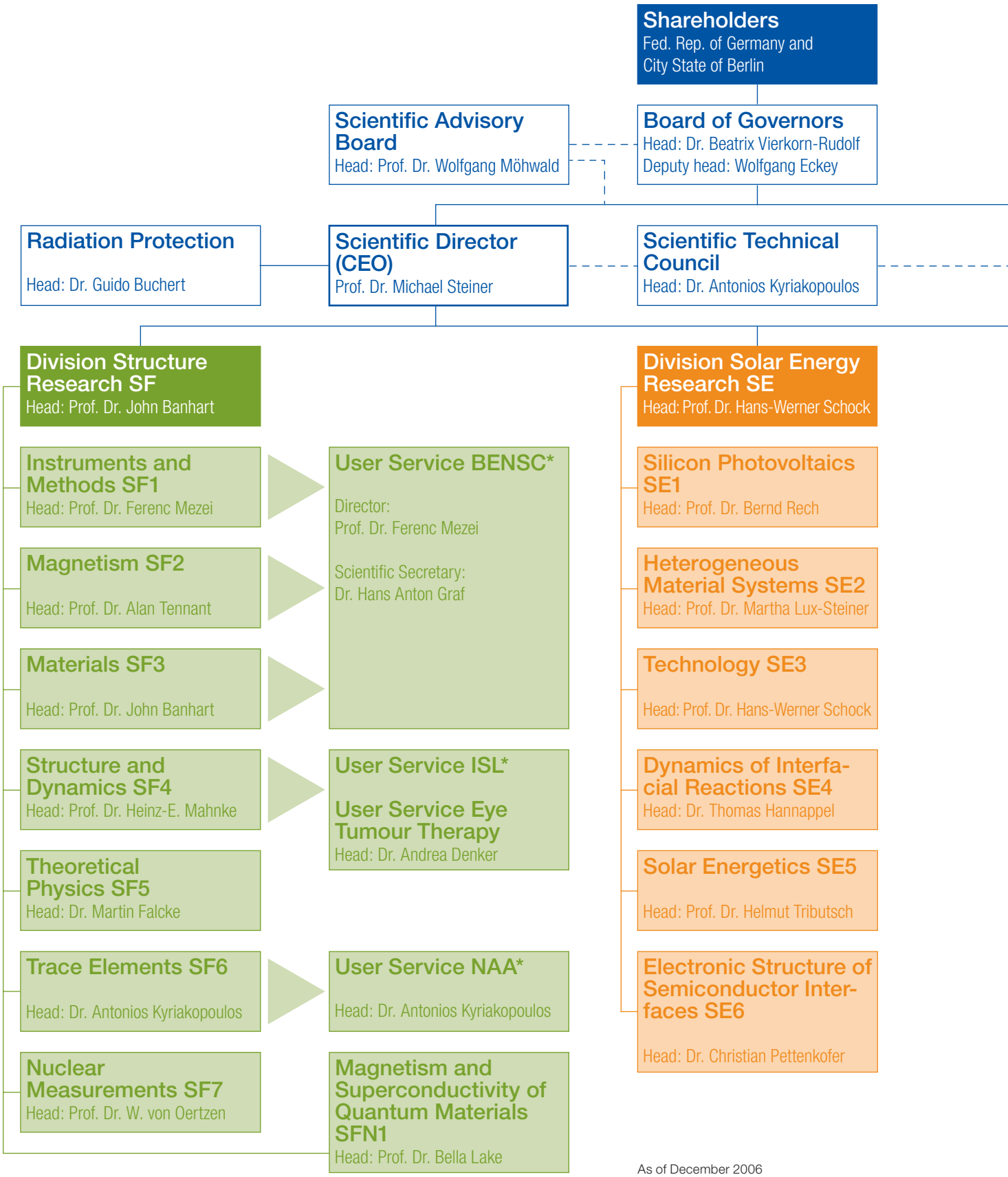

As of December 2006

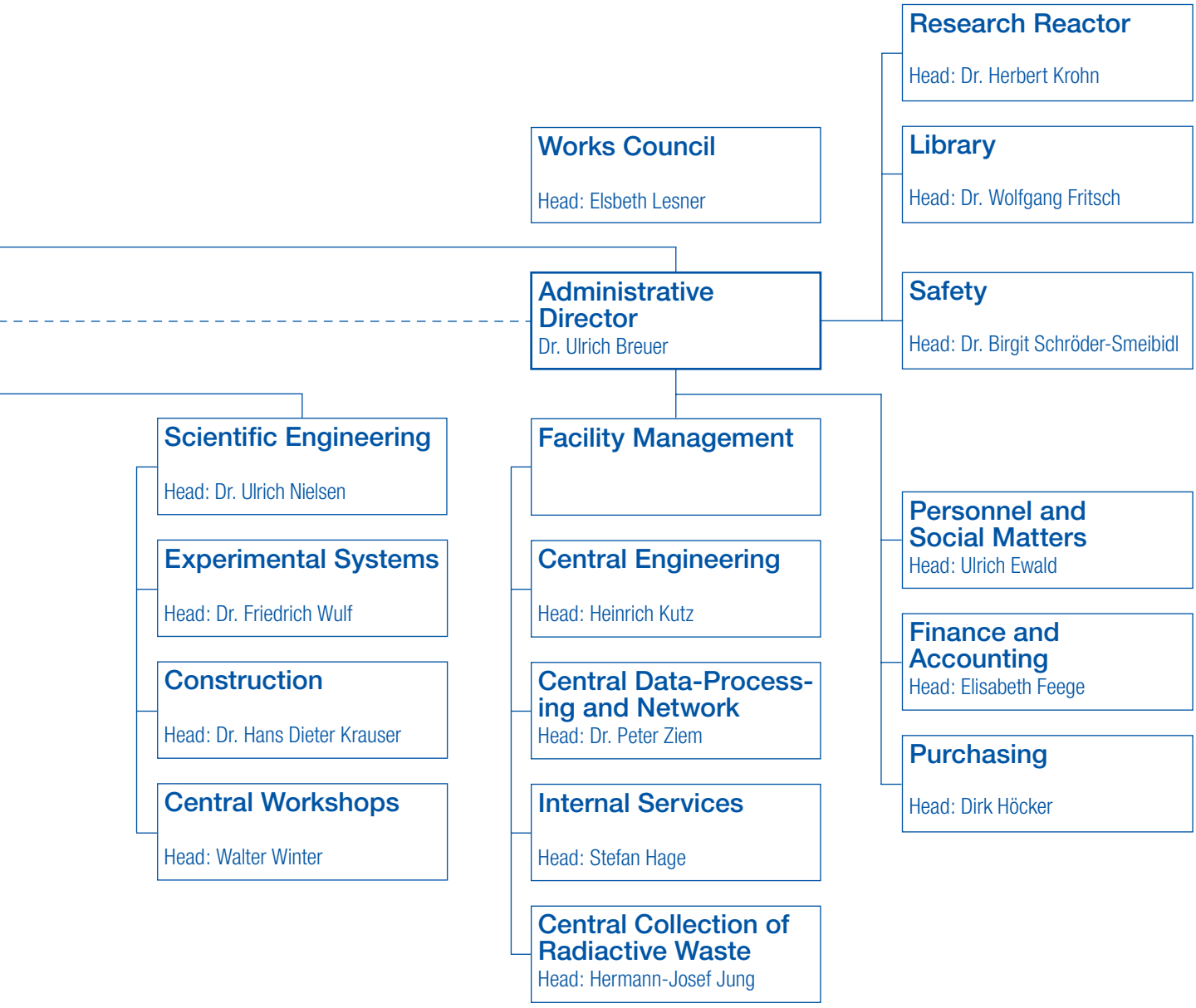

*BENSC = Berlin Neutron Scattering Center

*ISL = Ion Beam Laboratory

*NAA = Neutron Activation Analysis

Imprint

1. Edition
September 2007

Annual Report 2006
Selected Results
HMI-B 614

Published by
Hahn-Meitner-Institut Berlin GmbH
Glienicker Str. 100
14109 Berlin
Germany

info@hmi.de
http://www.hmi.de
Phone: (+49) (0) 30-8062-0
Fax: (+49) (0) 30-8062-2998
Member of the Helmholtz Association

Concept and Coordinating Editor
Dr. Paul Piwnicki
piwnicki@hmi.de

Coordination Solar Energy
Erik Zürn
erik.zuern@hmi.de

Book Design
Frenkelson Werbeagentur, Potsdam
www.frenkelson.de

Printing
Druckerei Format, Berlin
www.formatdruck.de